ABSTRACT

EXPERIMENTAL AND NUMERICAL DETERMINATION OF FLUID VELOCITY PROFILES AND TURBULENCE INTENSITY IN MIXING VESSELS

by
Chun-Chiao Chou

In this study, both a laser-Doppler velocimeter (LDV) and a computational fluid dynamic (CFD) software package (*FLUENT*) were used to experimentally determine and numerically predict the velocity distribution of an unbaffled and a baffled mixing vessel. Two types of impellers were employed, namely a flat blade turbine (FBT) and a pitched blade turbine (PBT). These impellers were studied in a single-impeller or multiple-impeller configuration in the unbaffled and baffled vessels. The flow characteristics in the impeller regions were measured by LDV and used as boundary conditions in the numerical computation. Turbulence effects were numerically simulated using either the k-ε or the algebraic stress model (ASM).

In general, good agreement between the CFD predictions and the LDV measurements was obtained. Predictions in which the boundary conditions were specified at multiple surfaces in the impeller region (i.e., two planes instead of one) were found to be superior to those in which less accurate boundary conditions were used. The predictions based on ASM were typically found to be in closer agreement with the experimental data than those based on the k-ε model.

The flow patterns in the unbaffled vessels were found to be dominated by the tangential component of the velocity, regardless the types of impeller used. In the baffled vessels the flow patterns were strongly dominated by both the axial and tangential

components. The presence of a second impeller in the baffled vessels altered the flow considerably, producing a strong vertical recirculation pattern between the impellers, and significantly reducing the circulation flow below the lower impeller.

EXPERIMENTAL AND NUMERICAL DETERMINATION OF FLUID VELOCITY PROFILES AND TURBULENCE INTENSITY IN MIXING VESSELS

by
Chun-Chiao Chou

A Dissertation
Submitted to the Faculty of
New Jersey Institute of Technology
in Partial Fulfillment of the Requirements for the Degree of
Doctor of Philosophy

Department of Chemical Engineering,
Chemistry, and Environmental Science

January 1995

APPROVAL PAGE

EXPERIMENTAL AND NUMERICAL DETERMINATION OF FLUID VELOCITY PROFILES AND TURBULENCE INTENSITY IN MIXING VESSELS

Chun-Chiao Chou

Dr. Piero M. Armenante, Dissertation Advisor — Date
Professor of Chemical Engineering, Chemistry, and Environmental Science, NJIT

Dr. Gordon A. Lewandowski, Committee Member — Date
Professor of Chemical Engineering, Chemistry, and Environmental Science, NJIT

Dr. Ching-Rong Huang, Committee Member — Date
Professor of Chemical Engineering, Chemistry, and Environmental Science, NJIT

Dr. Dimitrios P. Petridis, Committee Member — Date
Professor of Chemical Engineering, Chemistry, and Environmental Science, NJIT

Dr. Ronald S. Kane, Committee Member — Date
Assistant Vice President for Academic Affairs—Graduate Studies and
Adjunct Professor of Mechanical Engineering, NJIT

BIOGRAPHICAL SKETCH

Author: Chun-Chiao Chou

Degree: Doctor of Philosophy in Chemical Engineering

Date: January 1995

Undergraduate and Graduate Education:

- Doctor of Philosophy in Chemical Engineering
  New Jersey Institute of Technology, New Jersey, 1995
- Master of Science in Environmental Science
  New Jersey Institute of Technology, New Jersey, 1990
- Bachelor of Science in Chemical Engineering
  National Taipei Institute of Technology, Taipei, Taiwan, 1983

Major: Chemical Engineering

Publications

Armenante P. M. and C. C. Chou, 1994. "Experimental LDV Measurement and Numerical CFD Determination of the Fluid Velocity Distribution in an Unbaffled Mixing Vessel," *AIChE Symp. Ser.*, **90**(299): 33-40.

Armenante P. M., C. C. Chou, and R. R. Hemrajani, 1994. "Comparison of Experimental and Numerical Fluid Velocity Distribution Profiles in an Unbaffled Mixing Vessel Provided with a Pitched-Blade Turbine," *Proc. 8th Europ. Conf. Mixing*, NO. 136, 349-356.

Publication currently under review

Armenante P. M. and C. C. Chou, 1994. "Experimental and Numerical Fluid Velocity Profiles in a Baffled Vessel Provided with a single or Double Pitched-Balde Turbine agitation System," *AIChE J.*, under review.

Presentations

Armenante P. M. (presenter) and C. C. Chou, "Experimental LDV Measurement and Numerical CFD Determination of the Fluid Velocity Distribution in an Unbaffled Mixing Vessel," presented at the 1993 AIChE Annual Meeting, St. Louis, Missouri, Nov. 7-12, 1993.

Armenante P. M., C. C. Chou, and R. R. Hemrajani, "Comparison of Experimental and Numerical Fluid Velocity Distribution Profiles in an Unbaffled Mixing Vessel Provided with a Pitched-Blade Turbine," presented at the 8th European Conference on Mixing, Cambridge, U.K., 21-23 September 1994.

This dissertation is dedicated to
my parents and my wife

ACKNOWLEDGMENT

I would like to express my sincere gratitude to my dissertation advisor, Dr. Piero M. Armenante, for his support and valuable advice during my doctoral research and education. Without his support, this work would not have been finished.

I would like to sincerely thank Dr. Ching-Rong Huang for his kind help with mathematical modeling. His gentle suggestions were valuable to the theoretical analysis of the flow pattern in the mixing vessels.

I would also like to express my sincere thanks to Dr. Gordon A. Lewandowski, Dr. Dimitrios P. Petridis, and Dr. Ronald S. Kane for serving as Committee Members.

I would also like to express my special thanks to Mr. Lian-Kuo Liang and EE and ME shop at NJIT, for their enthusiastic assistance in the maintenance of the laser-Doppler velocimeter. I would like to give credit to the computer service department at NJIT and Fluent, Inc., for their thoughtful suggestions in the numerical simulation.

I received plenty of encouragement and assistant during this study. To these friendly people, I would like to give my deep appreciation. The following are some of them: Dr. Joseph Bozzelli, Mr. Gwo-Ming Chang, Ms. Chu-Feng Wei, and Mr. Yogesh Gandhi.

Finally, I would like to express my appreciation to my wife for her patience and carefulness, and to my parents for their considerate support and enduring patience through my studying at New Jersey Institute of Technology.

TABLE OF CONTENTS

TABLE OF CONTENTS
(Continue)

LIST OF FIGURES

LIST OF FIGURES
(Continue)

Figure **Page**

LIST OF FIGURES
(Continue)

Figure **Page**

LIST OF FIGURES
(Continue)

LIST OF FIGURES
(Continue)

Figure **Page**

LIST OF FIGURES
(Continue)

Figure **Page**

LIST OF FIGURES
(Continue)

Figure **Page**

NOMENCLATURE

C Impeller clearance off the vessel bottom; m

C_1 Off-bottom clearance for lower impeller (in the two impeller configuration) or for single impeller (in the single impeller configuration); m

C_2 Off-bottom clearance for upper impeller in the two impeller configuration; m

C'_1 Constant used during the numerical simulation of turbulence; non-dimensional

C'_2 Constant used during the numerical simulation of turbulence; non-dimensional

C'_3 Constant used during the numerical simulation of turbulence; non-dimensional

C_D Constant used during the numerical simulation of turbulence; non-dimensional

C_μ Constant used during the numerical simulation of turbulence; non-dimensional

D Impeller diameter; m

Fl Impeller flow number ($Q/N D^3$); non-dimensional

G_k Generation of turbulence kinetic energy, k; kg/m·s^3

H Height of liquid in mixing vessel; m

k Specific turbulence kinetic energy; m^2/s^2

N Agitation speed; rotations/s

N_{cd} Minimum agitation speed for complete liquid-liquid dispersion in mechanically agitated liquid-liquid mixtures; rotations/s

N_{js} Minimum agitation speed for complete particles suspension in mechanically agitated solid-liquid systems; rotations/s

N_p Power number

P Variable defined by equation (3.4)

P_{ij} Variable defined by equation (3.4)

Q Impeller discharge flow rate; m^3/s

r Radial distance from vessel centerline; m

R Radius of impeller; m

S Spacing between impellers; m

T Vessel diameter; m

u Velocity; m/s

$\mathbf{u}$ Velocity vector (m/s)

u_r Radial velocity; m/s

NOMENCLATURE
(Continue)

u_t Tangential velocity; m/s

$\overline{u_t}$ Time averaged tangential velocity; m/s

u_z, u_a Axial (vertical) velocity; m/s

$\overline{\mathbf{u}}$ Time averaged velocity vector; m/s

u_R Time averaged velocity (in rotating reference frame), m/s

u_{Rt} Time averaged tangential velocity (in rotating reference frame), m/s

$\mathbf{u}'$ Fluctuating velocity vector; m/s

u'_i Fluctuating velocity in the *ith* direction; m/s

U_{tip} Impeller tip velocity, m/s

w Vertically projected width of impeller blade (m)

x_i, x_j, x_l Coordinate variables, m

Z Axial (vertical) distance from vessel bottom; m

Z_b Axial (vertical) distance from vessel bottom to bottom of impeller; m

Z^+ Axial (vertical) distance from vessel bottom up to the point on the impeller tip where the radial flow on the impeller side is directed outwards; m

Greek Letters

α Constant used during the numerical simulation of turbulence; non-dimensional

δ_{ij} Kronecker delta

ε Turbulence energy dissipation rate; m^2/s^3

κ Half-angle of incident beams, degree

λ Wavelength of light, mm

μ_t Turbulent viscosity; kg/(m·s)

ρ Liquid density, kg/m^3

σ_k Constant used during the numerical simulation of turbulence; non-dimensional

σ_ε Constant used during the numerical simulation of turbulence; non-dimensional

Ω Angular velocity of the rotating vessel

CHAPTER 1

INTRODUCTION

Mechanically agitated mixing vessels are widely used in a variety of industrial applications such as precipitation, polymerization, fermentation, as well as crystallization and heterogeneous catalysis. As a result, a significant literature exists on the subject, and design principles have been determined for many situations of industrial significance. A comprehensive review of the literature has recently been published (Tatterson, 1991).

The conventional approach to mixing-related problems based on the development of design equations and on the use of dimensional groups and semitheoretical (or empirical) correlations has been proven to be satisfactory in many practical applications. However, this approach is limited in its use since it usually neglect the complexity of the turbulent process at the basis of most mixing phenomena. In addition, this approach cannot provide information about the "micro" scale phenomena of mixing and their impact on transport phenomena and chemical reactions.

Recent instrumentation advancements now allow us to make flow measurements in mixing vessels that could not be made with previous measurement techniques. The laser Doppler velocimiter (LDV) is an ideal device to make these flow measurements because it does not disturb the flow, and has a high-speed, direction-sensitive transducer response.

In addition, computational fluid dynamic (CFD) software programs are now widely available. These programs numerically integrate the basic fluid dynamic conservation equations for mass, momentum and energy and are capable of incorporate turbulence effects in their computations. As a result, we can now measure accurately the flow in complex tridimensional systems, such as mixing vessels, and try to predict the flow distribution numerically. This opens the possibility of developing improved mathematics models to successfully scaling up reactors. The scale-up can include linking flow patterns

of a mixer to the final reaction results and simultaneously determining the mechanical loads imposed on the structures.

In order to gain a more fundamental understanding of micromixing phenomena, a more detailed knowledge of the characteristics of the flow, including is turbulent characteristics, is necessary. Therefore, *the objective of this work is to experimentally determine and numerically predict the flow field in mixing vessels, including its fluctuating component, as a function of the type of impeller and the geometric characteristics of the system.* In this study, the flow fields and turbulent characteristics in both unbaffled and baffled mixing vessels combined with single or multiple flat blade turbines (FBT) and or pitched blade turbines (PBT) are examined. For each mixing configuration, the flow field was experimentally determined using a LDV and the results so obtained compared with the predictions obtained through the use of Computational Fluid Dynamics (CFD) software package.

CHAPTER 2

LITERATURE SURVEY

The flow field inside mixing systems has been the subject of a number of studies over the years. However, only over the last decade has this field of study really benefited from two major technical advances, namely Laser-Doppler velocimetry (LDV) and Computational Fluid Dynamics (CFD). In general, a satisfactory agreement between the LDV measurements and numerical simulations was reported. However, most of the limited number of studies available focused on either the computation aspect or the LDV component of the problems. In addition, most of the literature reviewed covered the field of mixing in baffled single impeller vessels. Very little information is available to date on mixing processes in multiple impellers system, and no fundamental study on the velocity distribution and turbulent characteristics in such a system is available.

A number of theoretical and semiempirical expressions for the turbulence models have been developed since 1877. For example, the earliest proposal was Boussinesq's eddy viscosity model (1877) which was adopted to correlate the Reynolds stresses with the velocity gradient. Prandtl (1925) also proposed the concept of *mixing length, l,* to describe the properties of the Reynolds stresses. Other investigators (Taylor, 1932; von Karman, 1930; Deissler, 1955) introduced various expressions for the Reynolds stresses. However, Chou (1945) was the first one to derive and present the Reynolds stresses equation from the transport equation. Since 1970 the summaries of turbulent theories were summarized by a number of investigators (Hinze, 1959; Bird et al., 1960; Launder and Spalding, 1972; Rodi, 1984). However, due to the complexity of the theory, limitations of the computer capability, and measurement techniques, the applications of these theories to the field of mixing in agitated vessels were not too numerous until a decade ago.

2.1 Unbaffled Mixing Systems

Nagata et al. (1975) studied the velocity distribution of a six-flat-bladed agitated vessel with Pitot tubes. The impeller was located halfway between liquid surface and vessel bottom. He reported that the tangential velocity components are high relative to the radial and axial components, and that they are almost symmetrical to the impeller axis and also to the plane of impeller rotation. The tangential velocity was found to be proportional to the radius within the forced vortex zone, but inversely proportional to radius outside forced vortex zone.

De Groot (1991) proposed a modified model in comparison to Nagata's model (1975) in predicting the flow field of an unbaffled mixing vessel with a formation of a vortex within the tank, by assuming that the dependence of the velocity to radius (r) in the free zone is not equivalent to 1/r but $1/r^{0.4}$, this leads to a better prediction of the tangential velocity in the mixing vessel when compared to Nagata's model.

2.2 Baffled Mixing Systems

Nataga et al. (1975) reported the flow pattern in a mixing vessel agitated by a 8-flat-blade turbine using Pitot tube. A cross sectional view of the velocity profiles along r-Z plane clearly indicated that a strong axially directed circulation pattern was obtained. He also concluded that the tangential velocity was greatly decreased by insertion of baffles.

Oldshue (1983) used an electrical method to determine both the average and the fluctuating velocities for the radial component in a Rushton turbine agitated vessel. The turbulence intensities along the impeller outflow region had an average value about 0.45. Two recirculated flows were also found above and below the impeller using a streak photography technique.

Chen et al. (1988) reported only experimental LDA results for a Rushton turbine and a four-inclined-blade turbine in baffled mixing systems. By comparing the flow

patterns generated from the Rushton and four-inclined-blade turbines systems, it was confirmed that the axially directed flows was primarily due to the presence of the baffles in the mixing vessel. Although the flow fields were examined extensively, the turbulent characteristics were not presented.

Costes and Couderc (1988a) studied a fully baffled Rushton turbine agitated system by LDA at various agitation speeds. By observing the flow patterns along the r-z plane, they concluded that at higher Reynolds number (27,000-85,000) the non-dimensional distribution of the mean and fluctuating velocities are nearly independent of the Reynolds number.

Costes and Couderc (1988b) conducted an extensive study to determine the power dissipation using both macroscale power measurement and microscale fluctuating velocities. They concluded that the ratio of local average energy dissipation per unit mass to power consumption per unit mass of fluid was 15.6 and 0.38 in the impeller region and in the circulation zone, respectively. Two scale-up criteria based on the turbulent characteristics observed in this study were also proposed.

Wu and Patterson (1989) proposed a relation between two important turbulent parameters, namely, the turbulent kinetic energy k and turbulent dissipation rate ε. This relationship is :

$$\varepsilon = \alpha \frac{k^{1.5}}{w}$$

where α is a characteristic constant, and w is the impeller blade width. This relation is believed effectively correlate k and ε in the impeller region in many mixing problems, and was adopted quite frequently by many investigators (Bakker, 1992; Bouwmans, 1992; Armenante and Chou, 1994).

Ranade and Joshi (1989) produced an LDA study for a series of single pitched-blade turbine agitated, fully baffled mixing configurations. The velocity profiles and turbulent kinetic energy were determined for the top, bottom and side surfaces in the impeller region. The comparison between the measured velocities and numerical prediction were also presented. In general good agreement was obtained when the k-ε model was used, and only the velocity at the bottom of the impeller region was used as the impeller boundary conditions.

Ranade et. al. (1989) presented a comparison between the numerical predictions using the k-ε model and experimental results obtained via LDA for a single pitched-blade turbine in a fully baffled system. The flow data at the bottom of the impeller region consisted of tangential, axial velocities, and k and ε were used as the boundary conditions in the impeller region. However, the radial velocity component on the same plane was not specified and was calculated numerically by their CFD program. Boundary conditions along the vessel wall were specified using the no-slip condition. Good agreement between the experimental results and the numerical prediction was reported.

Mahouast et at. (1989) determined the local Reynolds stresses in a fully baffled Rushton turbine agitated vessel by LDV. The local Reynolds stresses were found to be direction dependent indicating that no homogeneous isotropic turbulence is existed. Any calculations based on isotropic turbulence may lead to the erroneous simulations of the flow pattern. The power consumption was calculated from the fluctuating velocity terms and was found to be about 25% of the total power consumption.

Ranade and Joshi (1990a) studied a baffled disc turbine agitated vessel using LDA. They concluded that in the impeller swept volume the energy dissipation rate was found to be about 30% of the total input rate. The effect of the vessel diameter to the flow characteristics was reported to be minimal. Locally isotropy in the bulk region was also presented in this study.

Ranade and Joshi (1990b) conducted the simulations of a baffled disc turbine system with k-ε model. Good agreement between the experimental data and the numerical results was presented. However, some characteristic constants were reported to be sensitive to the model prediction.

Costes et al. (1991) conducted a study in fully baffled, Rushton turbine agitated systems and compared the results obtained using two measurement techniques, i.e., thermal anemometry (TA) and laser Doppler anemometry (LDA). It was confirmed that LDA could produce more accurate data than TA. The radial velocity and turbulence intensity in the impeller discharge stream along tank radius were also presented .

Jaworski et al. (1991) studied the flow in fully baffled pitched-blade turbine agitated system by LDA. They found that near the tank base, the impeller off-bottom clearance influenced decisively the flow pattern. The locally isotropic turbulence characteristic was found to be prevalent throughout the mixing tank except in the impeller outflow stream. The flow number in this study was reported to be about 0.7 for (w/D) equal to 1/5. No simulation was reported in this works .

Kresta and Wood (1991) used a swirling jet model (SRJ) to predict the turbulence quantities k and ε, and the mean velocity components in the region outside a Rushton turbine in a mixing vessel. The results showed a good agreement between the experimental data and the numerical predictions. Comparison of these predictions with others investigators' results were also included.

Weetman (1991) studied a propeller type impeller (Lightnin A410) in a fully baffled mixing vessel using both LDA and CFD techniques. His Results indicated that blending time decreased with increasing of attack angle of the impeller. At Reynolds number higher than 700 the flow was found to be axially dominated while at lower Reynolds number (<200) the flow was radially dominated. The actual data used as boundary conditions in the simulation were not reported.

Hirata et al. (1991) studied a fully baffled single Rushton turbine agitated system using LDA. The tangential and axial velocity components along the radius of the vessel were reported. However, the radial components was not shown. The variation of tangential velocity at the same liquid level between two baffles was reported to be very small. No simulation work was reported in this study.

Renade et al. (1992) reported LDA results for fully baffled pitched-blade turbine (30 °-60°) configurations. In this study, three velocity components and the turbulent kinetic energy (k) in the impeller region were measured. As boundary conditions the velocity profiles on the bottom layer of the impeller region were used. Good agreement between the experimental results for the axial component and the numerical predictions was reported. However the tangential and radial components of the velocity were not compared. A flow number of 0.85 for the 45° pitched blade turbine with (w/D) (ratio of actual impeller blade width to impeller diameter) equal to 1/5 was reported.

Bakker (1992) conducted a series of studies for a single turbine in an agitated, fully baffled mixing vessel with either a LIGHTNIN A315 turbine, a standard 45° pitched blade turbine (6 blades), or a disc turbine. *Fluent* was used to simulate the flow pattern using boundary conditions (tangential and axial velocities, k and ε) specified at the bottom of the impeller region. A relation between k and ε was adopted from Wu and Patterson (1989). The algebraic stress model (ASM) was used. Good agreement between the experimental results and numerical prediction was reported. However only the comparisons for axial component were indicated.

Bouwmans (1992) studied a fully baffled, single 45° pitched-blade turbine mixing system. The flow simulation used the same boundary conditions as in Bakker's case(1992). Only the simulated flow patterns were reported. No comparison between the experimental results and the numerical prediction were indicated.

Dyster et al. (1993) studied a fully baffled Rushton turbine system. The radial velocity components in the impeller discharge stream was proposed to be proportional to

the -0.94 power of (r/R) (dimensionless radial position). The impeller flow number in this particular case was reported to be about 0.78 for Reynolds numbers greater than 10,000.

Kresta and Wood (1993a) compared different methods to estimate the turbulent dissipation rate in mixing tanks. Four types of methods were discussed in this study. They are: gradient hypothesis, Taylor's hypothesis, dimensional argument, and autocorrelation coefficient. The first two methods were suggested to be inferior to the latter two in estimating the dissipation rate.

Kresta and Wood (1993b) determined the flow field produced by a 45° pitched blade turbine with four blades in a fully baffled vessel. Extensive data for the tangential, axial, and radial components of the velocity at various positions below the impeller were given. The average flow number was found to be 0.7.

CHAPTER 3

THEORETICAL EQUATIONS USED IN THE NUMERICAL SIMULATION

To predict the flow created by a rotating impeller, two types of reference frames can be used, namely a stationary frame of reference and rotating frame of reference. The stationary reference frame assumes a stationary vessel wall with respect to the rotating impeller, while the rotating reference frame assumes a rotating wall with respect to a stationary impeller. For the case of an unbaffled tank with a smooth wall, the boundary conditions along the wall can be easily assumed using the rotating reference frame. On the other hand, in the case of baffled vessels the stationary reference frame is typically chosen. Details about these two reference frames will be examined in the following sections.

Independently of the simulation method used the vessel was always assumed to be symmetric along its axis. *Fluent* was run assuming using a repeated 60° and 90° domain for unbaffled and baffled configurations, respectively. The domain always contained about 25,000 cells.

3.1 Stationary Reference Frame

Numerical simulations were conducted to determine the velocity profiles inside the vessel. A commercial CFD finite difference software package (*FLUENT*, Version 3.03) was used for this purpose. This program uses a finite difference approach to solve the steady-state, time-averaged continuity and momentum equations in turbulent regime (Tatterson, 1991).

$$\nabla \cdot \bar{\mathbf{u}} = 0 \tag{3.1}$$

$$\nabla \cdot \left(\rho \bar{\mathbf{u}}\, \bar{\mathbf{u}}\right) = \mu \nabla^2 \bar{\mathbf{u}} - \nabla \bar{p} + \rho \mathbf{g} - \nabla \cdot \left(\rho \overline{\mathbf{u}'\, \mathbf{u}'}\right) \tag{3.2}$$

Both the k-ε model and the algebraic stress model (ASM) were used to account for turbulence effects. Accordingly, the Reynolds stresses $\rho\overline{\mathbf{u}'\mathbf{u}'}$ were modeled, respectively, as:

$$\overline{u_i' u_j'} = \frac{2}{3}\delta_{ij} k - \frac{\mu_t}{\rho}\left(\frac{\partial \overline{u_i}}{\partial x_j} + \frac{\partial \overline{u_j}}{\partial x_i}\right)$$

or

$$\overline{u_i' u_j'} = \frac{2}{3}\delta_{ij} k + \frac{C_D}{\frac{P}{\varepsilon} - 1 + C'_3}\frac{k}{\varepsilon}\left(P_{ij} - \frac{2}{3}P\delta_{ij}\right) \tag{3.3}$$

where (Creare.x, 1991; Launder and Spalding, 1972):

$$P = \frac{1}{2}P_{ii} \qquad \text{and} \qquad P_{ij} = -\overline{u_i' u_\ell'}\frac{\partial \overline{u_j}}{\partial x_\ell} - \overline{u_j' u_\ell'}\frac{\partial \overline{u_i}}{\partial x_\ell} \tag{3.4}$$

The turbulent viscosity was obtained from (Rodi, 1984):

$$\mu_t = \rho C_\mu \frac{k^2}{\varepsilon} \tag{3.5}$$

The values of the specific turbulence kinetic energy, k, and the turbulence energy dissipation rate, ε, were obtained from their balance equations:

$$\mathbf{u}\cdot\nabla k = \nabla\left[\left(\frac{\mu_t}{\rho\sigma_k}\right)\nabla k\right] + \frac{G_k}{\rho} - \varepsilon \tag{3.6}$$

$$\mathbf{u}\cdot\nabla \varepsilon = \nabla\left[\left(\frac{\mu_t}{\rho\sigma_\varepsilon}\right)\nabla \varepsilon\right] + C'_1\frac{\varepsilon}{k}\frac{G_k}{\rho} - C'_2\frac{\varepsilon^2}{k} \tag{3.7}$$

where:

$$k = \frac{1}{2}\left(\mathbf{u}'\cdot\mathbf{u}'\right) \tag{3.8}$$

and:

$$G_k = -\rho\overline{\mathbf{u}'\mathbf{u}'}:(\nabla\mathbf{u}) \tag{3.9}$$

The values of the constants C'_1, C'_2, C'_3, C_D, C_μ, σ_k and σ_ε were taken to be equal to 1.44, 1.92, 0.55, 0.45, 0.09, 1.0, and 1.3, respectively (Rodi, 1984).

The boundary conditions imposed on the systems were as follows. The boundary conditions at the vessel cylindrical wall, baffles, and horizontal bottom were those derived assuming no-slip condition. This implied that the shear stress near the solid surfaces was specified using wall functions and that equilibrium between the generation and dissipation of turbulence energy was assumed (Launder and Spalding, 1974; Ranade *et al.*, 1989). The boundary conditions at the top (free surface) were of the zero-gradient, zero-flux type, which is equivalent to a frictionless impenetrable wall. The common symmetry boundary conditions were assumed at the symmetry axis (Ranade *et al.*, 1989). The program setup for the numerical simulation of unbaffled and baffled configurations are indicated in Appendices B and C, respectively.

In the unbaffled mixing vessel with a single FBT or PBT, and in the baffled mixing vessel with a single PBT, the boundary conditions in the impeller region were imposed at one or more of the surfaces of the cylinder having the same size of the volume swept by the impeller. In particular, either one of two different sets of boundary conditions (named B.C. #1 and B.C. #2, respectively) was imposed in any given simulation. When B.C. #1 was used the time-averaged tangential and axial fluid velocities at the bottom surface of the region swept by the impeller(s) were specified, while all the other cells (including those in the impeller volume) were treated as "live" cells whose velocities were determined by the simulation. The k values along the same surface were also specified, as well as the corresponding values of ε, calculated from:

$$\varepsilon = \alpha\frac{k^{1.5}}{w} \tag{3.10}$$

where α was taken to be equal to 1.4 (Wu and Patterson, 1989; Armenante *et al.*, 1994). The boundary time-averaged velocities and the fluctuating velocities necessary to calculate k were experimentally determined using the LDV system, as described below. Similarly, when B.C. #2 was used the tangential and axial velocities and the corresponding k and ε values were specified at the top and bottom surfaces of the impeller region. The simulations of the baffled agitation systems for the single FBT, double-FBT, double-PBT, and combination of PBT and FBT were always conducted with B.C. #2, using the experimentally obtained velocities for the impeller region as boundary conditions.

3.2 Rotating Reference Frame

A frame of reference rotating with the vessel can be especially useful in unbaffled mixing vessel configurations. This is because the smooth boundary conditions along the unbaffled tank wall can be specified without LDV measurement. In the rotating reference frame, the impeller is at rest and the tank wall is rotated at an angular velocity equal to-$\boldsymbol{\Omega}$. The fluid velocity predicted in the rotating reference frame, $\mathbf{u_R}$, can be related to that in the stationary reference frame as:

$$\mathbf{u} = \mathbf{u_R} + \Omega \times \mathbf{r} \tag{3.11}$$

Fluent incorporates this relation into the momentum equation, in which the additional terms involving $\boldsymbol{\Omega}$ describe the acceleration of the fluid due to the acceleration of the rotating reference frame. The tangential velocity in the stationary reference frame can be obtained from the corresponding velocity in the rotating reference frame using the following reverse transformation:

$$u_t = u_{Rt} + \Omega \times r \tag{3.12}$$

All other velocity components are not affected by the transformation of the reference frame.

Whenever the simulation is conducted with the rotating reference frame, the cells closest to the wall are assumed to have the same tangential velocity as the rotating wall. The other two velocity components and the turbulence parameters are assumed to be zero at those cells. After completing the simulation in the rotating reference frame, a transformation back to the stationary reference frame is conducted.

CHAPTER 4

EXPERIMENTAL APPARATUS AND PROCEDURE

4.1 Mixing Tank Configurations and Impeller Types

Three agitated vessel systems were used in this work: two of them were unbaffled and one was baffled. The first (closed) unbaffled system consisted of an unbaffled, cylindrical, flat-bottomed, plexiglas vessel provided with a flat lid, and completely filled with water (the fluid used in all the experiments) up to the lid, leaving no head space (Figure 4-1). This arrangement prevented the formation of the vortex typically observed in unbaffled systems. The vessel had an internal diameter, T, and a liquid height, H, equal to 0.29 m and 0.32 m, respectively. The second (open) unbaffled system (not shown) was identical to that shown in Figure 4-1 with the exception of the lid, which was absent. Hence, when the liquid was agitated a vortex could be observed.

The baffled system was similar to the open unbaffled system except for the presence of four baffles (width: 29 mm i.e., 1/10 of tank diameter) located 15 mm off the tank bottom (Figure 4-2). These four baffles prevented the formation of the vortex. The vessel had an internal diameter, T, and a liquid height, H, equal to 0.29 m and 0.36 m, respectively.

As indicated in the figures, D was the impeller diameter (0.1016 m), C was the clearance between the blade center of the impeller and the bottom of the vessel, and S was the distance between two impellers' centers. The agitated cylindrical mixing vessel was surrounded by a square cross-section tank (0.4 m by 0.4 m by 0.4 m), also made of Plexiglas, so as to minimize diffraction of the incoming laser beams.

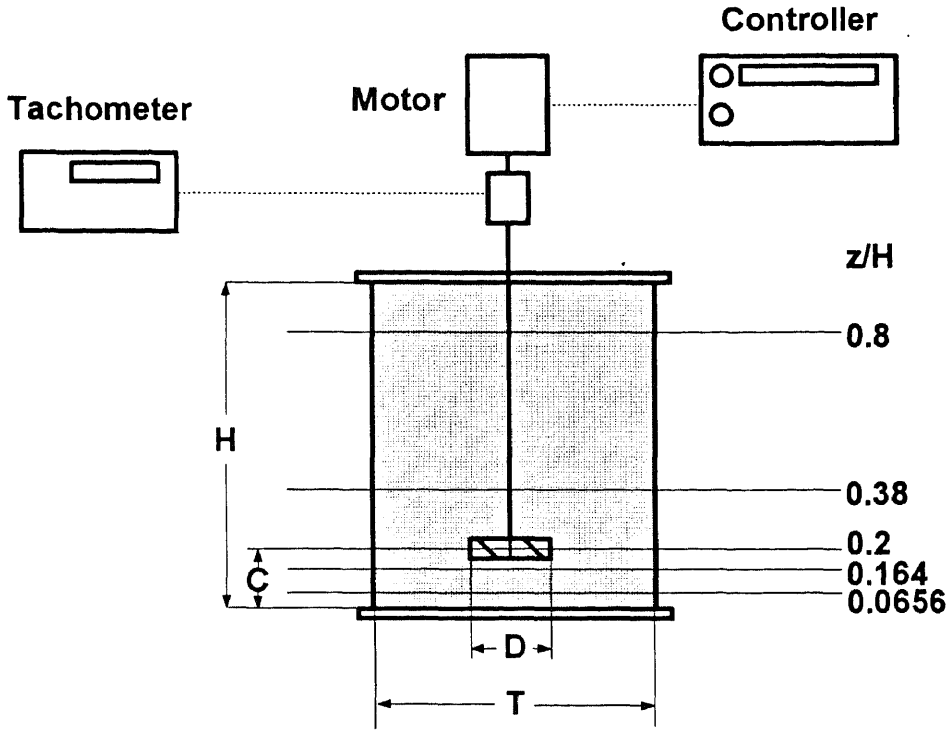

Figure 4-1. Experimental Mixing Apparatus for Unbaffled Configuration

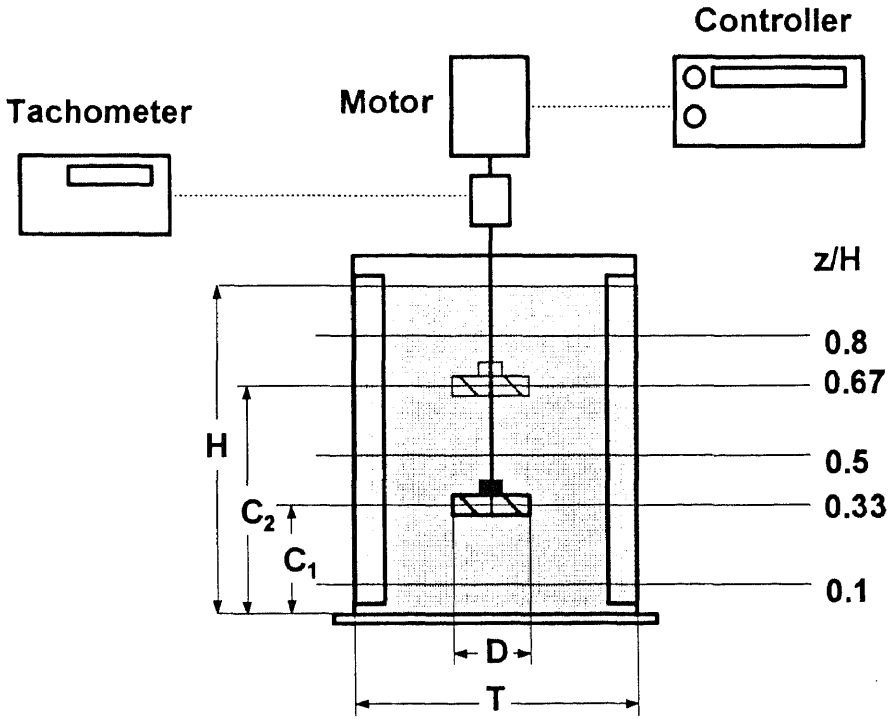

Figure 4-2. Experimental Mixing Apparatus for Baffled Configuration

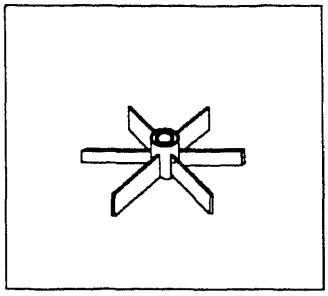

Figure 4-3. Flat Bladed Turbine (FBT)

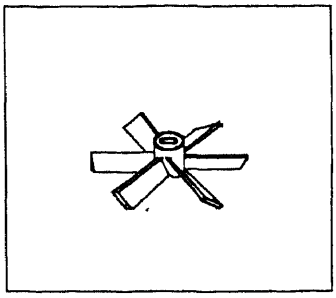

Figure 4-4. Pitched Bladed Turbine (PBT)

Both a 6-blade, flat blade turbine (FBT) having a diameter of 0.1016 m and a blade width of 12 mm, and a 6-blade, 45° pitch-blade turbine (PBT) having a diameters of 0.1016 m and a projected blade width of 13 mm (as seen from the side) were used in this study. They are shown in Figure 4-3 and Figure 4-4, respectively. The impellers were driven by a centrally mounted 1/8 hp motor controlled by an external controller. The agitation speed were set at 100 rpm, 300 rpm, and 500 rpm in the experiments with different impeller clearances. The clearance, C, of the impeller off the tank bottom (in the experiments with one impeller only) was varied only in the closed unbaffled tank system (C/D equal to 0.285, 0.5711, 0.862 and 1.427, respectively). In the experiments with baffled vessels the agitation speed was always 300 rpm and the clearance of the (lower) impeller off the tank bottom was constant and equal to 0.12 m. In this system experiments were conducted in which one or two impellers were used. In the latter case the distance between the impellers, S, was varied (S/D equal to 0.591, 0.886, and 1.181, respectively).

4.2 LDV Apparatus and Experimental Procedure

4.2.1 Detection Principles

A schematic of the laser Doppler velocimeter (LDV) is shown in Figure 4-5. This instrument measures the velocity of a moving object by detecting the Doppler shift of the

light scattered by the object. In flow measurements, the "object" is generally a particle closely following the liquid flow.

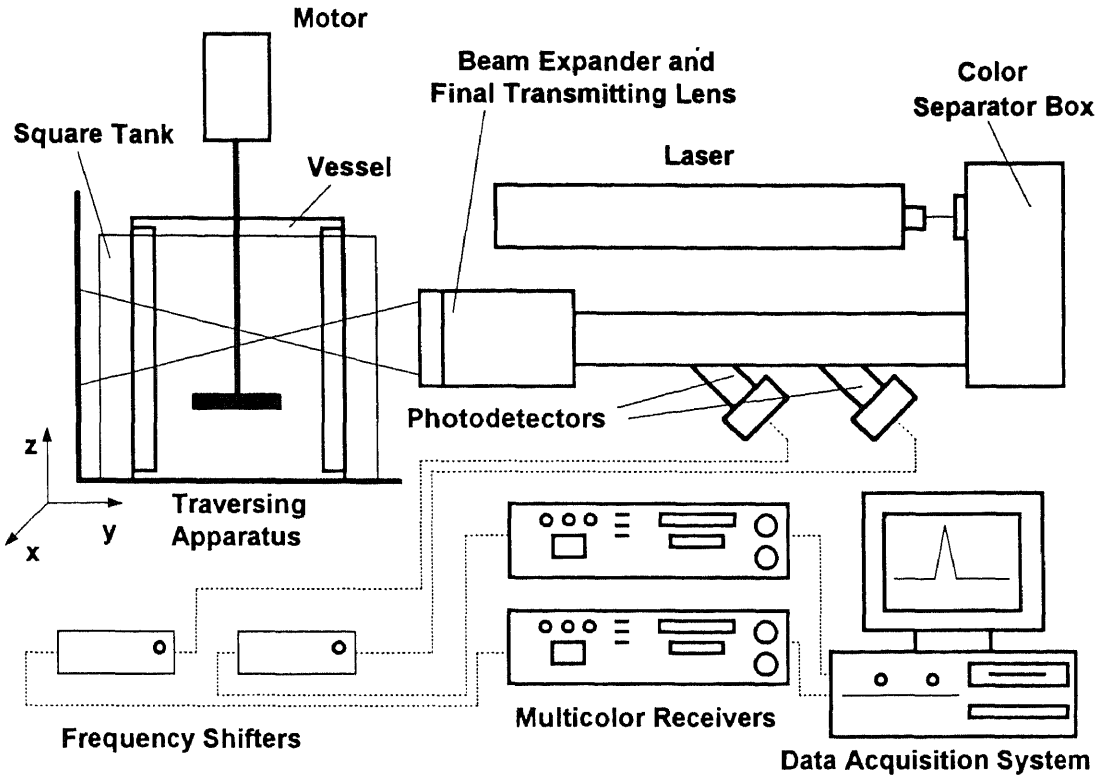

Figure 4-5. Laser-Doppler Velocimetry Apparatus

The velocity and turbulence intensity profiles inside the vessel were determined using the LDV apparatus shown above. The apparatus consisted of a multicolor 2-Watt laser producing a beam that was passed through a color separation assembly box containing several prisms, mirrors, and light attenuators. Only two beams (a green beam and a blue one) emerged from this box. The beams were passed through an optical train splitting them into four beams that were focused by a beam expander and the final transmitting lens on a single point 480 mm away from the final lens (i.e., at a distance equal to the focal distance of the final transmitting lens). The focusing point where the beams converged had an 84 μm diameter formed by the intersection of the four beams, and was always

within in the fluid contained in the mixing vessel in order to take a velocity measurement. The water in the vessel was seeded with 1.5 μm silicon carbide particles. The light scattered by the particles as they traveled through the control volume was collected by the receiving optical assembly working in backscatter mode. The Doppler shift (directly proportional to the particle velocity) was measured with photodetectors. Frequency shifters were mounted on the optical train to allow reverse flow to be measured. Two multicolor receivers connected to a computer system were used for data acquisition.

The alignment and operation procedures for LDV (TSI) apparatus are shown in Appendix D.

4.2.2 Calibration of LDV System

The calibration procedures were conducted prior to LDV measurements. The calibrating method used was to focus the laser beams on a disk rotating at a known constant speed. Aligning the LDV system to measure the surface speed of a defined diameter of the disk gives a direct calibration. For example, the known rotational speed on the outer horizontal plane of the rotating disk can be used to calibrate the local axial velocity (green light) local radial velocity (blue light), vice versa for the vertical plane of the rotating disk.

4.2.3 Data Processing

The photodetector output is a frequency that varies with particle velocity. To convert this to a voltage or "number" proportional to velocity requires some type of frequency converter. The intermittency of the signal, noise, variable amplitude and high frequencies require sophisticated electronics to properly convert the frequency to a voltage or number that is more directly usable.

In this study, a counter type of processor was used which measured the time, τ, for n cycles of the Doppler signal. The frequency is then calculated from $f_D=n/\tau$. Since the time τ is generally measured with a digital clock, the fundamental output of a counter is a

digital word proportional to the time for n cycles. The value of n may either be fixed or varied and output as another digital word.

On a counter, input filters are provided and set to filter out the "pedestal" and as much of the noise as possible without restricting the Doppler signal. When very wide dynamic ranges are encountered, it is often necessary to use frequency shifting to permit effective filtering of the pedestal component. This is particularly true when the optics gives relatively few fringes (cycles) in the measuring volume.

Figure 4-5 shows the data acquisition system. The backscattered Doppler frequencies are amplified by the photodetectors, received and conditioned by the counters. These signals were then transformed into velocities by LDV Data Analysis Software.

4.2.4 Experimental Procedures

The LDV system was used to experimentally determine both the average and fluctuating velocities (and hence turbulent intensities) at 8 radial distances (2r/T equal to 0.114, 0.227, 0.335, 0.44, 0.55, 0.65, 0.76, and 0.86, respectively) and 5 different heights (Z/H equal to 0.0656, 0.164, 0.2, 0.38, and 0.8, respectively) in the unbaffled mixing vessel, as shown in Figure 4-1. For baffled mixing vessel measurement points at 8 radical distance (2r/T equal to 0.11, 0.186, 0.262, 0.338, 0.414, 0.51, 0.683, and 0.841, respectively) and 5 different heights (Z/H equal to 0.1, 0.33, 0.50, 0.67, and 0.80, respectively) were taken, as shown in Figure 4-2.

In order to measure three velocity components using two colors LDV, typically two measurements were taken for each point at a generic radial distance, r, and height, Z: one in which the laser was oriented perpendicularly to the radius along which the measurement was made and another in which it was parallel, as shown in Figure 4-6. This enabled all the three velocity components to be measured at any location.

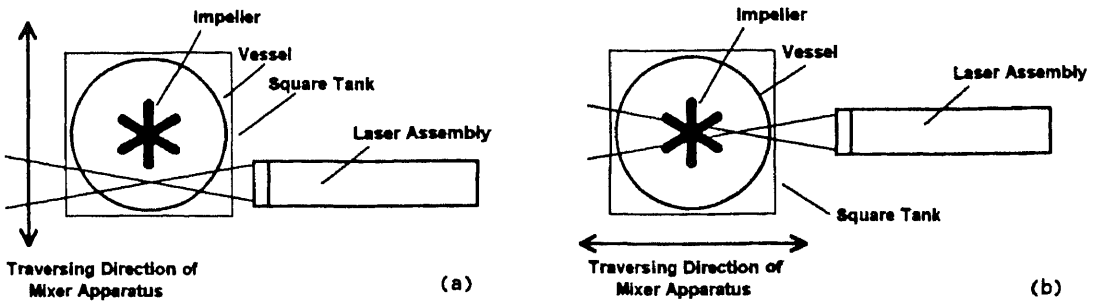

Figure 4-6. Position of the mixing vessel with respect to the laser assembly to measure all three velocity components at the same location: (a). radial and axial velocities are measured; (b). tangential and axial velocities are measured.

CHAPTER 5

RESULTS AND DISCUSSION

5.1 Unbaffled Single-FBT Configuration

5.1.1 Velocities in the Impeller Region

In this study the impeller was positioned at (C/T) = 0.2 and rotated at a speed of 300 rpm. The process fluid was filled up to top of the vessel and covered with a lid. The velocities in the tangential, axial, and radial directions were experimentally determined via LDV for the top and bottom layers of the cylindrical region swept by the impeller. These experimentally determined velocities are reported in Figures 5-1a and 5-1b (App. A). Each point in these figures represents the average of at least two measurements. The results of these figures indicate that the flow in the impeller region had a strong tangential component across the entire top and bottom surface of the impeller region, and that this velocity had a numerical value approximately in the range 0.25-0.35 of the impeller tip speed. The tangential velocities of the bottom layer were slightly larger than those of the top layer.

The results for the axial velocity in the impeller region show that the impeller produced a consistent pumping action in the downward direction. The flow across the top and bottom layers were calculated to be 537 mL/s and 685 mL/s. However, when the radial velocities along the side surface of the impeller, as indicated in Figure 5-2a (App. A) were included the mass balance in the impeller region could be closed within 6 %. It should be noticed that the absolute values of these velocities were quite small, especially when compared with the tip speed (typically less than 10% of the tip speed).

The radial velocity component at the top and bottom of the impeller region was always found to be very small when compared to the tangential component. The reason

for this resides in the absence of either baffles or a vortex preventing the formation of a strong recirculation flow in either the radial or the axial direction.

The intensity of the turbulent kinetic energy in the same impeller region (obtained through the experimental measurement of the fluctuating velocity components) is shown in Figure 5-3 (App. A). The kinetic energy was found to be relatively constant across both the top and bottom surface layers except for a peak in correspondence of $r/R = 0.4$. This result does not appear to be attributable to any kind of experimental error since additional experiments were conducted to confirm these results. In addition, other investigators (Ranade and Joshi, 1989) working on entirely different systems also reported similar significant peaks for the kinetic energy values around the impeller. The values for the velocity components (tangential and axial) and for k shown in the above figures were used as boundary conditions for the numerical simulation resulting in the velocity profiles inside the vessel.

5.1.2 Velocities Outside the Impeller Region

The results of the numerical simulation are presented in Figures 5-4, 5-5, and 5-6 (App. A). Figure 5-4 shows a comparison between the experimental data for the tangential velocities at different positions inside the vessel and the corresponding values obtained from the numerical simulation. One can see that the agreement is quite good for all the cases examined here (i.e., all the different Z/H values). This figure also shows that the tangential velocity is relatively independent of the radial position or the axial position within the vessel, indicating that the vessel's content rotates as a solid body around the shaft.

Figures 5-5a and 5-5b (App. A) show a comparison between the experimental data and the numerical simulation results for the axial velocity component and the radial velocity component, respectively. In these figures the positive direction indicates the

upward direction (for the axial velocity case) or the direction toward the vessel wall (for the radial velocity case). The agreement in these cases is as good as in tangential velocity case (Figure 5-6, App. A). However, it should be emphasized that the absolute values of the radial and axial velocities are quite small.

A comparison of the results obtained in this work with previously published data is impossible because of the lack of data (either experimental or numerical) for similar unbaffled systems. De Groot (1991) experimentally determined the velocity in an unbaffled system without a lid, i.e., in which a vortex was generated. A comparison of his tangential velocity data showed a good agreement with a numerical model and with an earlier model (Nagata, 1975). Satisfactory comparisons between numerical and experimental data have also been obtained by those investigators who studied baffled systems (Ranade *et al.*, 1989; Kresta and Wood, 1991; Weetman, 1991; Bakker, 1992). Therefore, the level of agreement between numerical results and experimental data obtained in this work is comparable with that reported in the literature for other mixing systems. Figure 5-7 (App. A) shows the computational grids and a cross sectional view of the simulation results. As can be seen from Figure 5-7b (App. A) a strong tangential dominated flow pattern is generated. In Figure 5-8 (App. A) both the simulated contours of turbulent kinetic energy and dissipation rate are shown. A strong gradient of both turbulence parameters near the impeller region is observed and is propagated towards the vessel bottom.

In order to understand the effect of the impeller off bottom clearance (C) on the flow fields in the vessel, another experiment was carried out. Figure 5-9 (App. A) shows the effect of the impeller clearance at (C/T) = 0.1, 0.2, 0.3 and 0.5 on the dominated tangential velocities. The ratio u_t/U_{tip} was found to be equal to 0.2 independently of the different impeller off bottom position. This means that the flow pattern is not altered by the impeller position in this unbaffled configuration.

A separate experiment was carried out in the open unbaffled configuration to examine the effect of the vortex on the flow pattern. The C/T ratio was 0.2. Figure 5-10 (App. A) shows the experimental results for the three velocity components within the vessel. As one could see that the flow fields in such a vortex system is still dominated by tangential component. Similar results were also reported by De Groot (1991).

5.1.3 Simulation Using Rotating Reference Frame

The simulations were carried out with the vessel rotating at 100, 300 and 500 rpm, and with single FBT positioned at (C/T) = 0.2. Figure 5-11, 5-12, and 5-13 (App. A) show the corresponding results accordingly. At 100 rpm results of the simulation were acceptable, while at higher rotational speed (300-500 rpm) a more pronounced deviation from the experimental data occurred. Such a deviation increased with the rotational speed. This could be attributed to turbulence effects. At higher rotating speed the turbulence is getting stronger, therefore turbulence parameters along the vessel wall can no more be assumed to be zero. Unfortunately, no general rule is available to date to predict these turbulence parameters near the wall region in the rotating reference frame.

5.2 Unbaffled Single-PBT Configuration

5.2.1 Velocities in the Impeller Region

In this study the impeller was positioned at (C/T) = 0.2 and rotated at a speed of 300 rpm. The process fluid was filled up the vessel entirely. The velocities in the impeller regions were experimentally determined via LDV in order to determine the boundary conditions for the numerical simulation. As mentioned in the section on numerical simulation the average and fluctuating velocities were determined for the top, bottom, and side surfaces of the cylindrical region swept by the impeller. The results for the top and bottom surface, in terms of tangential, axial, and radial velocity distribution, are given in Figure 5-14a and 5-14b (App. A), where each point represents the average of at least two measurements.

The results for the side surface were also obtained but are not shown. These velocities were used to calculate the flow in and out of the impeller region. It was found than the mass balance in this region could be closed quite satisfactorily (ratio of inflow rate to outflow rate = 94.6%). This insured that these velocity values could be reliably used as boundary conditions in the numerical simulation.

The average tangential velocity along the impeller top surface appeared to be constant with respect to the radial position, and equal to about 25% of the impeller tip speed. The corresponding velocity on the bottom surface showed greater scatter. In any case a strong tangential velocity component was observed. The axial velocity on the top surface was always directed downwards (negative direction), as one may expect. On the bottom surface the axial velocity was always directed downwards except for the region near the impeller tip. The radial velocity on the top and bottom impeller surface was always found to be very small with respect to the tip speed.

The values of the turbulence kinetic energy in the same impeller region (obtained through the experimental determination of the fluctuating velocities) are shown in Figures 5-15a and 5-15b (App. A). While the k value on the bottom impeller surface was found to be quite small and nearly constant, that on the top surface showed a significantly greater variability. The experimentally determined velocity and turbulence kinetic energy data for the impeller region were used as boundary conditions for the numerical CFD simulation in the entire vessel.

5.2.2 Velocities Outside the Impeller Region

In Figure 5-16 (App. A) the experimental LDV results for the tangential velocity are compared with the values predicted by *FLUENT* for five different values of the *Z/H* ratio. These predictions were obtained using ASM as a turbulence model and B.C. #2 as the impeller boundary conditions. One can clearly see that the comparison between the

experimental and the numerical results is quite favorable. Figures 5-17a and 5-17b (App. A) show the corresponding comparison for the axial velocity and the radial velocity, respectively. In this case the axial velocity appears to be correctly predicted for Z/H equal to 0.38 (i.e., closer to the impeller) while a deviation between the experimental and the numerical values can be seen for Z/H equal to 0.8 and $2r/T$ values smaller than 0.4. The radial velocity (although small) also appears to be more correctly predicted for Z/H equal to 0.38 than for 0.8, as shown in Figure 5-17b (App. A).

Comparisons between the experimental data for the tangential velocity and the numerical predictions obtained using different turbulence models (ASM or k-ε) and different boundary conditions in the impeller region (B.C. #1, and #2) for two different values of the Z/H ratio (0.38 and 0.8) are shown in Figure 5-18 (App. A). Independently of the axial position it appears that the predictions based on ASM agree more closely with the experimental results than those based on the k-ε model. This is indicated not only by the proximity of the experimental data point to the ASM-based curves but also by the general trend of the curves which is more similar to the experimental data for the ASM curves than for the k-ε model curves. A possible explanation for this can be found in the fact that whereas the k-ε model employs an isotropic eddy viscosity ASM uses an non-isotropic eddy viscosity. This can be important in a system, such as the one under study, in which the flow is highly directional and for which a single value of the eddy viscosity may not be sufficient to adequately describe the turbulent flow.

Figure 5-18 (App. A) also shows that the choice of the boundary conditions has an impact on the numerical results. This is clearly the case for the ASM curve obtained using B.C. #2 which is in much closer agreement with the experimental points than the corresponding curve for B.C. #1. However, the latter curve also appears to follow the same qualitative trend of the former curve. Therefore it can be concluded that, at least for this system, to specify the velocity distribution in the impeller region more precisely has a positive impact on the reliability of the predictions.

A comparison between the results obtained in this work and previous literature is difficult because of the limited availability of data. A direct comparison can only be made with the results recently obtained in a similar closed, unbaffled system using a flat-blade turbine (Armenante and Chou, 1994). It appears that the velocity distribution in the impeller region found in that study is somewhat similar to that reported here, in spite of the different impellers used in the two systems. The reason for this is probably in the absence of baffles, the presence of the lid, and fact that the vessel is completely full. This is likely to reduce the differences between the flow generated by impellers that would normally produce strong radial or axial flow in baffled systems. The two systems also present strong similarities between the flow in the entire vessel. Because of the geometry of the mixing system a flow dominated by a strong rotational component is generated independently of the type of impeller used. As expected, little similarity exists between the pitched-blade impeller system studied here and the corresponding baffled system studied by Jaworski *et al.* (1991).

Finally it appears that the level of agreement between experimental data and numerical predictions obtained in this work is quite good in spite of the fact that the absence of baffle creates a flow that is quite difficult to model unless a non-isotropic turbulence model is used. The results of the predicted flow pattern and the computational grids used in the simulation are shown in Figure 5-19 (App. A). Usually a finer grids is used in the region where strong velocity gradient is expected The cross sectional view of the flow pattern reveals that a strong domination of the tangential velocity existed within the vessel. In Figure 5-20 (App. A) both the simulated contours of turbulent kinetic energy and dissipation rate are shown. A strong gradient of both turbulence parameters near the impeller region is observed and is propagated radially towards the vessel wall.

Another experiment was conducted to examine the effect of the impeller off bottom clearance (C) to the flow pattern in the unbaffled vessel. Figure 5-21 (App. A) shows the tangential velocities at various impeller positions (C/T = 0.11, 0.2, 0.3, and 0.5) along the

vessel radius. It indicates that the tangential velocities are not changed with respect to the impeller position in the vessel, and having the values about 0.2 of the impeller tip speed.

5.3 Baffled Single-PBT Configuration

5.3.1 Velocities in the Impeller Region

The experimentally determined average axial, tangential, and radial velocities in the impeller region are reported in Figure 5-22 (App. A). The axial velocities along the top of the impeller were all directed downward, as one would expect for a PBT-induced flow, and nearly constant for r/R values larger than 0.6 (Figure 5-22a, App. A). Closer to the hub the velocities became progressively smaller and approached the zero value. The corresponding velocities on the bottom face of the impeller were constant for $r/R < 0.7$ and became larger in magnitude beyond that point (Figure 5-22b, App. A). The tangential components were relatively constant and similar in magnitude on both faces. The velocities on the cylindrical surface representing the side of the volume swept by the impeller were also experimentally measured. The velocity profiles in the impeller region observed in this work are flatter than those recently reported by Kresta and Wood (1993b) just below the impeller, or by Ranade *et al.* (1992) 30 mm below the impeller. On the other hand the profiles found here are somewhat similar to those reported by Armenante and Chou (1994) and Armenante *et al.* (1994) for unbaffled systems. A possible explanation for the discrepancies with the results in baffled vessels reported above is that in those studies the baffles extended all the way to the bottom of the vessel, whereas in this work a gap between the baffles and the vessel bottom existed. This could have an impact on the circulation in the region below the impeller making it more similar to that found in unbaffled tanks.

The average velocities on all the surfaces of the volume swept by the impeller were used to calculate the flow rate in and out of the impeller region. A mass balance based on

the experimental velocities around the impeller indicated that the fluid flow rates entering the top face and leaving from the bottom face were $1.90 \cdot 10^{-3}$ m^3/s and $1.78 \cdot 10^{-3}$ m^3/s, respectively. When the contribution of the side surface was taken into account the mass balance could be closed to within 2%, i.e., the total outflow from the impeller region was 98% of the total inflow into the same region. The impeller flow number, *Fl*, was calculated from (Jaworski *et al.*, 1991):

$$Fl \equiv \frac{Q}{N D^3} \tag{1}$$

where Q is the volumetric flow rate discharged from the impeller. This number was calculated from:

$$Q = 2\pi \int_0^R u_z(r)\big|_{Z=Z_b} r\,dr + 2\pi R \int_{Z_b}^{Z^+} u_r(Z)\big|_{r=R} dZ \tag{2}$$

in which the first integral accounts for the flow discharged from the bottom surface of the impeller, and the second integral represents the radial positive flow from the impeller side. In this equation, Z_b is the axial coordinate at the bottom of the impeller (in this work, 5 mm below the impeller for all practical purposes), and Z^+ is the axial coordinate up to which the radial flow on the impeller side is directed outwards. The second integral was evaluated at a radial distance that was as close to R as possible (practically 1 mm). In this work the flow number was found to be equal to 0.36. This value is much lower than the values that other investigators have found for PBT, such as 0.71 (Jaworski *et al.*, 1991), 0.753 (Kresta and Wood, 1993b), 0.75-0.79 (Oldshue, 1983; Table 8-3), and 0.85 (Ranade and Joshi, 1989). However, it should be noticed that all these investigators used PBT with a blade projected width-to-impeller diameter ratio (1/5) much larger than that used in this work (1/8), and that no *Fl* value was found for PBTs geometrically similar to those used here. On the other hand, values for *Fl* similar to that found here have been

reported for curved or convex PBTs (0.39; Ranade *et al.*, 1992), or for square pitch propellers (0.4-0.55; Gray and Uhl, 1966; Oldshue, 1983, Table 8-3). The importance of the *w/D* ratio can be also assessed by examining the literature data on power numbers for PBT having different blade width. The power number has been reported to be equal to 1.67 for PBT having a *w/D* equal ratio of 1/5 (Rewatkar *et al.*, 1990), but only 1.3 for *w/D* equal to 1/8 (Bates *et al.*, 1963; Bates *et al.*, 1966).

The fluctuating velocities in all three dimensions were experimentally determined for the same surfaces in the impeller region and were used to calculate the local turbulence kinetic energy, *k*. The results are given in Figure 5-23 (App. A). Also in this case the curves obtained here for k/U^2_{tip} as a function of *r/R* are flatter than those reported by other investigators (Ranade and Joshi, 1989; Ranade et at., 1992; Kresta and Wood, 1993a), who showed the existence of a peak for *k* for $r/R \approx 0.5$. However, the results found in the present work were more similar to those obtained in unbaffled vessels (Armenante and Chou, 1994; Armenante *et al.*; 1994).

5.3.2 Velocities Outside the Impeller Region

The values of the three experimentally determined velocity components in the bulk of the fluid were are given in Figures 5-24, 5-25, and 5-26 (App. A). In addition, the values given above for the velocities and turbulence kinetic energies in the impeller region were used as boundary conditions in the numerical simulations. The results for these simulations (using different boundary conditions and turbulence models) are also given in Figures 5-24, 5-25, and 5-26 (App. A). In general, a satisfactory agreement can be observed between the experimental results and the simulation curves. This confirms the validity of the experimental determinations of the boundary conditions that were used in the simulations.

The tangential velocity near the tank bottom ($Z/H = 0.1$) is only a weak function of the radial distance (Figure 5-24, App. A). This is probably due to the lack of baffling action in that region caused by the presence of a gap between the baffles and the tank bottom. The agreement between experimental and simulation data in this region is excellent almost independently of the type of boundary conditions and turbulence model. The results for $Z/H = 0.33$ show the effect of the presence of the impeller. The agreement with the simulation is good independently of the turbulence model but not of the boundary conditions. The simulation based on B.C. #2 is clearly superior. In the section of the vessel above the impeller the value of the tangential velocity is small and an acceptable agreement between simulation and experiments can be seen.

Figure 5-25 (App. A) show that near the vessel bottom ($Z/H = 0.1$) the axial velocity is directed downwards for $2r/T > 0.3$, i.e., in the region external to the impeller. Underneath the impeller the flow is close to zero, indicating the presence of a nearly stagnant zone. On the impeller plane the axial velocity is strongly oriented downwards near the impeller ($2r/T > 0.7$) and upwards otherwise. Above the impeller the flow is that typical of an axial impeller, i.e., downwards in the center and upwards at the periphery of the tank. For any of the five heights one can see that the simulation curves follow adequately well the experimental points. The simulation based on B.C. #2 and ASM is slightly superior to the others for any Z/H value.

A comparison between experimental data and simulations is also quite favorable for the radial velocity component (Figure 5-26, App. A) for all Z/H values. Below the impeller a nearly stagnant zone can be again identified. Since the radial and the axial velocities in this zone are both close to zero little exchange of fluid between this zone and the rest of the tank occurs. Only a swirling action is present in this zone because of the high values of the tangential component. In correspondence of the impeller ($Z/H = 0.33$) the radial velocity is also quite modest since the flow is primarily directed downwards, at an angle. The simulations based on B.C. #2 are clearly superior to the others in this

region. In the rest of the vessel the radial velocity is small and directed inwards to form a large recirculation loop above the impeller.

In Figure 5-27 (App. A) the computational grids used in all the simulations of the baffled single-impeller configurations is shown. Figure 5-28 (App. A) shows a tridimensional view of the velocity profiles obtained via simulation (Figure 5-28a, App. A), as well as a bidimensional cross section view across the impeller shaft of the same velocities (Figure 5-28b, App. A). This figures shows the typical top-to-bottom main circulation pattern associated with PBT-generated flows and the presence of nearly stagnant zone (as far as the velocities in the cross sectional plane are concerned) under the impeller. In Figure 5-29 (App. A) both the simulated contours of turbulent kinetic energy and dissipation rate are shown. A strong gradient of both turbulence parameters near the impeller region is observed and is propagated axially towards the vessel bottom.

The results obtained here for a single PBT can be partially compared with the results obtained in the literature for other PBT systems (Ranade and Joshi, 1989; Jaworski *et al.*, 1991; Ranade *et al.*, 1992; Kresta and Wood, 1993b; Armenante *et al.*, 1994). The tangential velocities obtained here for $Z/H = 0.1$ can be approximately compared with those of Ranade *et al.* (1989), who examined the case for which Z/H is equal to 0.668, 0.015 and 0.233, respectively. Their nondimensional tangential velocity for the lowest of these Z/H values is of the order of 0.1, i.e., quite similar to the value found here. However their curve shows a moderate peak for $2r/T = 0.38$ that is absent in the present study. More pronounce peaks appear in their other curves for higher Z/H values. Kresta and Wood (1993b) also produced several curves for the tangential velocities below the impeller. The curve that is closest to the Z/H value used here (0.1) is that for which $Z/H = 0.192$. This curve also shows a peak ($u_t/U_{tip} = 0.2$) for $2r/T \approx 0.27$. The likely explanation for these discrepancies is in the difference in baffling system, which extends all the way to the bottom of the vessel in the case of these two literature studies, but not in this study. In fact, the profile found in the present study is rather similar to that observed

in a similar but closed, unbaffled vessel agitated by a PBT (Armenante *et al.*, 1994). The tangential velocity on the same plane of the impeller was found here to show a marked upward trend near the impeller tip, similarly to previous results for planes under the impeller (of Ranade and Joshi, 1989; Kresta and Wood, 1993b). In particular, the values of the u_t/U_{tip} for $2r/T > 0.33$ were found to be very close to those of Kresta and Wood (1993b) just below the impeller. Comparisons of the tangential velocities above the impeller with other results in the literature are difficult because of the lack of data.

The results obtained here for the axial velocities compare quite favorably with the results of previous literature studies if one takes into account the differences in the geometries of the impeller and the baffles. Ranade and Joshi (1989) produced velocity profiles for the region below the impeller that are similar to that shown in Figure 5-25 for $Z/H = 0.1$. As observed previously, the numerical values of the peaks in their u_a/U_{tip} curves are greater than that found here (0.25 vs. 0.12). However, the impeller they used had a much larger w/D ratio than that used here (1/5 vs. 1/8). A similar argument can be used to interpret the data of Jaworski *et al.* (1991), and Kresta and Wood (1993b), which also show numerical results similar to those of Ranade and Joshi (1989). The curves that the latter authors obtained for the region above the impeller also agree qualitatively with the curves produced here for Z/H equal to 0.5, 0.67, and 0.8.

Previous investigations have shown that the radial component is typically quite small anywhere in the vessel except for the region below the impeller. This is what was found here as well (Figure 5-26, App. A). Significant agreement between the result of this work and the data of Jaworski *et al.* (1991) and Kresta and Wood (1993b) was found. The data of the former workers indicates that the radial velocity is small and directed inwards above the impeller and is directed outwards below the impeller except for the region just under it. This is precisely what was observed here (Figure 5-26, App. A). As before, the major difference between previous literature data and the data of the present work is in the magnitude of the velocities, which is lower here because of the smaller impeller blade

width. The data of Ranade and Joshi (1989) for u_r are also in overall qualitative agreement with the data of this study. However, the agreement between the numerical predictions and the radial velocity data appear to be much better in the present work than in Ranade and Joshi' s work (1989).

5.4 Baffled Double-PBT Configuration

5.4.1 Velocities in the Impeller Regions

The experimentally determined velocities in the upper impeller and lower impeller regions are given in Figures 5-30 and 5-31 (App. A), respectively. As for the single-PBT system the axial velocities were all directed downwards. A comparison between these two figures reveals that the axial velocities on the top surfaces of both impellers are identical for $r/R > 0.7$. For $r/R < 0.7$ the top layer velocity of the lower impeller is nearly flat while that of the upper impeller decrease, in absolute value, toward zero as the ratio r/R becomes smaller. The velocity on the bottom surface of the lower impeller was found to be slightly but consistently higher than the corresponding velocity for the upper impeller. These results indicate that the pumping action of the upper impeller produces a stronger and more homogeneous downward flow across the lower impeller. With the data from Figure 5-32 (App. A) where the radial velocities on the side surface of the impeller are indicated, the mass balance of the flow in and out of both the upper and lower impeller can be closed about 13.8 % difference. An examination of Figure 5-31 and Figure 5-22 (App. A) provides a comparison between the velocities in the same (lower) impeller region in the presence or absence of the upper impeller. The axial velocity profiles for both the top and bottom surfaces appear nearly the same with or without the upper impeller. However, the presence of the upper impeller produces a more constant and smooth axial velocity profile. This is probably the result of a more directionally homogeneous inflow to the lower impeller resulting from the presence of the upper impeller. By comparing Figure 5-30 (for

the upper impeller, App. A) with Figure 5-22 (for the single impeller, App. A) one can see that the axial velocity profiles on the top surfaces have nearly identical shapes, but that the curve for the upper impeller appears translated toward the right. This is probably the result of the shorter distance between the upper impeller and the free liquid surface compared to the single impeller case. A similar comparison for the bottom surfaces shows that the axial velocities are very similar but that the profile for the upper impeller is smoother than that of the single impeller, probably because of the presence of the lower impeller that makes the flow between the upper and lower impeller more axially oriented.

Figures 5-30 and 5-31 (App. A) also reveal that the tangential velocity profiles on the bottom faces of the upper and lower impellers are practically identical. However, a similar comparison for the top surfaces indicates that tangential velocities for the upper impeller are noticeably higher than the corresponding velocities for the lower impeller. This is somewhat counterintuitive since one would expect that a stronger tangential flow in the neighborhood of the lower impeller would be generated in the presence of the upper impeller rather than in its absence. On the other hand a comparison of Figure 5-30 (for the upper impeller, App. A) with Figure 5-22 (for the single impeller, App. A) shows that the tangential velocities on both the top and bottom surfaces are virtually superimposable. This confirms that the flow in the upper impeller region is similar to that observed in a single impeller region. A likely explanation for this is in the weak flow (especially tangential flow) generated by a PBT in the vessel region above the impeller (as shown in Figure 5-28, App. A) which makes the flow near the upper impeller nearly (although not completely) independent of the flow field generated by the lower impeller.

The values of the turbulent kinetic energy at the top and bottom surfaces of the upper impeller and lower impeller regions were calculated from the three components of the fluctuating velocities and are shown in Figures 5-33 and 5-34 (App. A), respectively. A significant difference exists between the k/U^2_{tip} profiles for the two regions. In particular, the k/U^2_{tip} profile for the top surface of the upper impeller was found to be

significantly lower than that for the top surface of the lower impeller. On the other hand, a comparison between Figure 5-23a and Figure 5-33a (App. A) shows no appreciable differences between the top surface k/U^2_{tip} values for the single impeller case and those for the upper impeller case. This indicates that the turbulent flow generated by the upper impeller travels downwards resulting in a higher level of turbulence on the top face of the lower impeller. An appreciable difference exists also between the k/U^2_{tip} values on the bottom surfaces of the upper and lower impellers (Figures 5-33b and 5-34b, App. A), although not as pronounced as in the top surface case. By comparing Figures 5-23b, 5-33b, and 5-34b one can see that the bottom surface k/U^2_{tip} values are rather similar for the single impeller and upper impeller case, but not for the lower impeller case. This again confirms that whereas the upper impeller has a significant impact on the flow and turbulence level in the lower impeller region, the reverse is not true, and that the upper impeller is quite similar to a single impeller as far as flow and turbulence in the impeller region are concerned.

5.4.2 Velocities Outside the Impeller Regions

Figures 5-35, 5-36, and 5-37 (App. A) show the velocity profiles in the bulk of the liquid in correspondence of five different horizontal planes for the double PBT agitation system. Examination of this figures reveals that, in general, a substantial agreement exists between the experimental LDV data and the results of the CFD simulations in which the velocity and turbulent kinetic energy profiles in the impeller regions (Figures 5-30, 5-31, 5-33, and 5-34, App. A) were used as boundary conditions. However, only B.C. #2 was used in the simulations for the double PBT system. Two different turbulence models (k-ε and ASM) were used in the simulations.

As in the single PBT case, the tangential velocity near the vessel bottom ($Z/H = 0.1$) was found to be relatively constant, although significantly smaller in value (about 50%)

than in the former case. This is somewhat counterintuitive since one would expect that the presence of a second impeller would reinforce the flow near the vessel bottom, including the tangential component. The tangential velocity profile for $Z/H = 0.33$ is clearly affected by the presence of the impeller on the same plane, and is very similar to the corresponding single PBT case. However, the velocity profile in the middle of the vessel ($Z/H = 0.5$) is substantially higher in this case, probably because of the upper impeller. The tangential velocity profile at $Z/H = 0.67$ is similar to that at $Z/H = 0.33$, and even more similar to that of a single PBT also at $Z/H = 0.33$. Finally, the profile in the upper region ($Z/H = 0.8$) shows that the tangential velocities above the impeller are only moderately affected by the proximity of the upper impeller and are only slightly higher than the corresponding values for the single PBT case. In any case, the curves in these figures indicate that no significant difference exists between the predictions based on the two turbulence models.

The results reported in Figure 5-36 (App. A) show that the presence of the upper impeller has a significant impact on the axial flow throughout the vessel. The most dramatic evidence of this can be seen near the bottom of the vessel. A comparison between Figures 5-36 and 5-25 (App. A) in correspondence of $Z/H = 0.10$ shows that the axial flow is now directed upwards in the central bottom part of the vessel ($2r/T < 0.7$), and downwards near the vessel wall. This is almost exactly the reverse of the flow produced by a single PBT. While the axial flow in the lower impeller region ($Z/H = 0.33$) is similar to that for a single impeller (Figure 5-25, App. A), the axial velocities between the impellers ($Z/H = 0.50$) are significantly larger in the central vessel region for the case of a double PBT system, which is what one could intuitively anticipate. The axial flow in the upper impeller region ($Z/H = 0.67$) and in the region above that ($Z/H = 0.80$) are clearly affected by the presence of the upper impeller.

As for the radial velocities significant differences exist between the double PBT and single PBT cases in the region near the vessel bottom ($Z/H = 0.10$) where the flow

intensity is much lower in the former case. Also, in the region of the lower impeller ($Z/H = 0.33$) the radial flow is directed outwards in the double PBT case and inward in the single PBT case. In the rest of the vessel no appreciable differences between the two configurations can be seen, except for the region where the upper impeller is located ($Z/H = 0.67$).

The simulated flow pattern generated by two PBTs is given in Figure 5-39 (App. A). A comparison of this figure with the corresponding figure for the single impeller configuration (Figure 5-28, App. A) shows the striking differences in flow pattern resulting from the presence of the second impeller. The main top-to-bottom axial flow is clearly stronger, especially between the two impellers. More significantly, the angled discharge from the bottom impeller is now deflected horizontally before reaching the bottom of the vessel. This produces an expansion of the low circulation region previously observed just under the impeller in the single PBT case, and results in the entire bottom region in the vessel being almost completely cut off from the main circulation loop. In fact, a secondary recirculation loop can be observed in the region comprised between the vessel bottom and wall. This change in the flow pattern is not only counterintuitive but can also have dramatic consequences on some of the typical industrial applications of PBTs, such as the off-bottom suspension of solid particles. Contrary to what one may expect the addition of a second impeller is likely to have (at least in this case) a negative impact on the suspension ability of the agitation system. This would not only result in a higher agitation speed to achieve the same degree of solid suspension, but also in a much higher power consumption caused by the presence of the second impeller. A situation of this kind has been already described in the literature. For example, Armenante *et al.* (1992) have already observed that the presence of two or three impellers instead of one may result in higher agitation speeds and higher power consumption to achieve the same complete particle suspension state in solid-liquid systems (N_{js}), or the complete dispersion state in liquid-liquid systems (N_{cd}). This phenomenon was observed not only with mixed-

flow impellers, such as PBTs, but also with radial flow impellers, such as disk turbines and flat-blade turbines (Armenante *et al.*, 1992; Armenante and Li, 1993). In Figure 5-40 (App. A) both the simulated contours of turbulent kinetic energy and dissipation rate are shown. A strong gradient of both turbulence parameters near the impeller region is observed and is propagated axially towards the vessel bottom.

A separate experiment was also carried out to examine the effect of the impeller spacing (S) to the flow pattern. Figure 5-41, 5-42, and 5-43 (App. A) show the measured tangential, axial, and radial velocities along the vessel radius with respect to the change of the ratio of S/D (ratio of the impeller spacing to impeller diameter). The important region in this study is particularly aimed at the zone between two impellers. Therefore, the horizontal planes at Z/H = 0.416, 0.444, 0.50, and 0.556 were examined. The tangential and radial velocities seem not affected by the impeller spacing. However, the axial velocities show the trend that the closer of the impellers the higher of the pumping action.

5.5 Baffled Single-FBT Configuration

5.5.1 Velocities in the Impeller Region

The experimentally determined average axial, tangential, and radial velocities in the impeller region are reported in Figure 5-44 (App. A). The axial velocities along both the top and bottom of the impeller were all downward directed, and nearly constant for r/R values greater than 0.6. When approaching to the hub the velocities became larger in the downward direction on the top surface, the corresponding velocities on the bottom surface were shown to be nearly constant. The tangential velocities were relatively constant and had a u/U_{tip} value about 0.15. The radial velocities values were shown fluctuate around zero on both the top and bottom surfaces, except those having values almost identical with axial velocities for $r/R < 0.75$ on the bottom surface. A comparison of the results with previous work was found to be difficult. Nagata (1975) reported a similar downward directed velocity profiles for axial velocities with single 8-flat-blade

turbine in a baffled mixing vessel. The radial velocities on the cylindrical surface representing the incoming or outgoing flow on the side of the volume swept by the impeller is shown in Figure 5-45 (App. A). The numerical simulations were obtained using those boundary conditions in the impeller region of the measured average axial and tangential velocities, the calculated k and ε, and by assuming zero radial velocities.

The average axial velocities on both top and bottom surfaces and the average radial velocities on the side surface were used to calculate the flow rate in and out of the impeller region. A mass balance based on these experimental results can be closed to within 4.9%, i.e., the total outflow from the impeller region was 104.9% of the total inflow into the same region. The impeller flow number, Fl, was found to be equal to 0.41. This value is found to be closed to Nagata's 0.34 for 8-flat-blade turbine configuration.

The fluctuating velocities along both the top and bottom of the impeller region for all three dimensions were experimentally determined and used to calculate the local turbulence kinetic energy, k. The results are shown in Figure 5-46 (App. A). The results for the side surface was not used in the numerical predictions, and, it is not included. The dimensionless k/U^2_{tip} values along r/R on the top surface shows a fairly constant value about 0.006-0.008, while along the bottom surface a more scattering nature is observed as for r/R > 0.5 the values is ranged from 0.008-0.018.

5.5.2 Velocities Outside the Impeller Region

Figures 5-47, 5-48, and 5-49 (App. A) show a comparison of the velocity profiles for both experimentally determined and numerically predicted results of three velocity components at five different horizontal planes. In general, a satisfactory agreement can be observed. This confirms the validity of the experimental determinations of the boundary conditions that were used in the simulations.

The tangential velocity near the tank bottom (Z/H = 0.1) was found to be almost constant along the radius. This is probably due to the presence of a gap between the

baffles and the tank bottom. The results for Z/H = 0.33, i.e., at the impeller centerline indicate a strong gradient along the tank radius. While for Z/H = 0.5, 0.67, and 0.8 a less strong gradient is observed.

The axial velocity (Figure 5-48, App. A) near the vessel bottom (Z/H = 0.1) shows a upward directed flow for 2r/T < 0.7, while at Z/H = 0.33 the flow is directed downwards. Two recirculation flows are observed in the zone for Z/H between 0.1 and 0.33.

Figure 5-49 (App. A) shows quite good agreement for the radial velocity components for all Z/H values. Except in the region near the impeller the radial velocity is fairly close to zero. This clearly shows that the flow is mainly dominated by the axial and tangential velocity components.

Finally, Figure 5-50 (App. A) shows a tridimensional view of the velocity profiles obtained via simulation (Figure 5-50a, App. A), as well as a bidimensional cross section view across the impeller shaft of the same velocities (Figure 5-50b, App. A). This figure shows the top-to-bottom main circulation pattern produced by FBT and an induced circulation pattern beneath the impeller. In Figure 5-51 (App. A) both the simulated contours of turbulent kinetic energy and dissipation rate are shown. A strong gradient of both turbulence parameters near the impeller region is observed.

The results obtained in this work can be compared with the observation of Nagata's (1975), in which a main circulation flow was also generated by an 8-flat-blade turbine in a baffled mixing vessel.

5.6 Baffled Double-FBT Configuration

5.6.1 Velocities in the Impeller Region

The experimentally determined velocities in the upper impeller and lower impeller regions are given in Figure 5-52 and Figure 5-53 (App. A), respectively. The axial velocities on the top of both the upper and lower show a fairly constant value of 0.15 and 0.10 of the impeller tip speed, respectively. A slightly greater values for the

corresponding velocities on the bottom of the upper impeller is observed. This indicates that the pumping action of the upper impeller produces a stronger downward flow than the lower impeller. However the axial velocities along the bottom surface of the lower impeller were found to be much smaller than the corresponding velocities for the upper impeller. This implies that a stronger radial pumping is expected. As can be seen from Figure 5-54b (App. A), the radial velocities along the side of the lower impeller are in the outflow direction. The average axial velocities on both top and bottom surfaces and the average radial velocities on the side surface of the upper and lower impeller were used to calculate the flow rate in and out of the impeller region. A mass balance based on these experimental results can be closed to within 8% and 1.1% for the upper and lower impeller, respectively. The impeller flow number, *Fl*, was found to be equal to 0.39 and 0.19 for the upper and lower impeller, respectively. The value of the upper impeller is found to be closed to Nagata's 0.34 for 8-flat-blade turbine configuration. When comparing the tangential velocities of the upper FBT with the single FBT in the impeller region, a similar trend and magnitude can be seen. This confirms that the flow in the upper impeller region is similar to that observed in the single impeller region. The average radial velocity components along both top and bottom surfaces of the upper and lower impeller show a near zero value.

The turbulent kinetic energy, k, at the top and bottom surfaces of the upper and lower impeller regions were calculated from the three components of the fluctuating velocities and are shown in Figure 5-55 and Figure 5-56 (App. A), respectively. In general, a fairly constant value of k/U^2_{tip} along the radius was observed, except for the value on the top of the lower impeller where a drastic change in the turbulent kinetic energy was shown. This indicates that the turbulent flow generated by the upper impeller travels downwards resulting in a higher level of turbulence on the top surface of the lower impeller. The same situation was also observed in the case of double-PBT system (Armenante et al., 1994). When comparing Figure 5-46, 5-55, and 5-56 (App. A) one can

see that the bottom surface k/U^2_{tip} values are rather similar for the single impeller and upper impeller case, but not for the lower impeller case. This again confirms that the upper impeller has a significant impact on the flow and turbulence level in the lower impeller region. The same phenomena was also reported by Armenante et al. (1994) for baffled double-PBT system.

5.6.2 Velocities Outside the Impeller Region

A comparison of the experimental results and numerical predictions for the tangential, axial, and radial velocity components are shown in Figure 5-57, 5-58, and 5-59 (App. A), respectively. In general, a substantial agreement exists between the LDV determinations and CFD simulations were obtained. However, only B.C. #2 was used for two different turbulence models, k-ε and ASM.

The tangential velocities along the tank bottom were found to be gradually decreased with respect to the radius. This trend is somewhat different from the single FBT system where a fairly constant tangential velocity was found. This stronger tangential velocities near the hub may therefore destroy the circulation pattern that existed in the single-FBT system, and result in a swirling flow near the vessel bottom in the double-FBT system. The tangential velocity profile at $Z/H = 0.33$ is similar to that of the single impeller system, but is quite different at $Z/H = 0.5$. This can be attributed to the presence of the upper impeller. The same situation was also observed for $Z/H = 0.67$ and 0.8. In any case, there is no significant difference between the predictions based on the two turbulence models.

A significant impact on the axial velocities throughout the vessel is observed in Figure 5-58 (App. A), when the upper impeller was placed. At $Z/H = 0.1$ a near zero velocity in the axial direction is observed, while at $Z/H = 0.33$ a slightly stronger axial flow compared to the single impeller is indicated. The most prominent changes in the axial flow are at $Z/H = 0.5$ and 0.67 where a very strong pumping action exists. This is what

one could intuitively anticipate. The flow in the region above the upper impeller (Z/H = 0.8) is clearly affected by the presence of the upper impeller. A similar situations were also reported by Armenante et al. (1994) in a double-PBT system.

As for the radial velocities, no significant difference between single and double FBT systems was found. The variation of the radial velocities along the vessel radius was very small. Their values were all near by zero at all the five heights in the mixing vessel.

Finally, the simulated flow for the double-FBT configuration is shown in Figure 5-60 (App. A). As can be seen from Figure 5-60a (App. A) a strong circulated flow pattern exists between two impeller. However, a comparison with the flow generated by a double-PBT system (Armenante et al., 1994) shows a higher off tank bottom circulation pattern. This confirms that the axial velocities were weaker in the double-FBT than in the double-PBT system near the bottom of the impeller region. Placing a second FBT into the system also significantly affects the flow pattern by shifting the circulation flow toward the upper part of the vessel. A swirling flow is dominates the lower part of the vessel. The addition of a second impeller would have a negative impact on solid suspension. This would not only results in higher agitation speed but also in higher power consumption to achieve the same degree of solid suspension. The same conclusion was also reported by Armenante et al. (1992). In Figure 5-61 (App. A) both the simulated contours of turbulent kinetic energy and dissipation rate are shown. A strong gradient of both turbulence parameters near the impeller region is observed.

A separate experiment was also carried out to examine the effect of the impeller spacing (S) to the flow pattern. Figure 5-62, 5-63, and 5-64 (App. A) show the measured tangential, axial, and radial velocities along the vessel radius with respect to the change of the ratio of S/D (ratio of the impeller spacing to impeller diameter). The important region in this study is the zone between the two impellers. Therefore, the horizontal planes at Z/H = 0.416, 0.444, 0.50, and 0.556 were examined. The tangential and radial velocities do no to be seem affected by the impeller spacing. However, the axial velocities show that

the closer the impellers the higher the pumping action is. The same observation was made in the double-PBT system.

5.7 Baffled PBT-FBT Configuration

5.7.1 Velocities in the Impeller Region

The velocity profiles in the impeller region for the three velocity components of both the upper and lower impeller are given in Figure 5-65 and Figure 5-66 (App. A), respectively. The axial velocities on both the top surfaces of the upper PBT and the lower FBT are nearly the same in trend and magnitude for all radial distances. A greater outgoing pumping action from the bottom surface of the upper impeller than the incoming pumping action on the top of the lower impeller is noticed. This can be attributed to the less effective axial pumping action of the lower radial type FBT. When comparing this observation with the results of the radial velocities on the side surface as indicated in Figure 5-67b (App. A), one can confirms that the downwards pumping action of the lower impeller is partly coming from the impeller side. A mass balance around the impeller region was obtained by the measuring average axial velocities on both the top and bottom surfaces, and the radial velocities on the side surface of volume swept by the impeller. The balance can be closed to 4% and 14% for the upper and lower impeller, respectively. The impeller flow number, *Fl*, was found to be equal to 0.37 and 0.30 for the upper and lower impeller, respectively. The value of the upper impeller was found to be closer to the value of 0.36 reported by Armenante et al. (1994), while the value of the lower impeller is close to Nagata's 0.34 for 8-flat-blade turbine configuration.

It also can be seen that the tangential velocities are almost identical on the bottom faces of the upper and lower impeller. However, when comparing the corresponding velocities of the top faces, those of the lower impeller shows grater values than the upper impeller. A further comparison of the velocities of the upper impeller with the single PBT shows that the velocities on both the top and bottom are almost identical. This confirms

that the flow in the upper impeller region is similar to that observed in the single PBT impeller region.

The scattering radial velocities along both the top surfaces of the upper and lower impeller imply that more intense turbulence exists along these surfaces. A more stable values of the same velocities on the bottom surfaces of the upper and lower impeller is also indicated.

The turbulent kinetic energy, k, along the top and bottom surfaces of the upper and lower impeller regions were calculated from the three fluctuating velocities and are indicated in Figure 5-68 and Figure 5-69 (App. A), respectively. As mentioned above, the k values on the top surfaces show a more broaden distributions.

5.7.2 Velocities Outside the Impeller Region

Figure 5-70, 5-71, and 5-72 (App. A) show a comparison between the experimental results and the numerical predictions for the three velocity components. Very good agreement was obtained. However, only B.C. #2 was used as the boundary conditions in the impeller region. Both k-ε and ASM turbulence models were tested.

Near the tank bottom (Z/H = 0.1) the tangential velocities are independent of the radius distance. This can be attributed to the gap between the baffles and the tank bottom. The simulation for Z/H = 0.33 shows slightly off prediction at 2r/T equal to 0.5 for both models. However, for the same radial locations at Z/H = 0.67 the agreement between experimental and simulation data is excellent. A strong velocity gradient at Z/H = 0.5 along the radius distance is observed. Very good agreement between the LDV data and CFD results is also obtained for both turbulence models at this horizontal plane, except for 2r/T > 0.53 where the ASM prediction are depart from the experimental observations. This is probably due to the regional homogeneous turbulence which results in locally off prediction of the ASM model. For Z/H = 0.8 the velocities are relatively independent of the radial distance.

The axial velocities along the radius near the vessel bottom (Z/H = 0.1) are quite small. In comparison to the double-PBT system (Armenante et al., 1994) and the double-FBT system (Armenante et al., 1994) the induced circulation pattern in this region has nearly disappeared. The addition of the second different type of impeller (PBT) has caused the flow in this region to be stagnant. A strong downwards pumping at Z/H= 0.33, 0.5, and 0.67 are clearly indicated. However when compared with the double-PBT system (Armenante et al., 1994) a less stronger downwards pumping action is observed. In this region, both turbulence models predict quite well the experimental results. At Z/H =0.8 which is the region above the impeller, the pumping action is not as strong as in the region between the two impellers.

As for the radial velocity components the results indicate that a nearly zero value for both the experimental and prediction is obtained, which confirms the previous observation of a stagnant zone existed in this region. The radial pumping action of FBT (at Z/H= 0.33) promotes the main circulation pattern, but also reduces the strength of the induced circulation flow near the vessel bottom. As explained earlier, a strong circulation existed between two impellers mainly directed axially, one may expects that a near zero value for the radial components above the lower impeller occurred. In fact, at Z/H = 0.5, 0.67, and 0.8 the experimental radial velocity components actually show a nearly zero value.

Finally Figure 5-73 (App. A) shows the velocity profiles of a tridimensional and a bidimensional view. From the bidimensional view the main top-to-bottom circulation pattern is clearly indicated, yet the induced circulation pattern is disappeared. In Figure 5-74 (App. A) both the simulated contours of turbulent kinetic energy and dissipation rate are shown. A strong gradient of both turbulence parameters near the impeller region is observed.

A separate experiment was also carried out to examine the effect of the impeller spacing (S) on the flow pattern. Figure 5-75, 5-76, and 5-77 (App. A) show the measured tangential, axial, and radial velocities along the vessel radius with respect to the change of

the S/D ratio (ratio of the impeller spacing to impeller diameter). The important region in this study is the zone between the two impellers. Therefore, the velocities in the horizontal planes at Z/H = 0.416, 0.444, 0.50, and 0.556 were examined. The tangential and radial velocities do not to be seem affected by the impeller spacing. However, the axial velocities showed a slightly higher pumping action when the impellers were close.

5.8 Power Consumption

The total power consumption of the each configuration studied above is indicated in Figure 5-78 and Figure 5-79 (App. A). The single impeller agitated system produced a power number (Np) of about 0.5-3.0 at different impeller clearance ratio (C/T). The variation of the power number with respect to rpm is very small. As can be seen from Figure 5-78 (App. A) the baffled configurations always produced a higher power consumption. For the unbaffled systems the FBT configuration also shows a slightly higher power consumption than the PBT configuration. The way in which the power consumption of two impellers system was determined in this work is to fix the lower impeller position while varying the upper impeller position. As one can see from Figure 5-79 (App. A) the power numbers for two impeller systems ranged from 2.0 to 4.5 which is considered to be a reasonable value for such a system. In this study the double-FBT configuration produced the highest power consumption, and the double-PBT system produced the lowest power consumption, regardless of the S/D ratio. The same situation was also observed in the single impeller system. This confirms that FBT-agitated systems always consume more power than PBT system. The power number was a very weak function of the S/D ratio. This also validate the observation of the flow fields was not significantly affected much by the impeller spacing.

CHAPTER 6

CONCLUSIONS

The results of this study indicate that the flow pattern within the mixing vessel can be correctly simulated whenever a set of well defined boundary conditions and a proper selection of simulation techniques are employed. The experimental apparatus (LDV) used in this study to measure the velocities across the vessel was also proven to be very suitable. When comparing the flow fields obtained with and without baffles, it was found that the flow pattern is generated mainly because of the existence of the four baffles within the vessel, as one can see in general, the flow pattern was found to be tangentially dominated in the unbaffled configuration regardless of the type of impeller, while an axial top-to-bottom circulation flow was always observed in the baffled configuration. The ASM model was always superior to the k-ε model in predicting the flow field for the unbaffled configuration. A better prediction was also observed when the velocities at more surfaces around the impeller region were specified as the boundary conditions in the unbaffled configuration. As for the baffled vessels, velocity predictions of the flow fields were, in general, quite good with both ASM and k-ε models. Several important observations follow:

1. In the unbaffled FBT system the axial component is typically much smaller than the tangential component. The radial velocity component is also typically smaller than the axial velocity and one order of magnitude smaller than the tangential component. This is also true even in the neighborhood of the impeller, in contrast to what has been typically observed in baffled vessels in which a turbulent stream is typically ejected radially from radial impellers (Kresta and Wood, 1991.). Significant agreement was observed between the numerical CFD predictions for the tangential velocity (in which an algebraic stress model was used to model

turbulence) and the experimental data. The agreement was less satisfactory for the axial and radial component. However, the CFD simulation was able to capture the trend shown in the experimental data for the radial velocity component.

2. The results obtained in the unbaffled PBT system show that the flow produced by a pitched-blade turbine in an unbaffled vessel with no headspace is strongly dominated by the tangential component of the velocity. In such a geometry the impeller, independently of its type, loses its radial or axial characteristics commonly observed in baffled systems. The flow in the system studied in this work can be adequately predicted by numerical models that use ASM to simulate the effect of the turbulence viscosity, whereas simulations based on k-ε models are less satisfactory. Significant agreement was observed between the numerical CFD predictions for the tangential velocity (in which an algebraic stress model was used to model turbulence) and the experimental data. The agreement was also found to be quite good for the axial and radial components as long as the ASM was used, and the boundary conditions were specified at the top and bottom of the impeller region.
3. The results of baffled PBT(s) system indicate that significant agreement exists between the numerical predictions based on CFD simulations and the LDV experimental values of the tridimensional velocity profiles in baffled vessels agitated with one or two PBTs. Better predictions can be obtained if the boundary conditions used in the simulation are specified at two rather than one of the surfaces of the region swept by the impeller(s). Of the two turbulence models used in this work, i.e., ASM and k-ε, the former produced results in marginally but consistently better agreement with the experimental data than the latter.
4. The results for the baffled single PBT configuration indicate that the flow is dominated by the axial component of the velocity, resulting in a major top-to-bottom recirculation loop characteristic of single PBT flow in mixing vessel. The

introduction of a second PBT produced a significant shift in the flow pattern, generating an even stronger axial recirculation loop in the central and upper part of the vessel, but also creating a secondary recirculation loop in the lower part of the vessel completely extending over the entire bottom of the vessel. Because of low velocities observed in this secondary loop, mixing in this region is likely to be poor. This could result in a significant and negative impact of the presence of the second impeller on phenomena such as off-bottom solid suspension, which strongly depends on the velocity profiles and turbulence intensity in the region near the tank bottom. Hence, caution should be exerted when an additional PBT is added to a single PBT in order to improve the mixing performance of the system.

5. A substantial agreement between the LDV results and CFD predictions for three velocity components in the baffled single FBT system is obtained.
6. With the addition of the second FBT, a strong circulated pattern is formed between the two FBTs. However a comparison with the FBT configuration shows that the presence of the second impeller reduces the intensity of the velocities in the region below the lower impeller.
7. In the configurations where combinations of a PBT and a FBT were used, a fairly good agreement between the LDV results and CFD predictions for all the velocity components across the vessel were found. However, prediction based on the k-ε model were slightly better than those based on ASM model.

APPENDIX A

FIGURES FOR UNBAFFLED AND BAFFLED SYSTEMS

This appendix includes the figures showing the boundary conditions of the impeller region and the comparison between the experimental data and simulation results for both unbaffled and baffled systems.

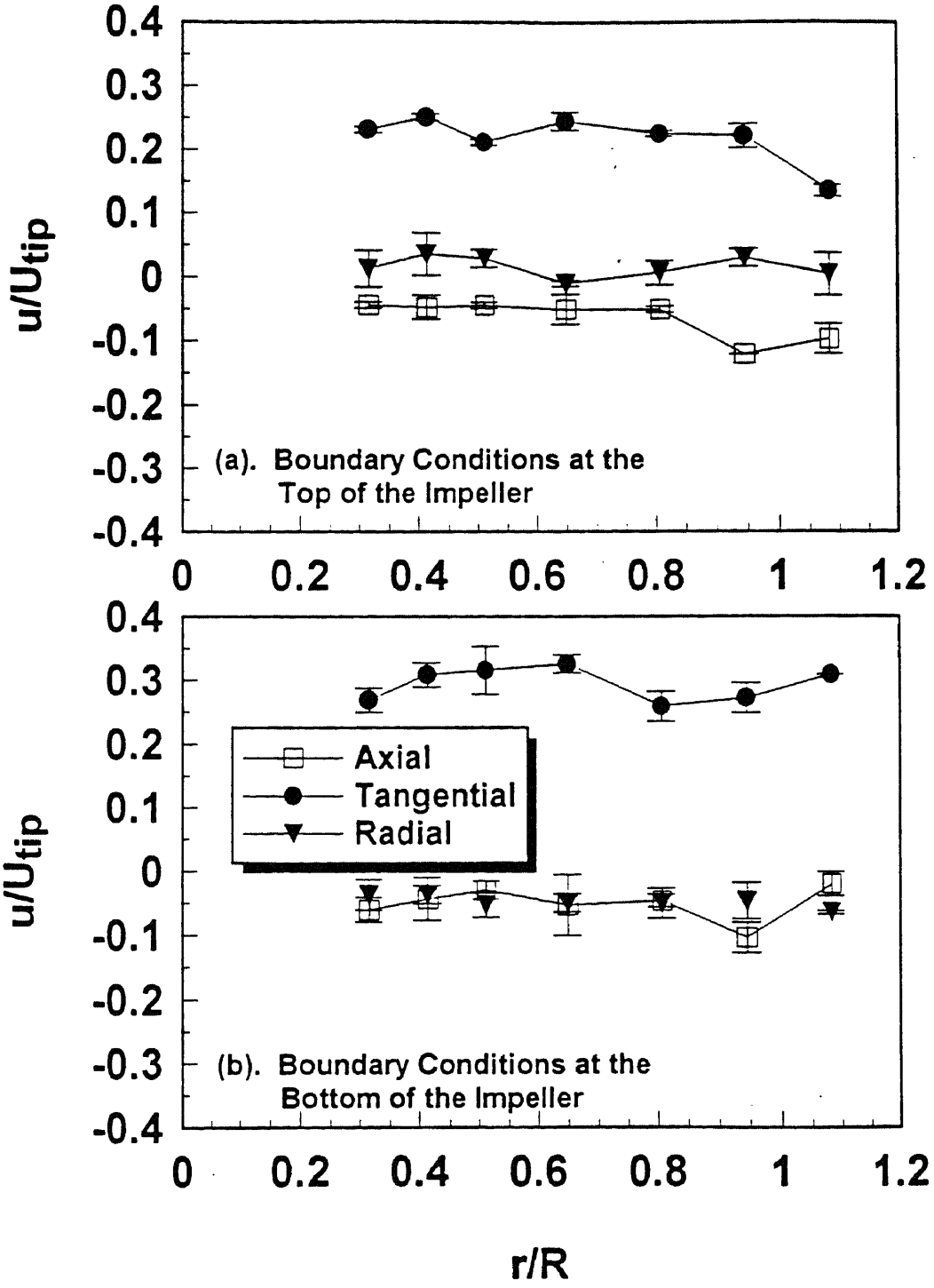

Figure 5-1. Experimentally determined (via LDV) velocities in the impeller region. These values were used as the boundary conditions in the numerical simulation. Unbaffled FBT system: (a) boundary conditions at the top of the impeller; (b) boundary conditions at the bottom of the impeller. Positive values indicate upwards velocities (for the axial direction). Error bars indicate standard deviation of duplicate experiments.

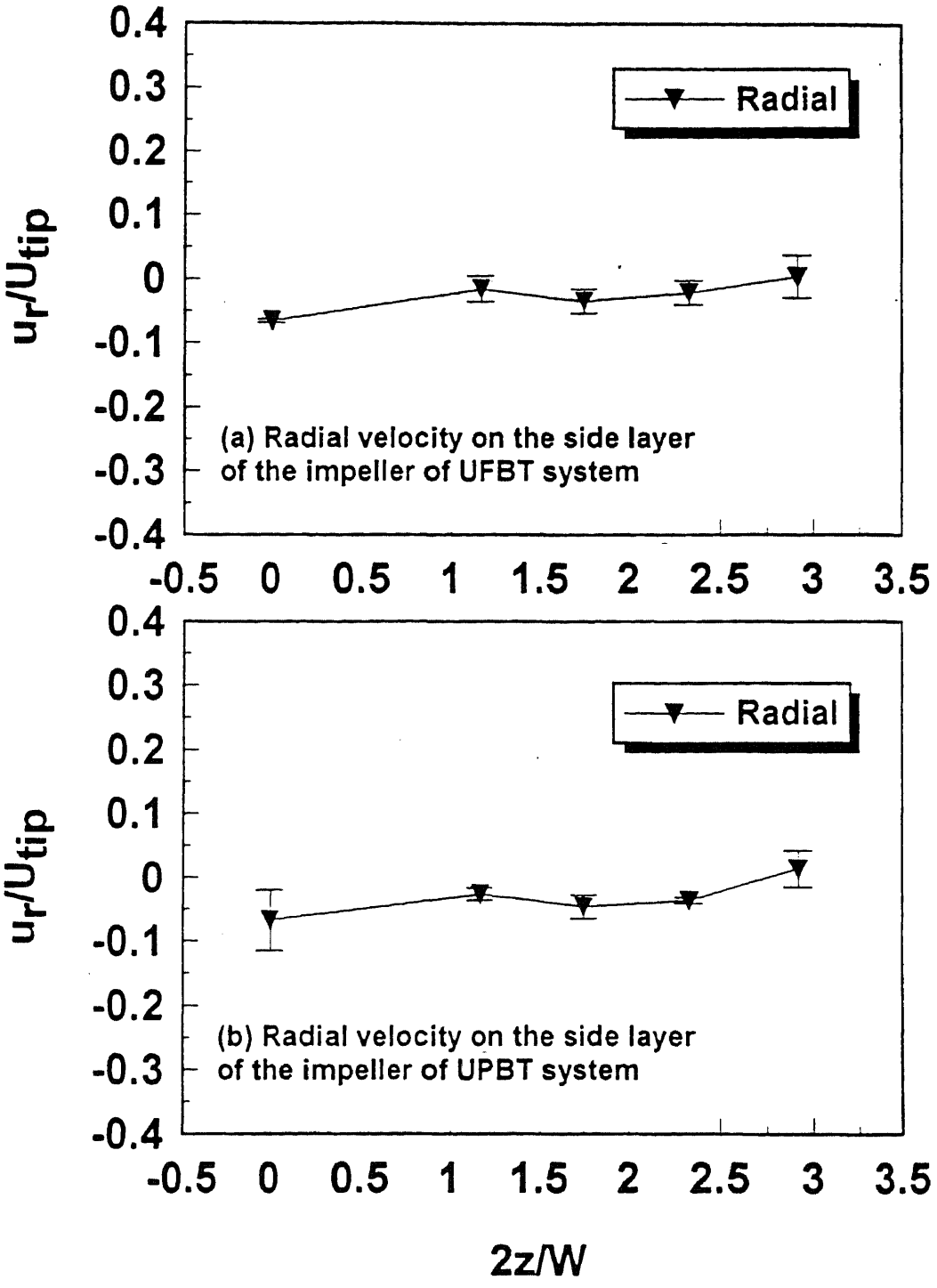

Figure 5-2. Experimentally determined (via LDV) radial velocities on the side layer of the impeller region. (a) UFBT system; (b) UPBT system. Negative value indicate outwards direction from impeller. Error bars indicate standard deviation of duplicate experiments.

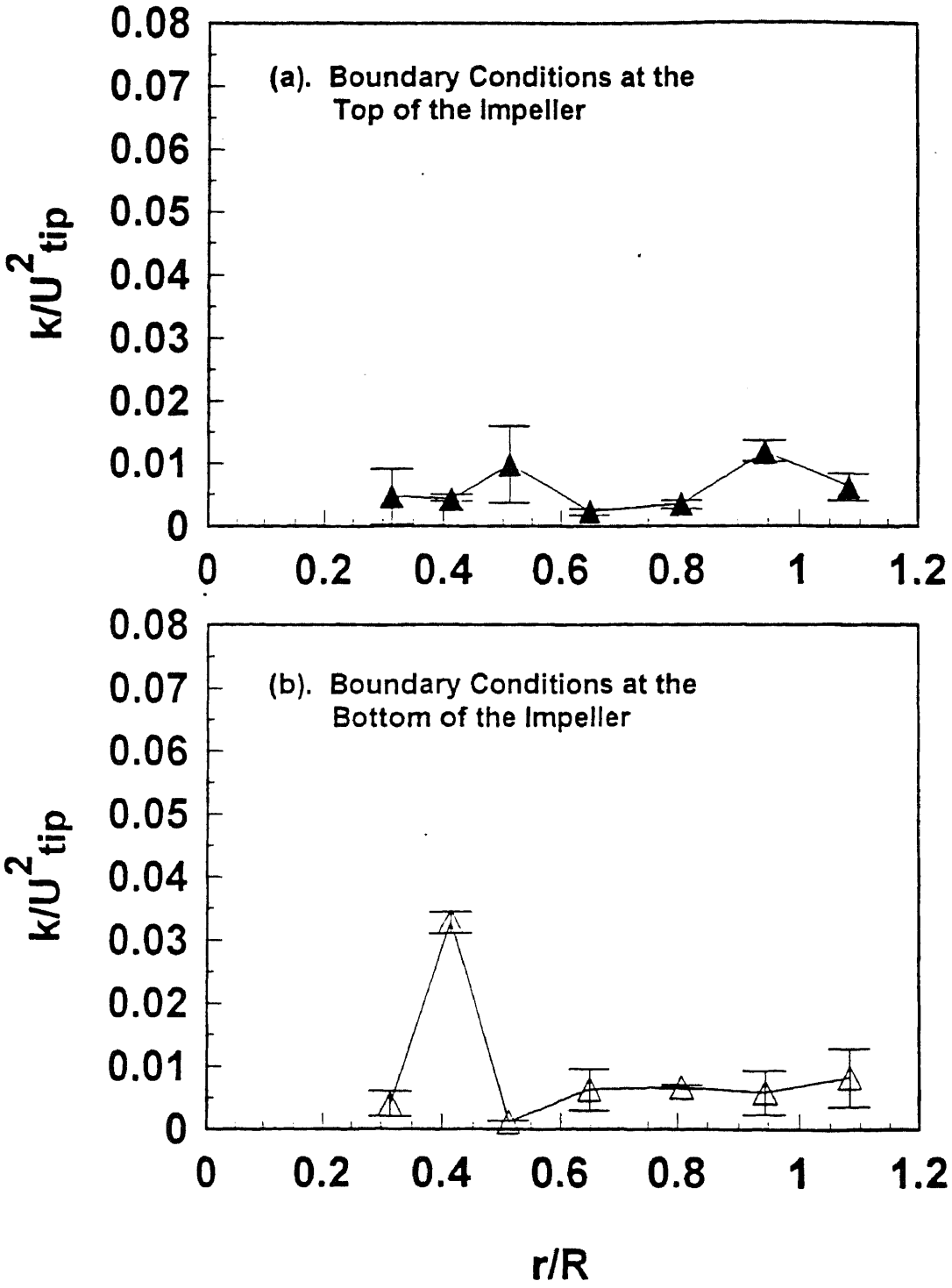

Figure 5-3. Turbulent kinetic energies in the impeller region. These values were used as the boundary conditions in the numerical CFD simulation. Unbaffled FBT system: (a) boundary conditions at the top of the impeller; (b) boundary conditions at the bottom of the impeller. Error bars indicate standard deviation of duplicate experiments.

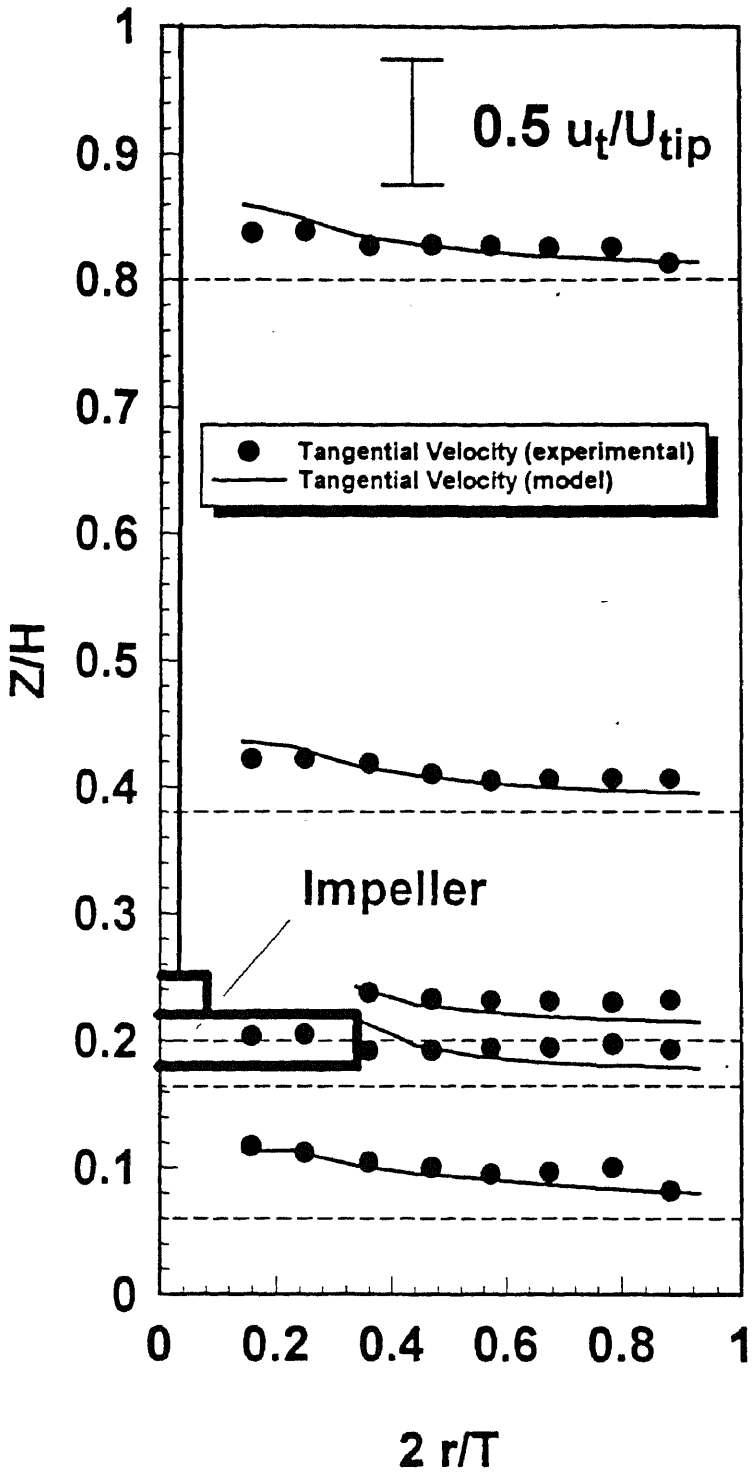

Figure 5-4. Comparison between experimental LDV tangential velocity data (u_t) and corresponding values from CFD simulation using ASM and B.C. #2 for Z/H equal to 0.0656, 0.164, 0.2, 0.38, and 0.8.

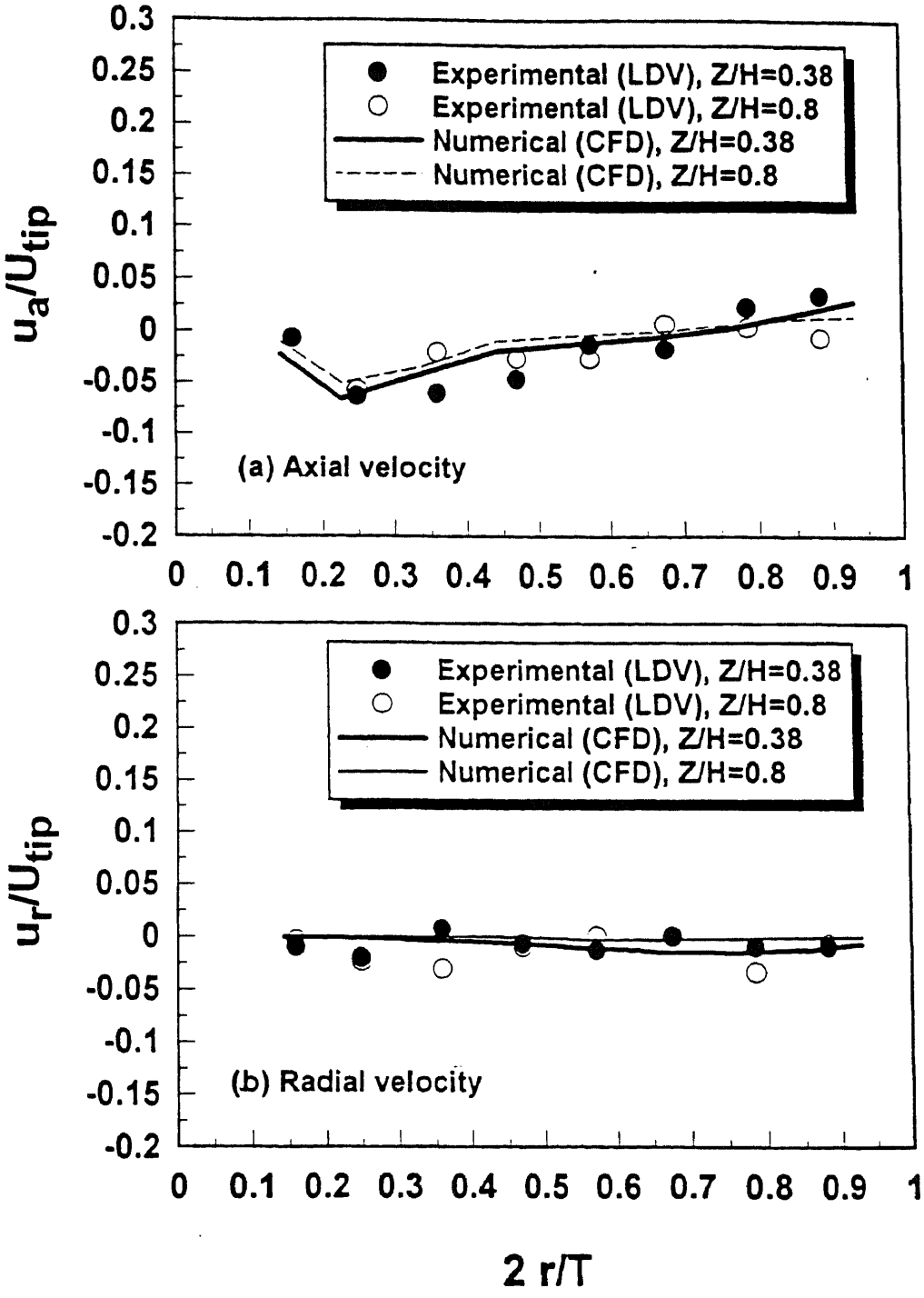

Figure 5-5. Comparison between experimental LDV data and the results of numerical CFD simulation for (a) axial velocity, (b) radial velocity component using ASM and B. C . #2 in the unbaffled FBT system. Positive values indicate upwards (for axial velocities) and incoming (for radial towards impeller) velocities.

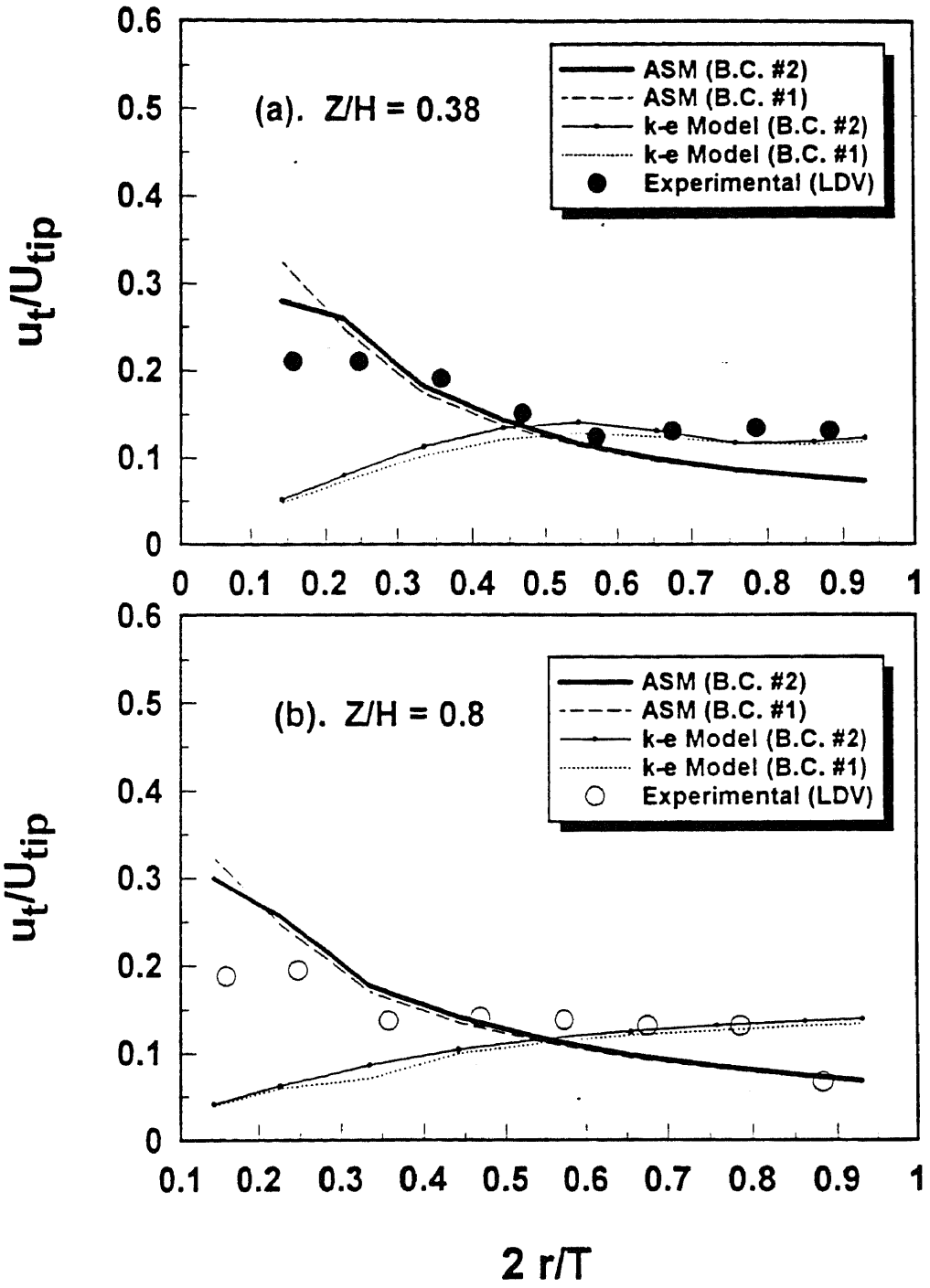

Figure 5-6. Comparison between experimental data for tangential velocity and numerical predictions obtained using different turbulence models (ASM or k-e) and different boundary conditions in the impeller region (B.C. #1 or #2) for unbaffled FBT system. (a) Comparison for Z/H = 0.38; (b) Comparison for Z/H = 0.8.

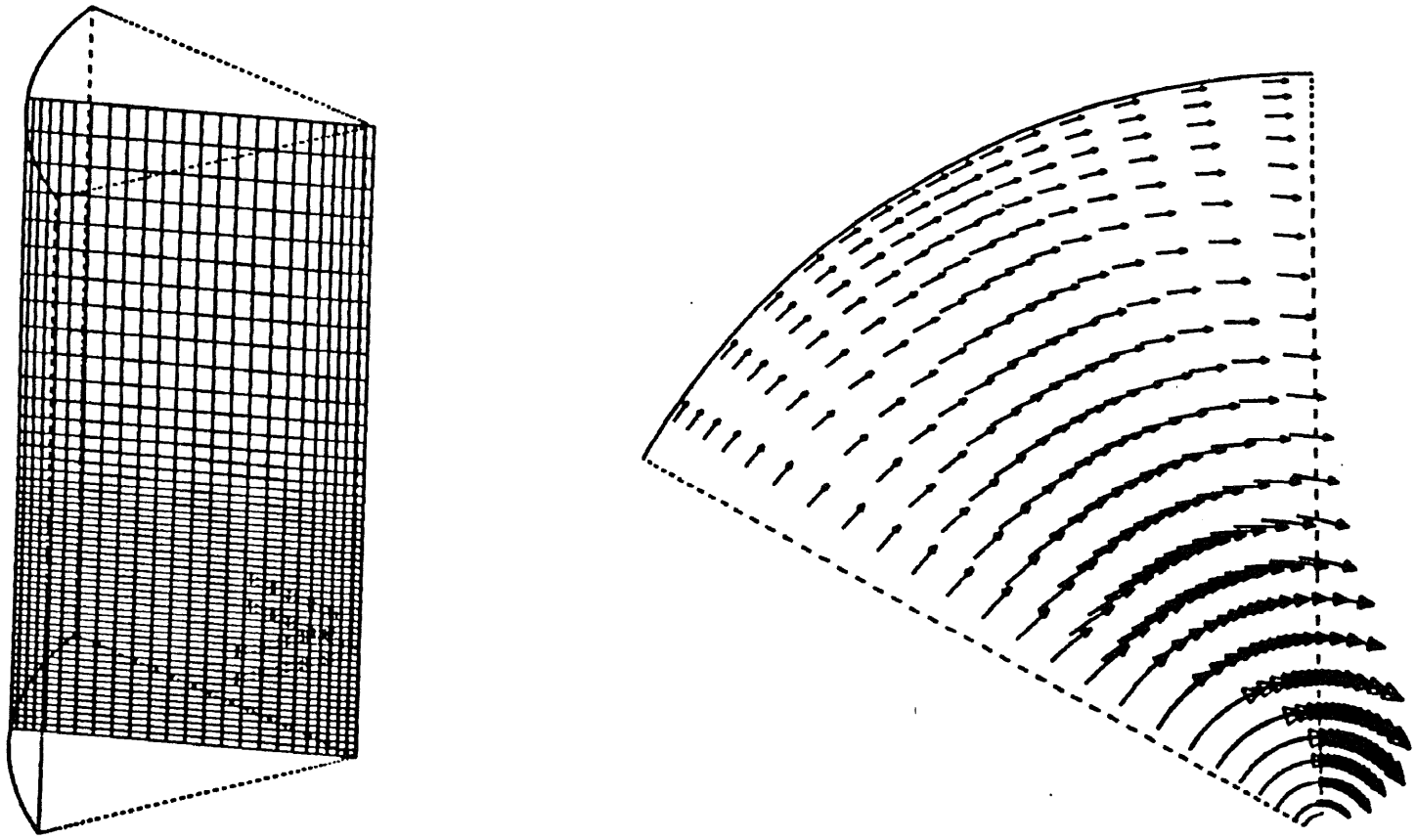

(a). (b).

Figure 5-7. Simulation for the unbaffled FBT system. (a) the computational grids; (b) the cross sectional view of the velocity distribution.

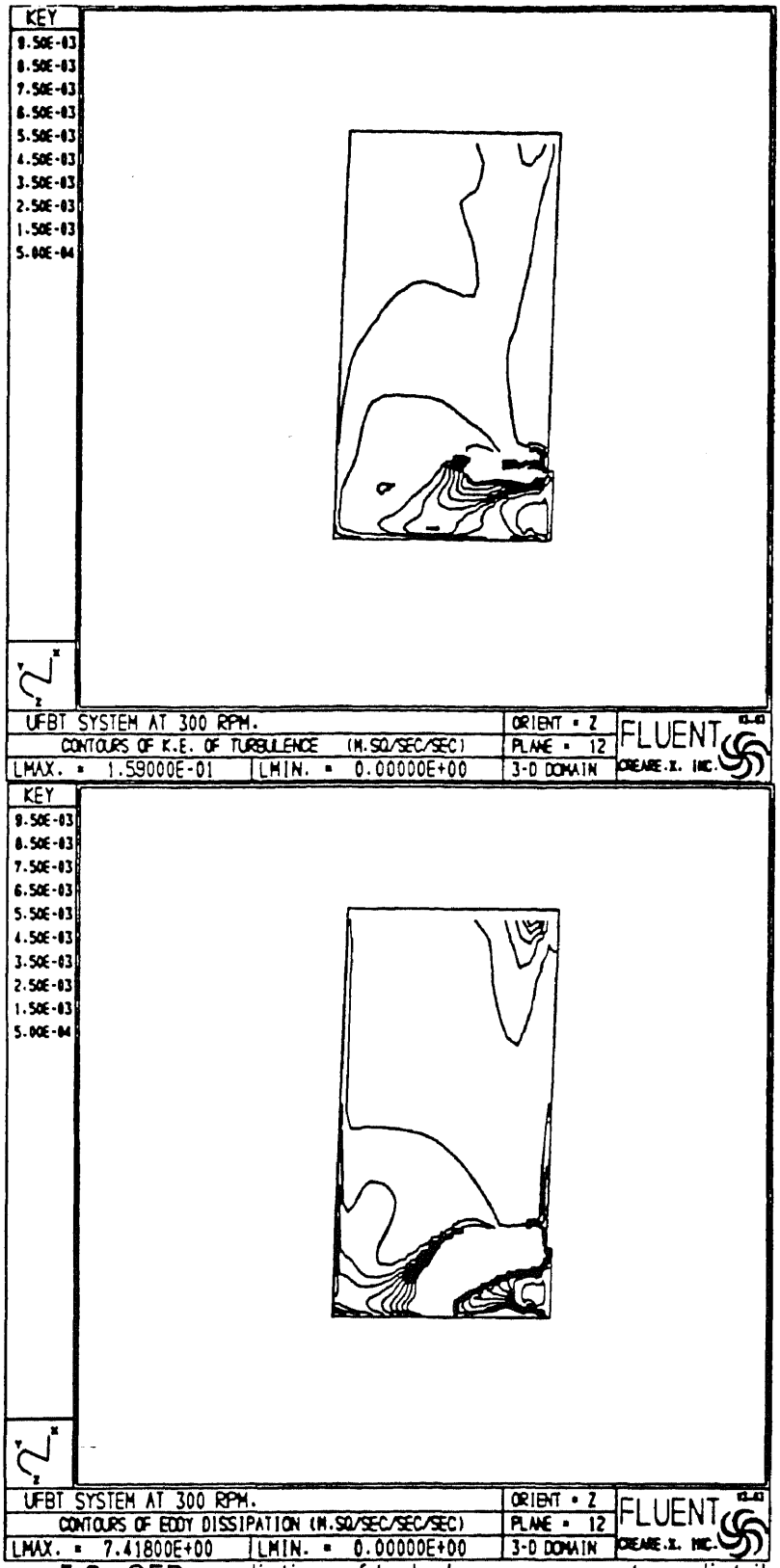

Figure 5-8. CFD prediction of turbulence parameters distribution in the vessel. System: unbaffled FBT. Contours for (a) turbulence kinetic energy; (b) dissipation rate.

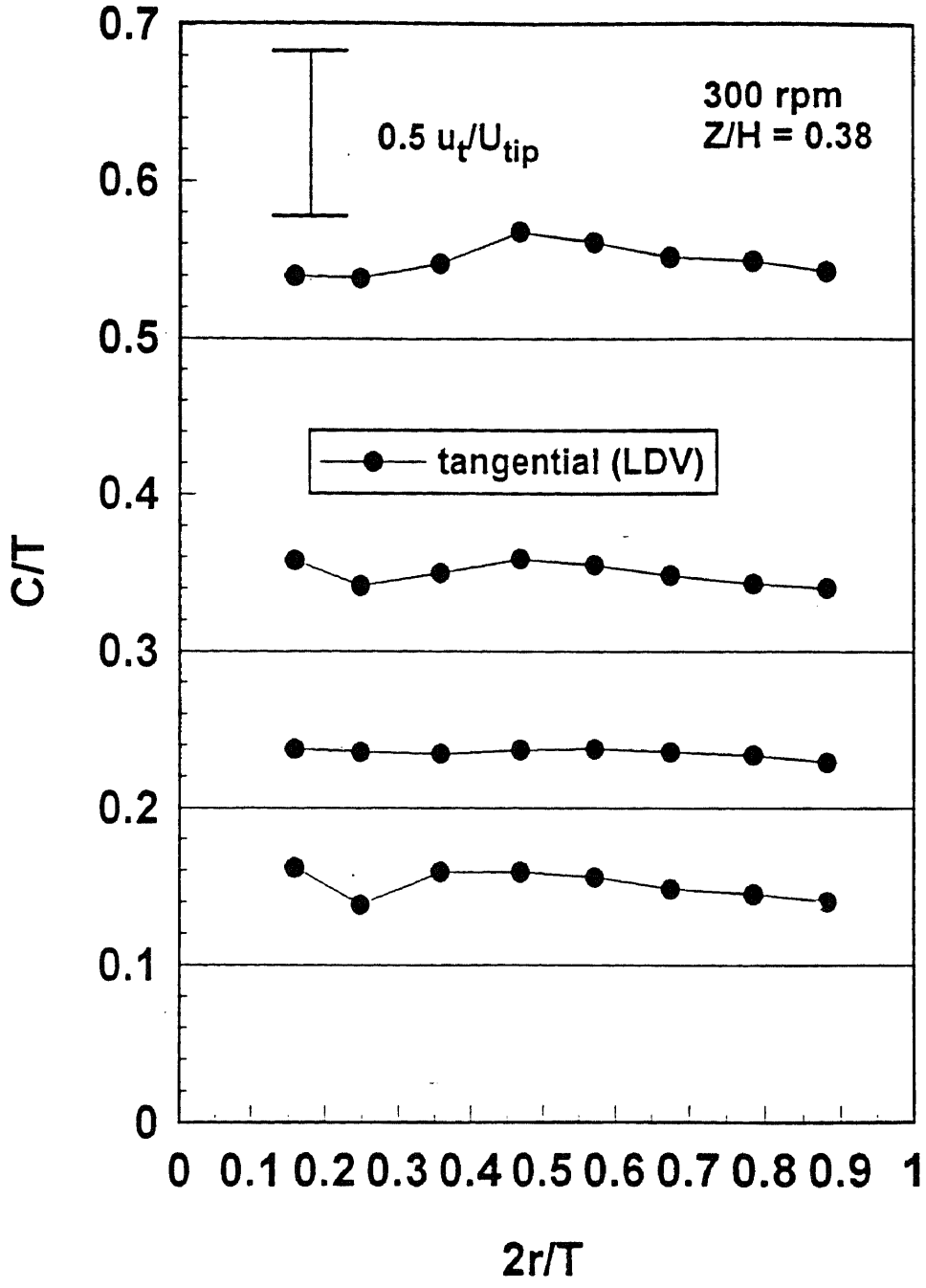

Figure 5-9. Experimentally determined (via LDV) tangential velocities at (C/T) equal to 0.1, 0.2, 0.3, and 0.5 for UFBT system.

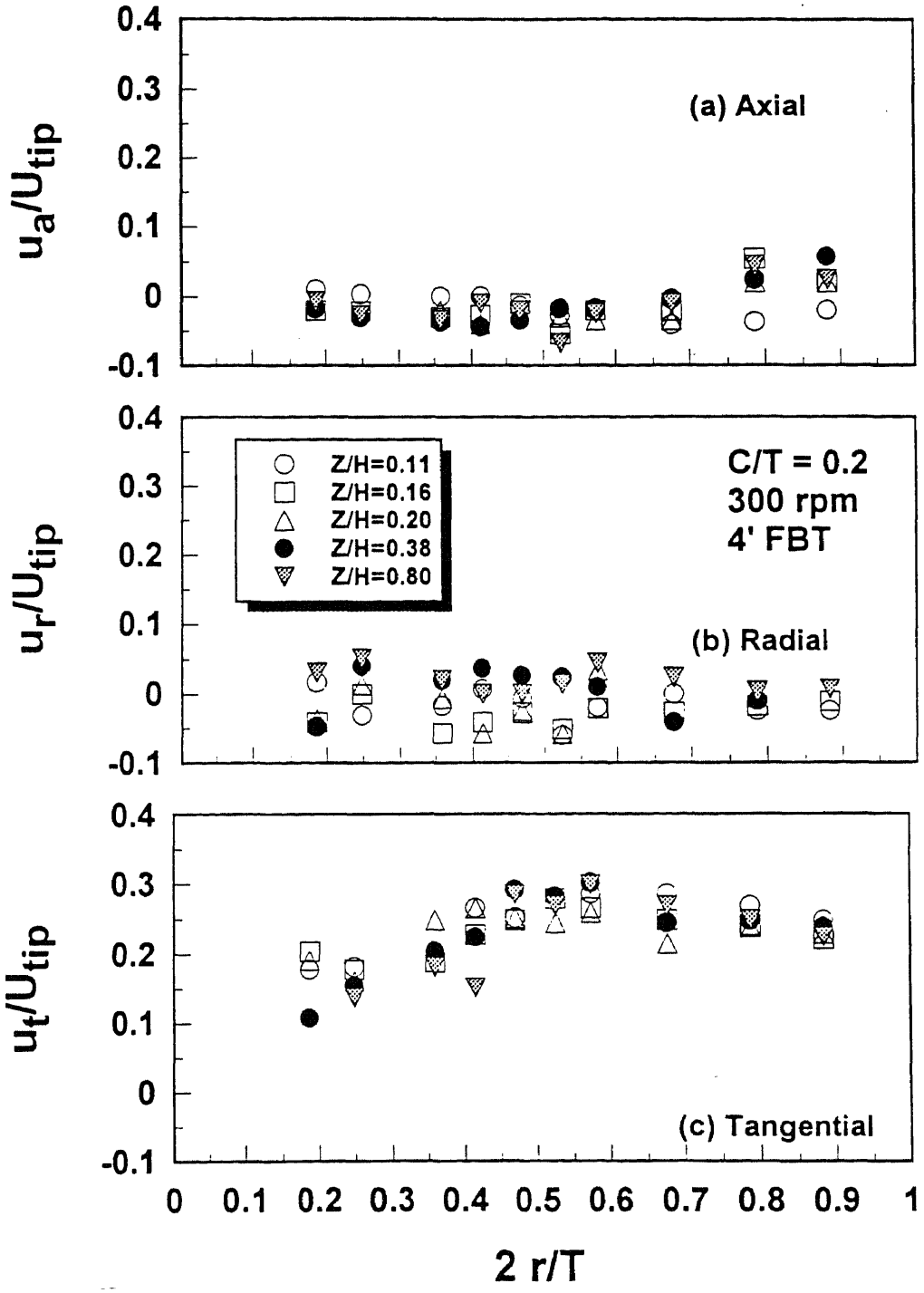

Figure 5-10. LDV measurements of the unbaffled flat blade turbine agitated system with formation of vortex for (a) axial, (b) radial, and (c) tangential components, at (C/T)=0.2, H=32 cm, T=29 cm, and 300 rpm.

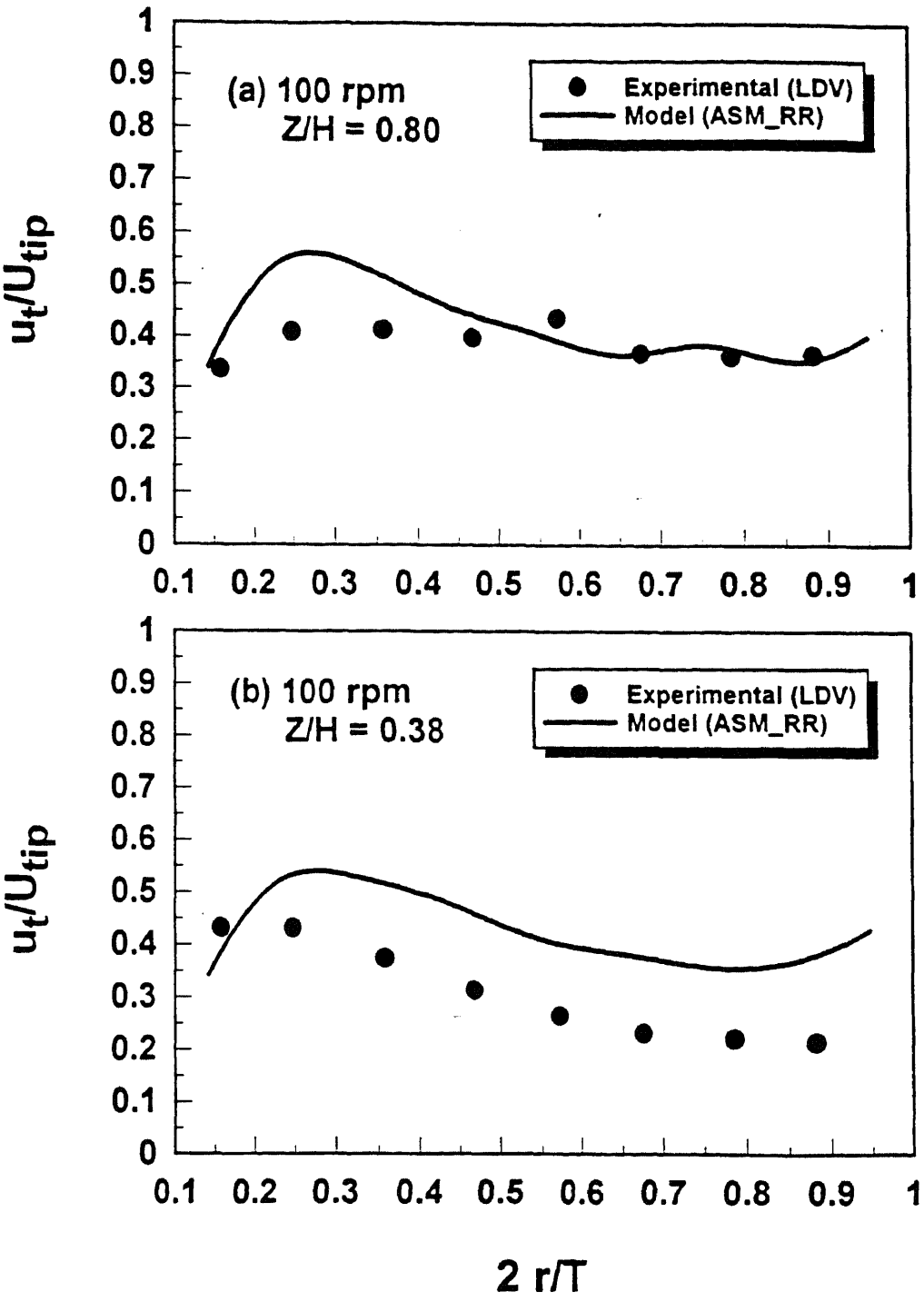

Figure 5-11. Comparison between the experimental data and numerical prediction for UFBT system using reference frame rotating with the vessel at 100 rpm at (a) Z/H = 0.8, and (b) Z/H = 0.38.

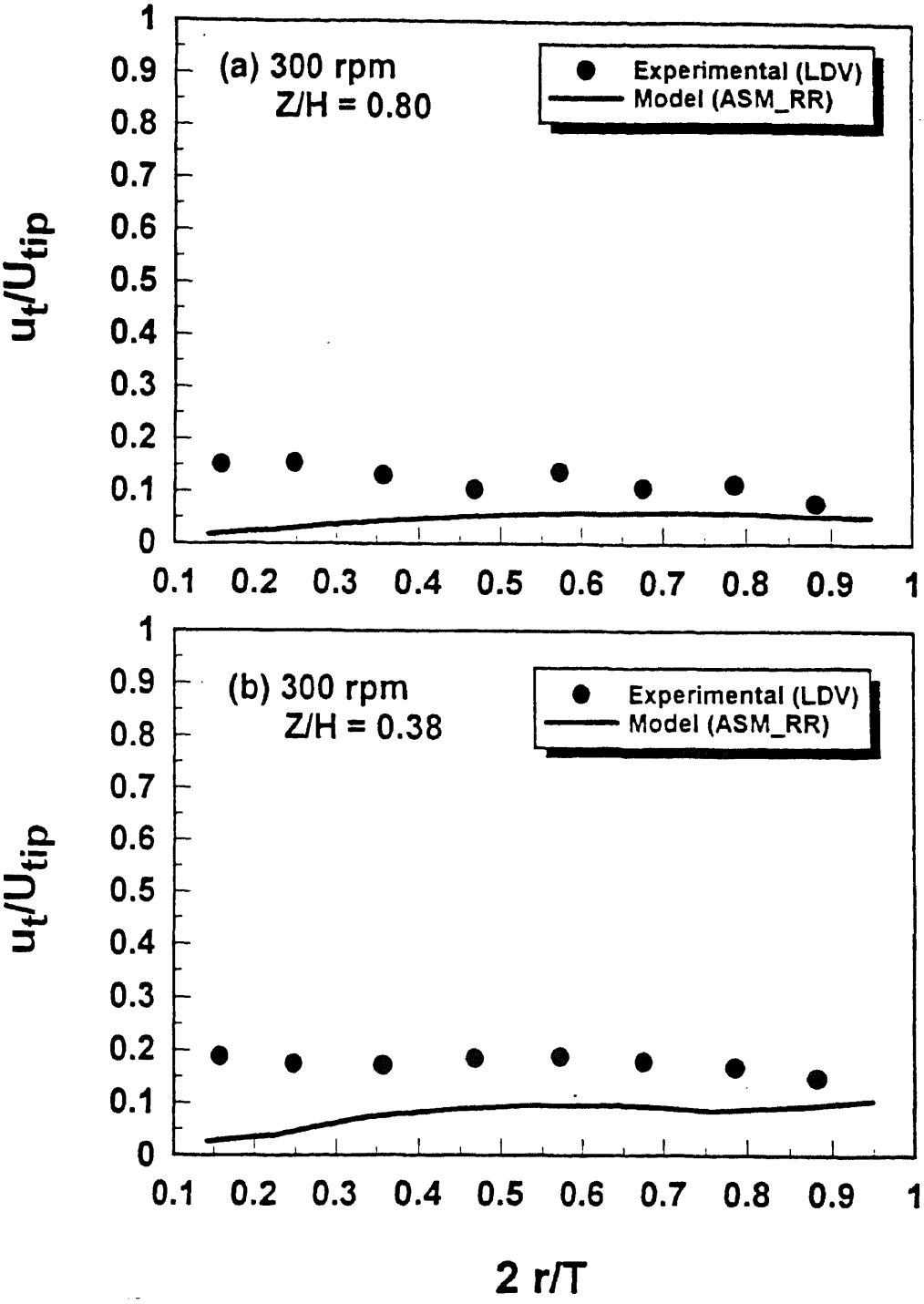

Figure 5-12. Comparison between the experimental data and numerical prediction for UFBT system using reference frame rotating with the vessel at 300 rpm at (a) Z/H = 0.8, and (b) Z/H = 0.38.

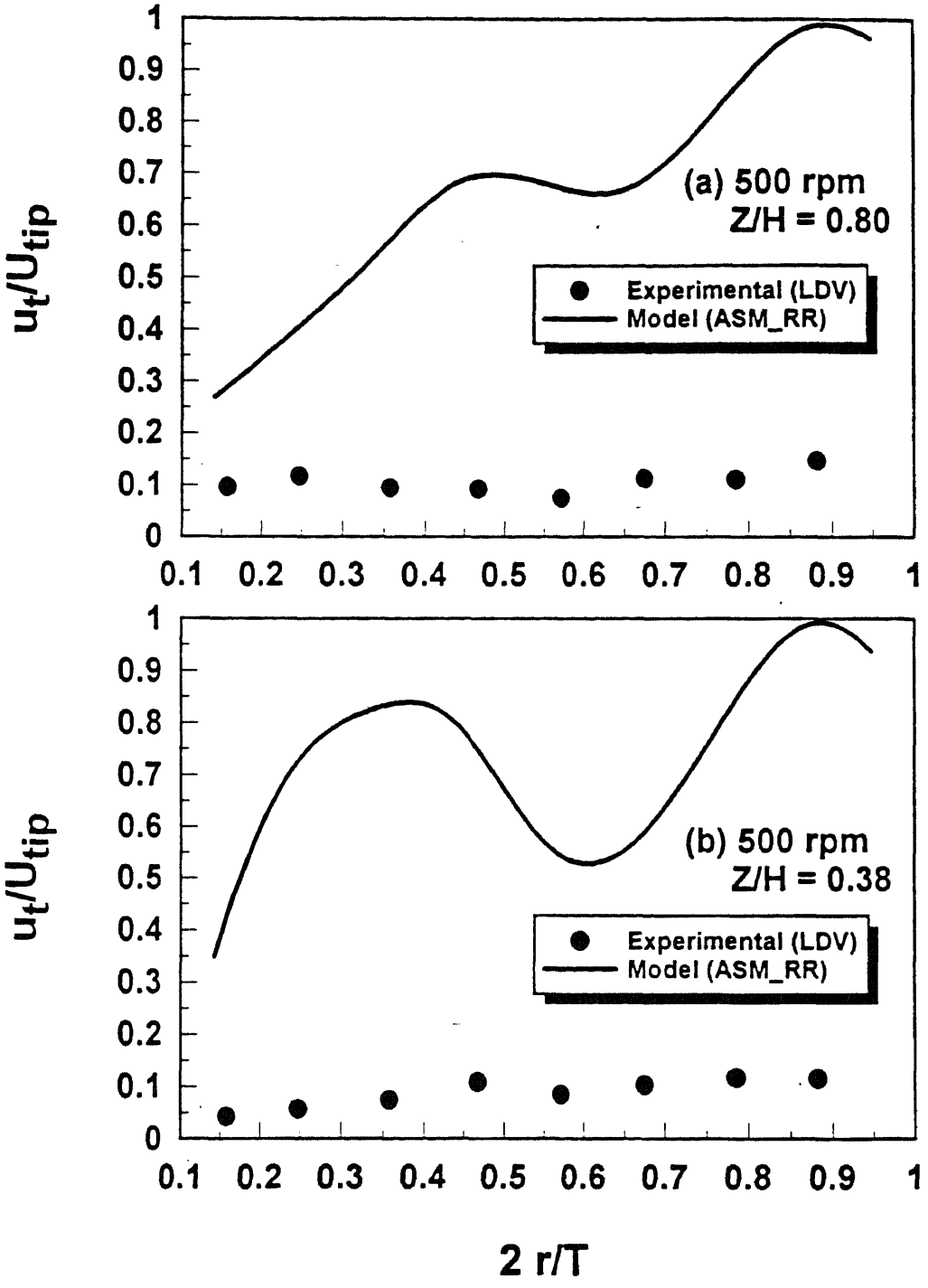

Figure 5-13. Comparison between the experimental data and numerical prediction for UFBT system using reference frame rotating with the vessel at 500 rpm at (a) Z/H = 0.8, and (b) Z/H = 0.38.

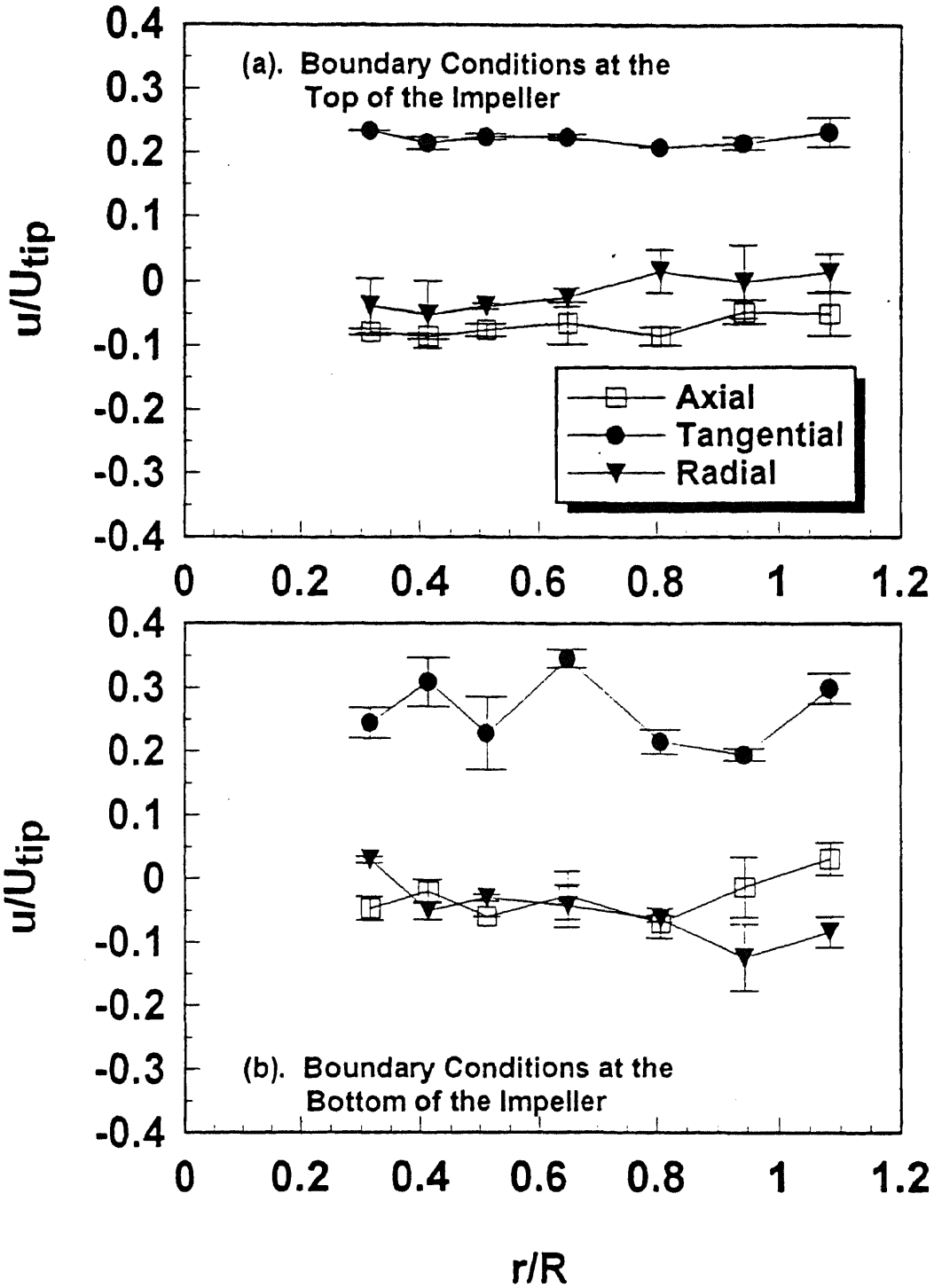

Figure 5-14. Experimentally determined (via LDV) velocities in the impeller region. These values were used as the boundary conditions in the numerical simulation. Unbaffled PBT system: (a) boundary conditions at the top of the impeller; (b) boundary conditions at the bottom of the impeller. Positive values indicate upwards velocities (for the axial direction). Error bars indicate standard deviation of duplicate experiments.

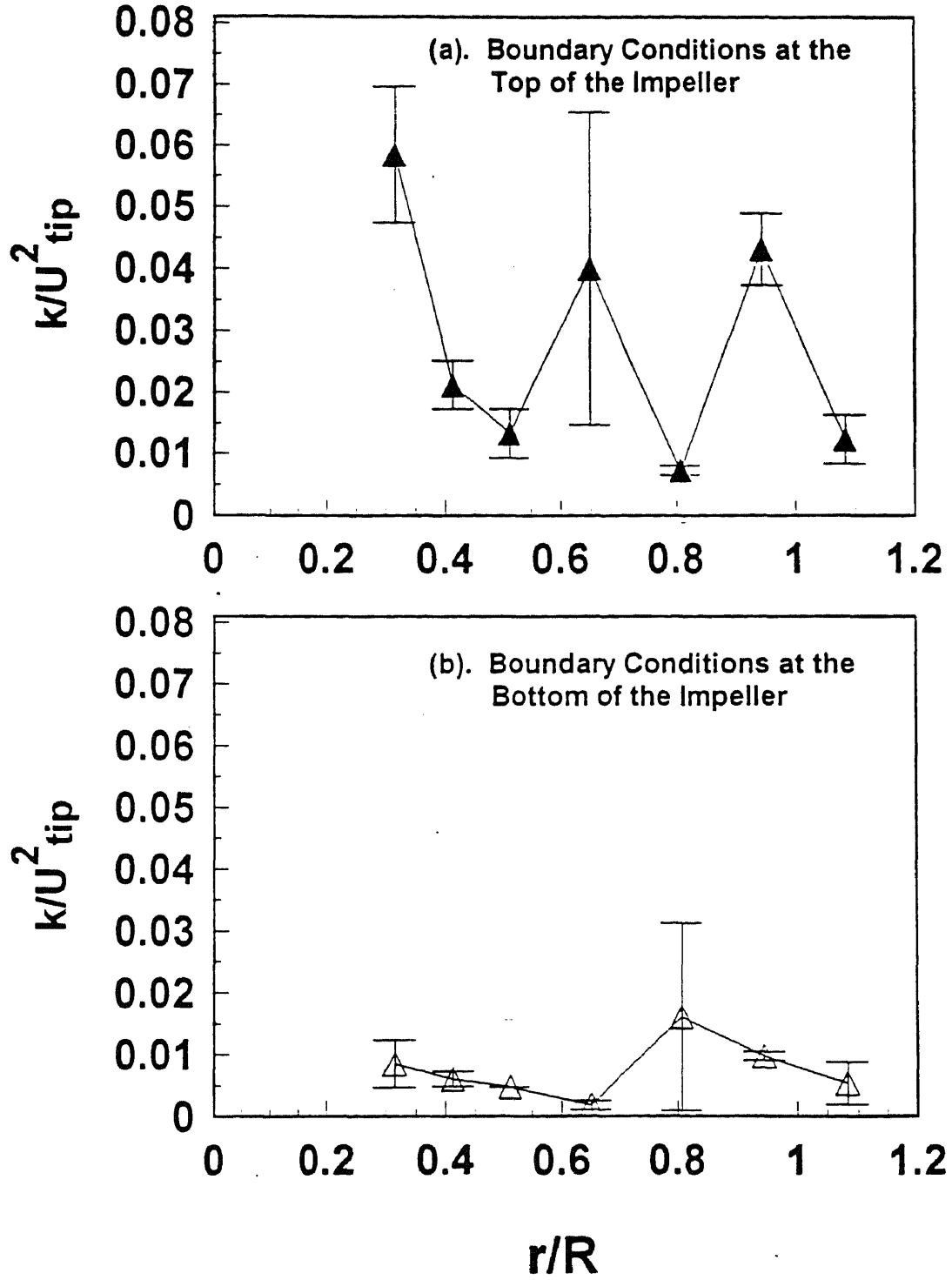

Figure 5-15. Turbulent kinetic energies in the impeller region. These values were used as the boundary conditions in the numerical CFD simulation. Unbaffled PBT system: (a) boundary conditions at the top of the impeller; (b) boundary conditions at the bottom of the impeller. Error bars indicate standard deviation of duplicate experiments.

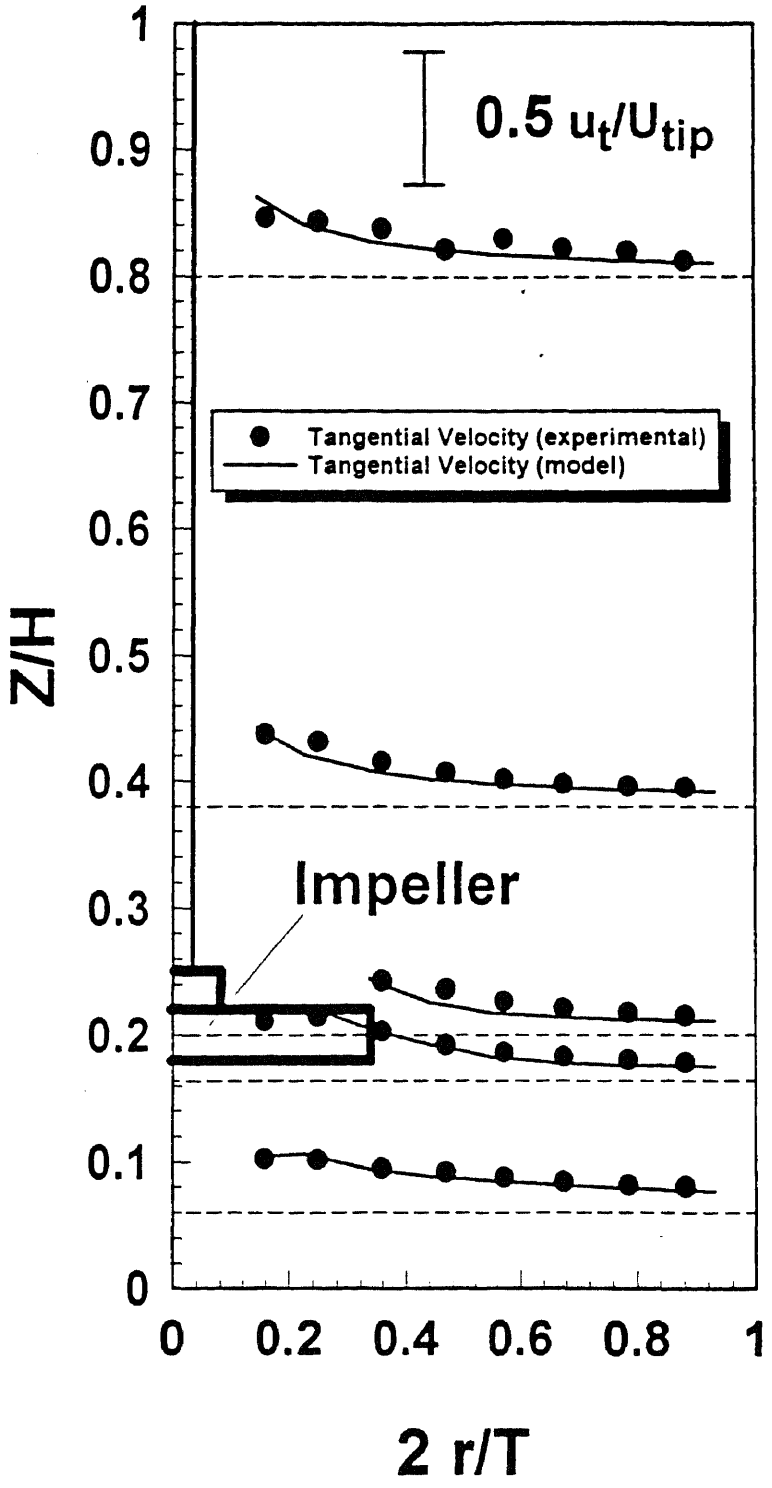

Figure 5-16. Comparison between experimental LDV tangential velocity data and corresponding values from CFD simulation using ASM and B.C. #2 for Z/H equal to 0.0656, 0.164, 0.2, 0.38, and 0.8.

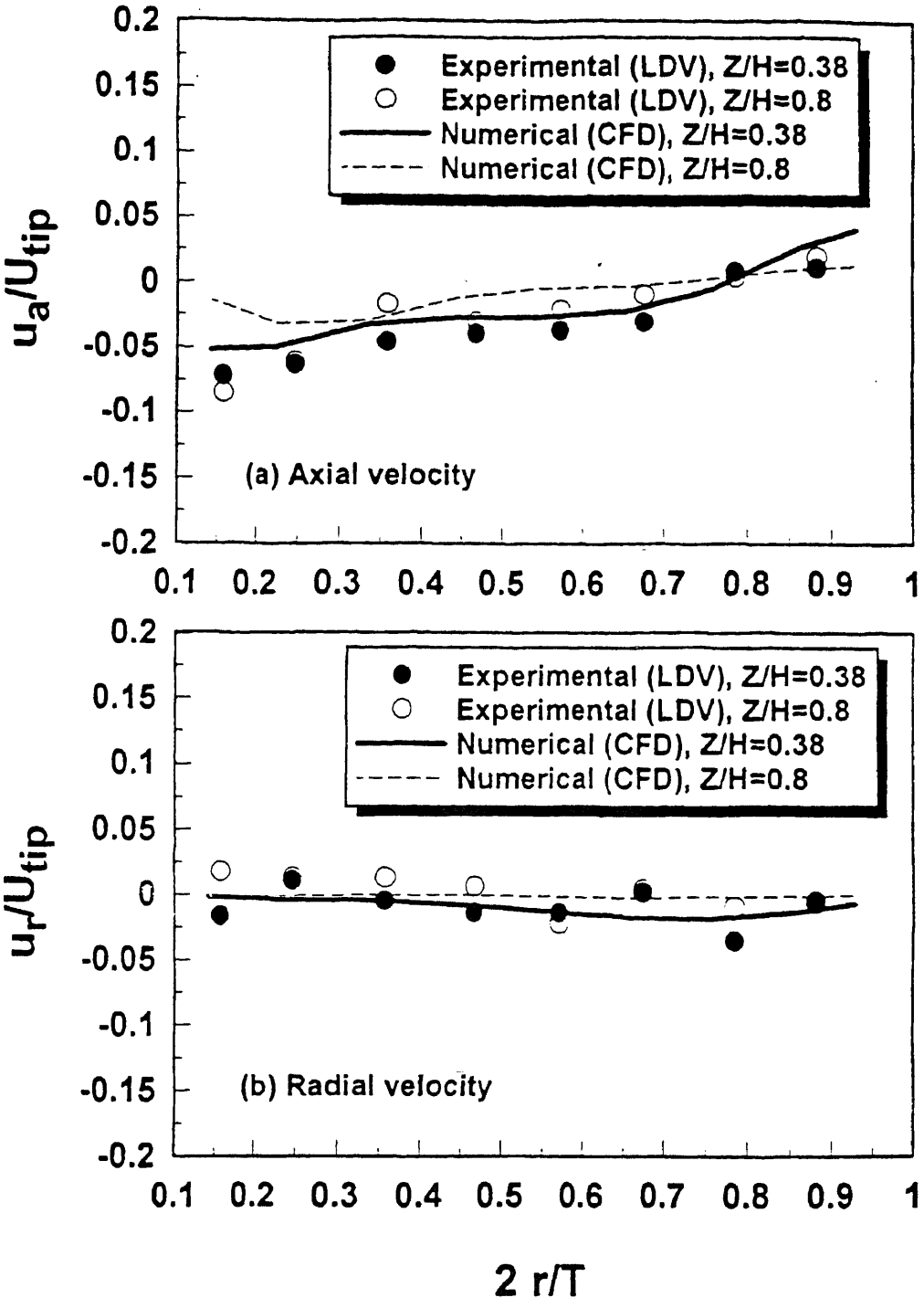

Figure 5-17. Comparison between experimental LDV data and the results of numerical CFD simulation for (a) axial velocity, (b) radial velocity component using ASM and B. C. #2. Positive values indicate upwards velocities.

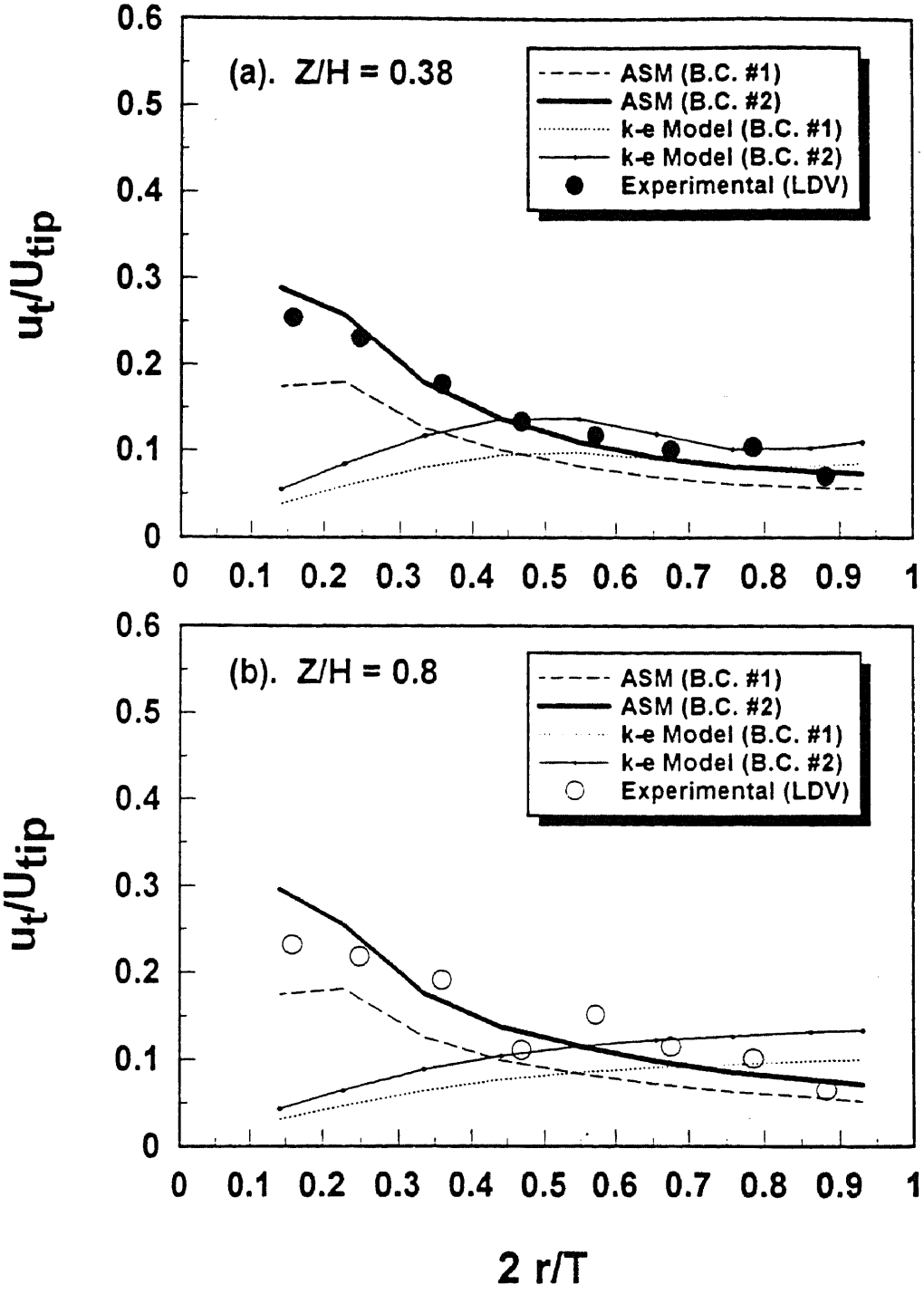

Figure 5-18. Comparison between experimental data for tangential velocity and numerical predictions obtained using different turbulence models (ASM or k-e) and different boundary conditions in the impeller region (B.C. #1, or #2) for unbaffled PBT system. (a) Comparison for Z/H = 0.38; (b) Comparison for Z/H = 0.8.

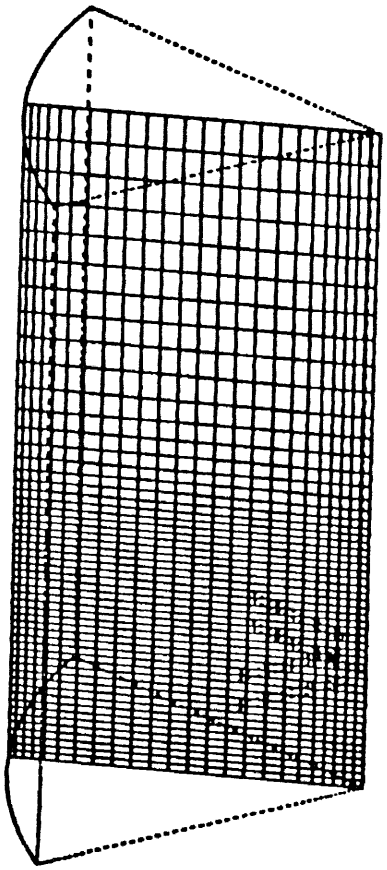

(a).

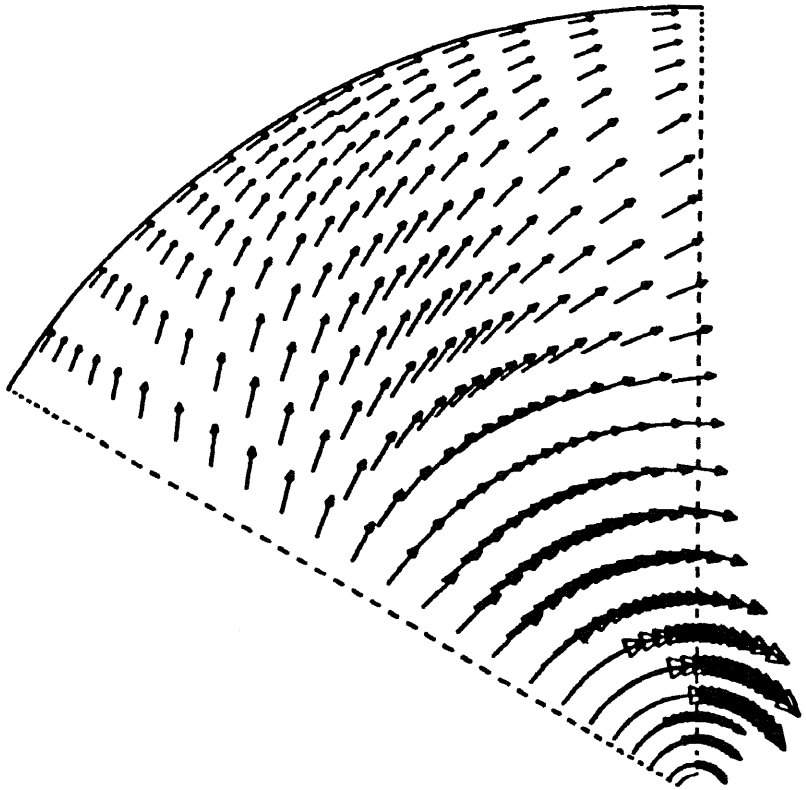

(b).

Figure 5-19. Simulation for the unbaffled PBT system. (a) the computational grids; (b) the cross sectional view of the velocity distribution.

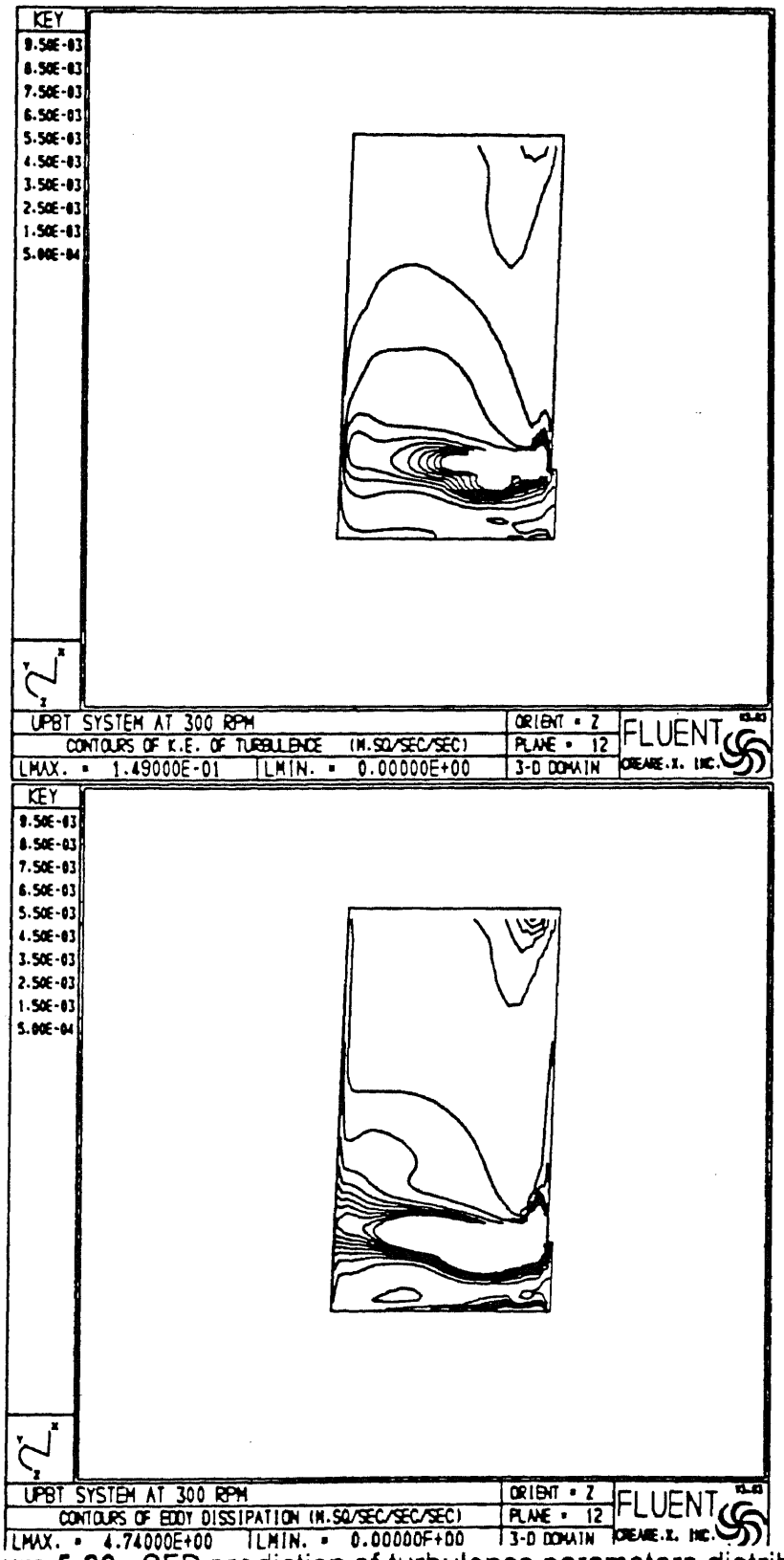

Figure 5-20. CFD prediction of turbulence parameters distribution in the vessel. System: unbaffled PBT. Contours for (a) turbulence kinetic energy; (b) dissipation rate.

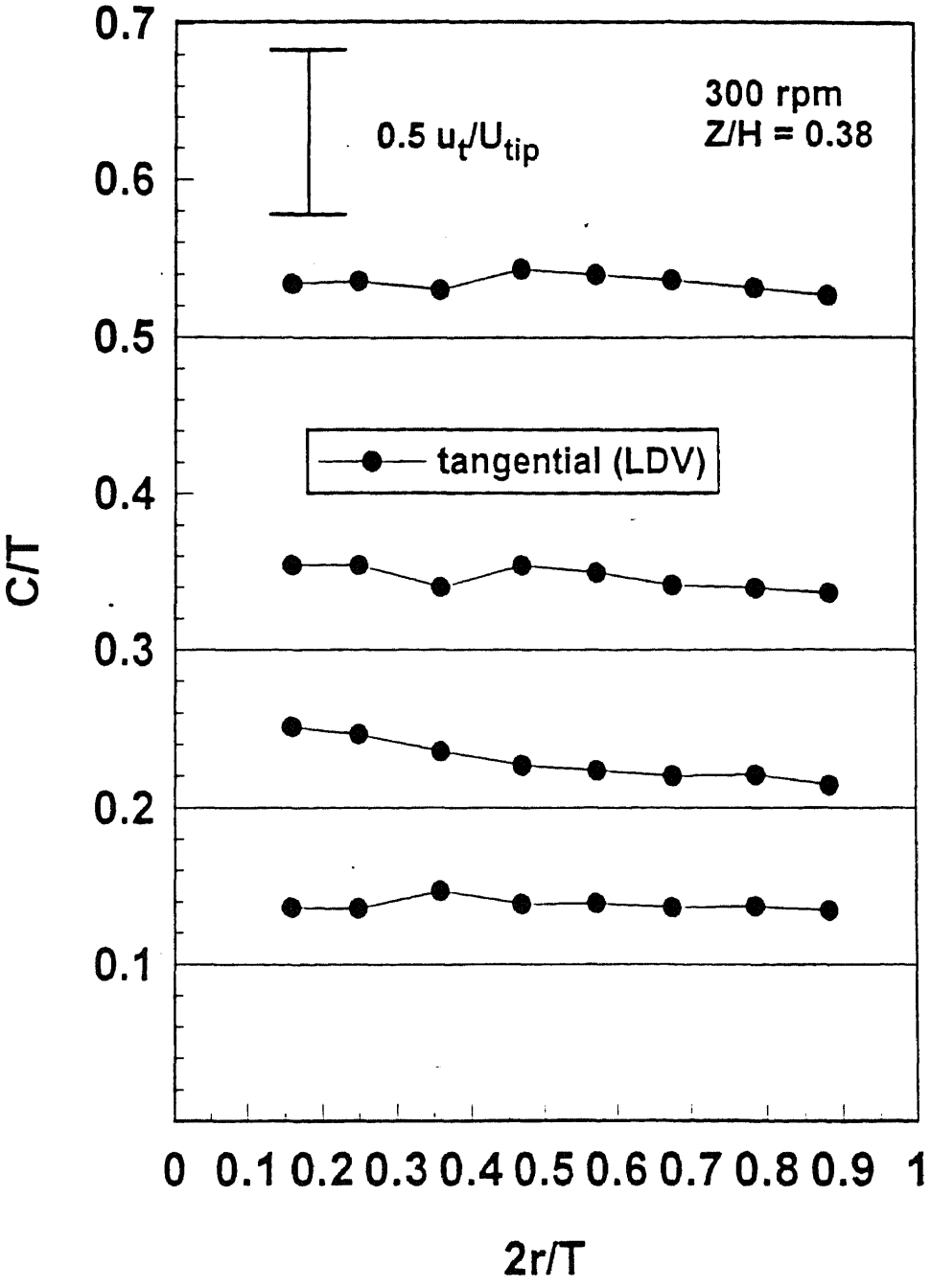

Figure 5-21. Experimentally determined (via LDV) tangential velocities at (C/T) equal to 0.1, 0.2, 0.3, and 0.5 for UPBT system.

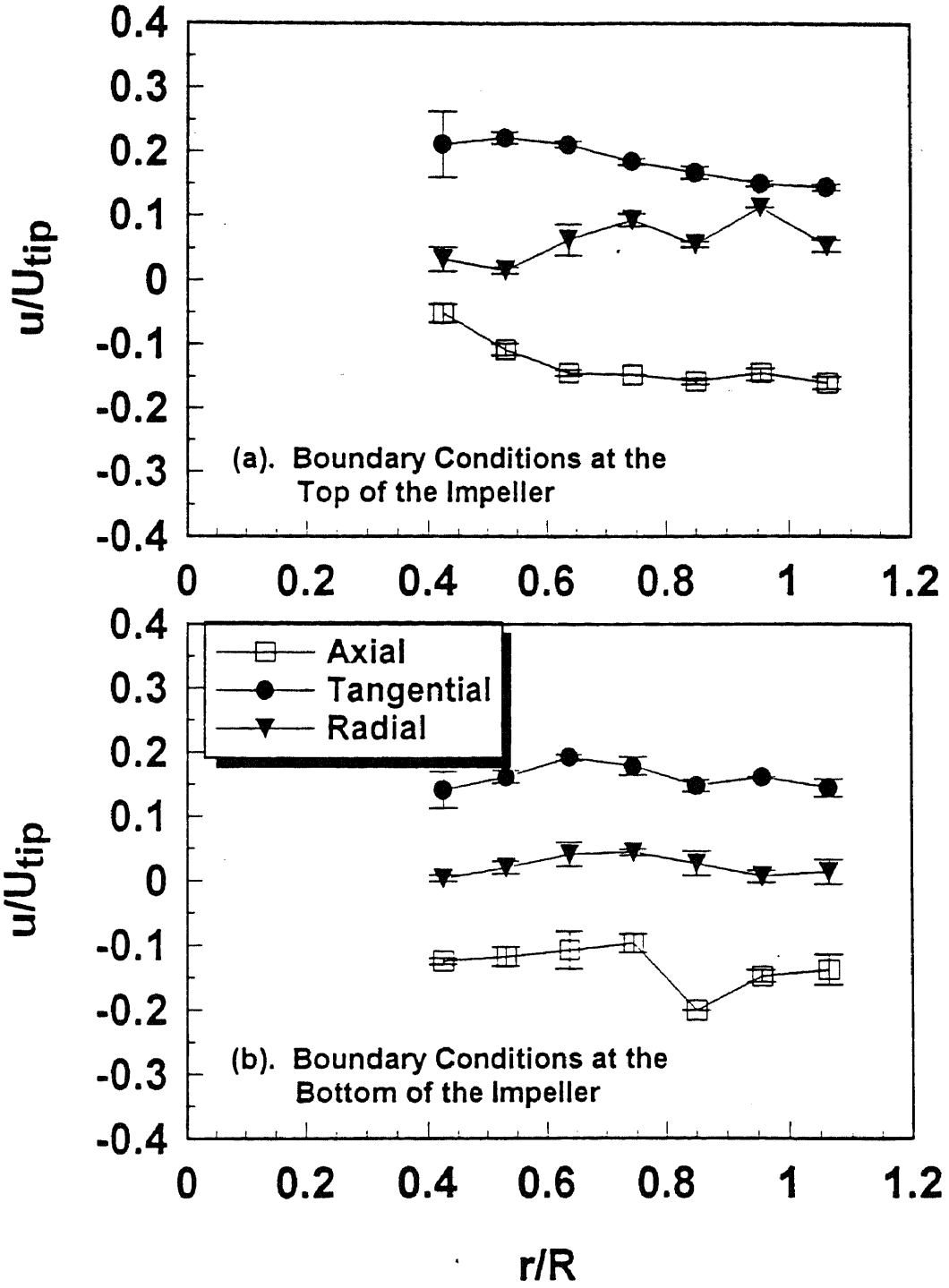

Figure 5-22. Experimentally determined (via LDV) velocities in the impeller region. These values were used as the boundary conditions in the numerical CFD simulation. Single PBT system: (a) boundary coditions at the top of the impeller; (b) boundary conditions at the bottom of the impeller. Positive values indicate upward velocities (for the axial direction). Error bars indicate standard deviation of duplicate experiments.

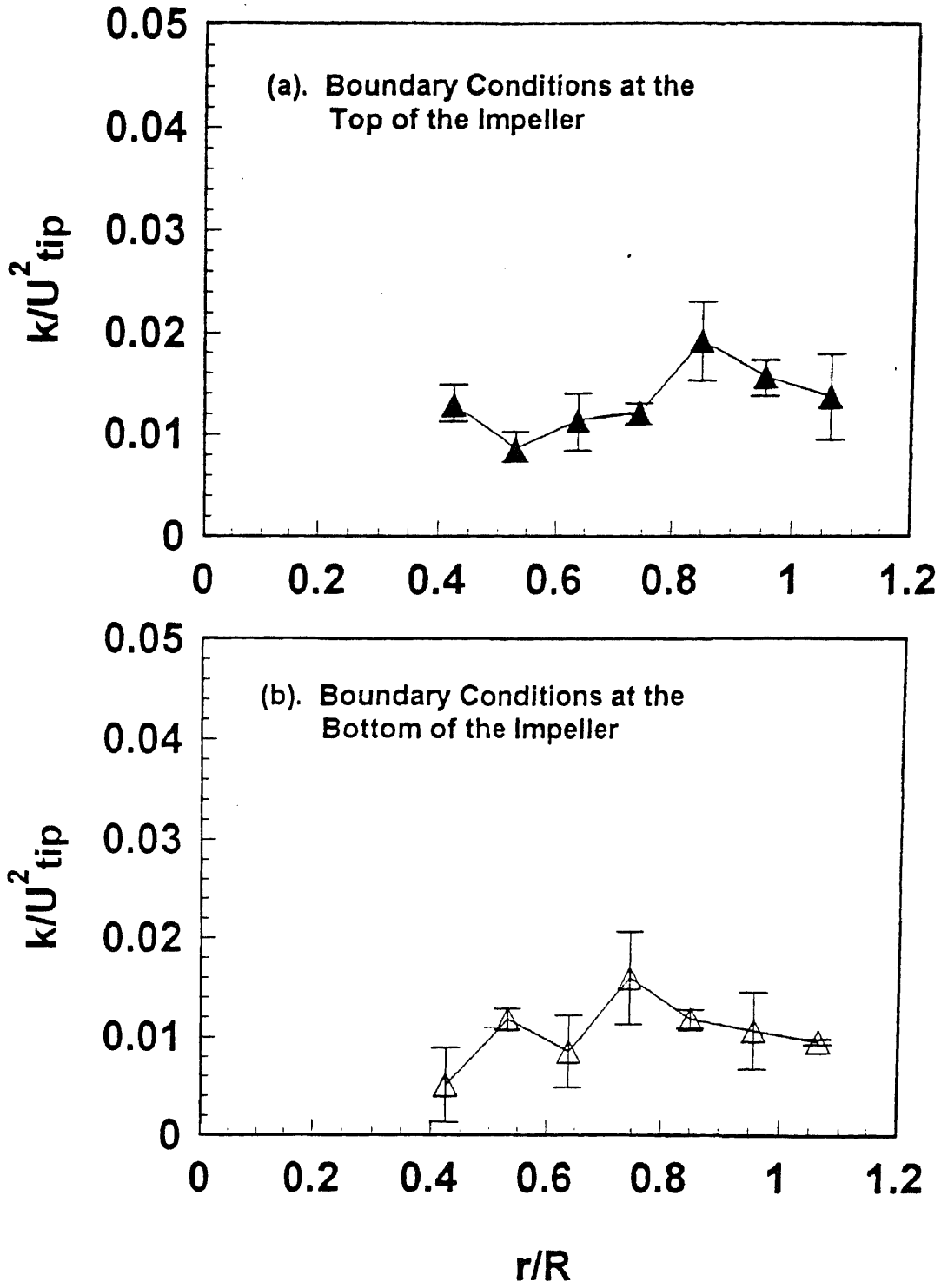

Figure 5-23. Turbulent kinetic energies in the impeller region. These values were used as the boundary conditions in the numerical CFD simulation. Single PBT system: (a) boundary conditions at the top of the impeller; (b) boundary conditions at the bottom of the impeller. Error bars indicate standard deviation of duplicate experiments.

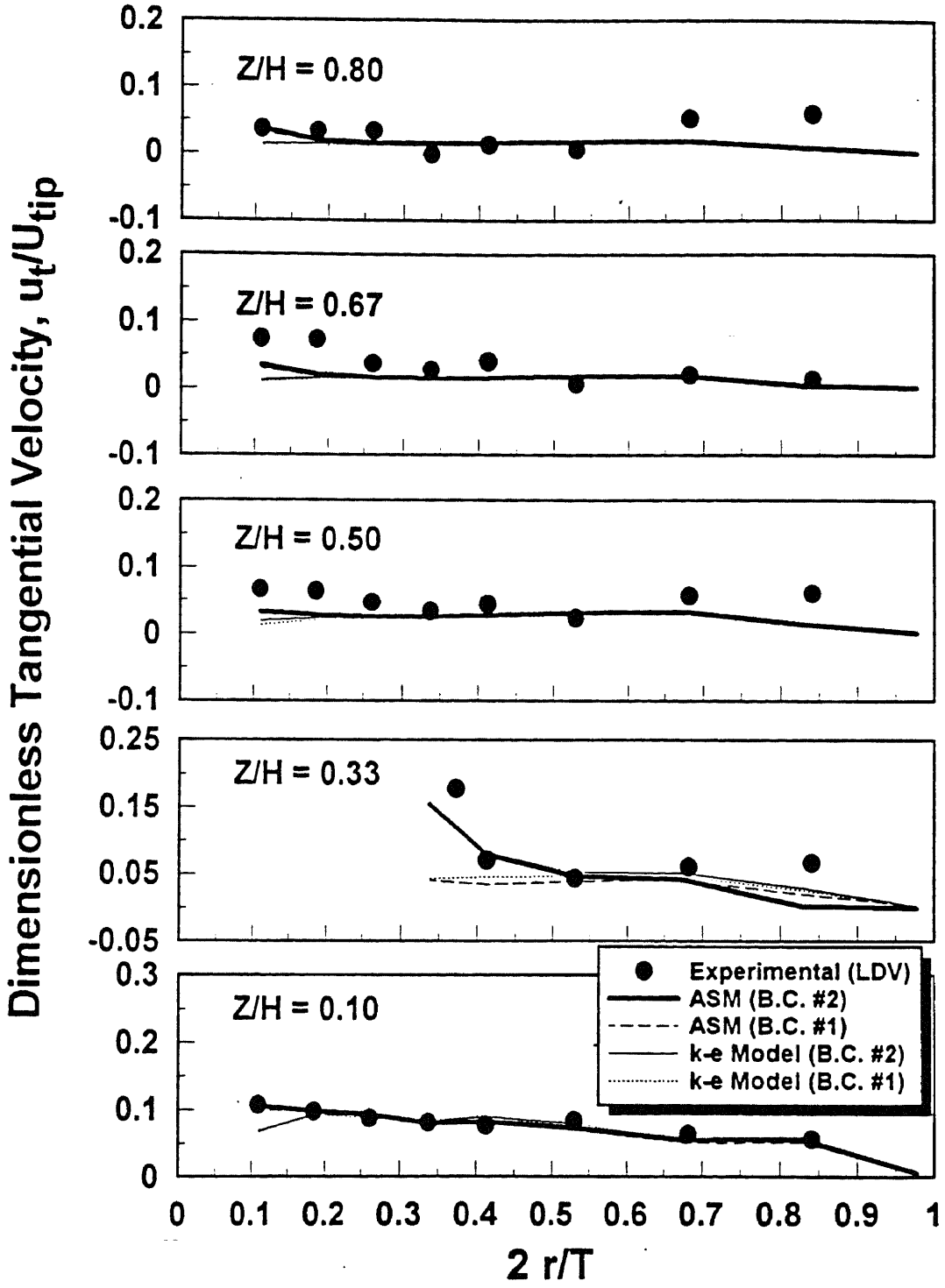

Figure 5-24. Comparison between experimental measurements and numerical predictions of the tangential velocities in single PBT system.

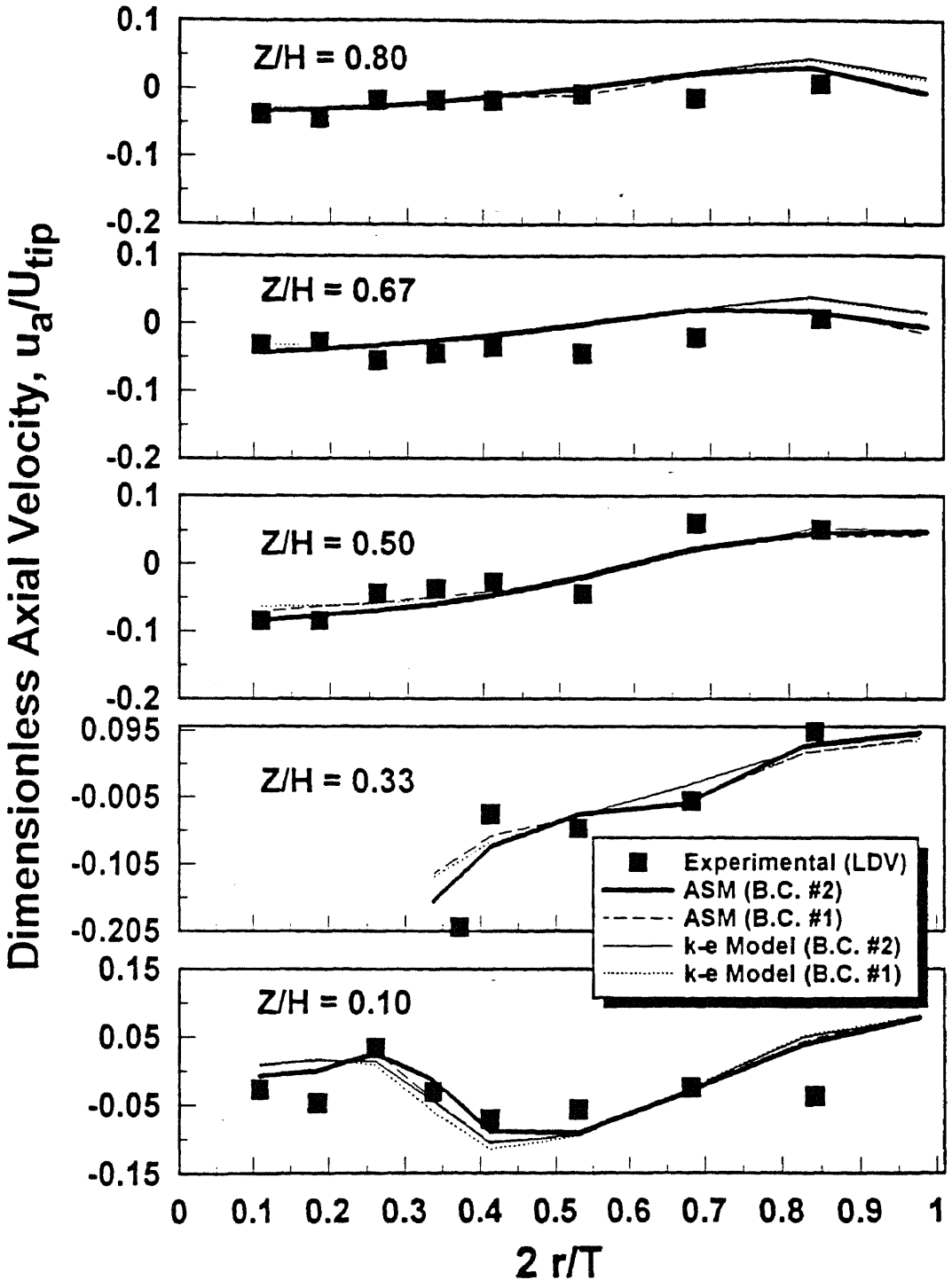

Figure 5-25. Comparison between experimental measurements and numerical predictions of the axial velocities in single PBT system.

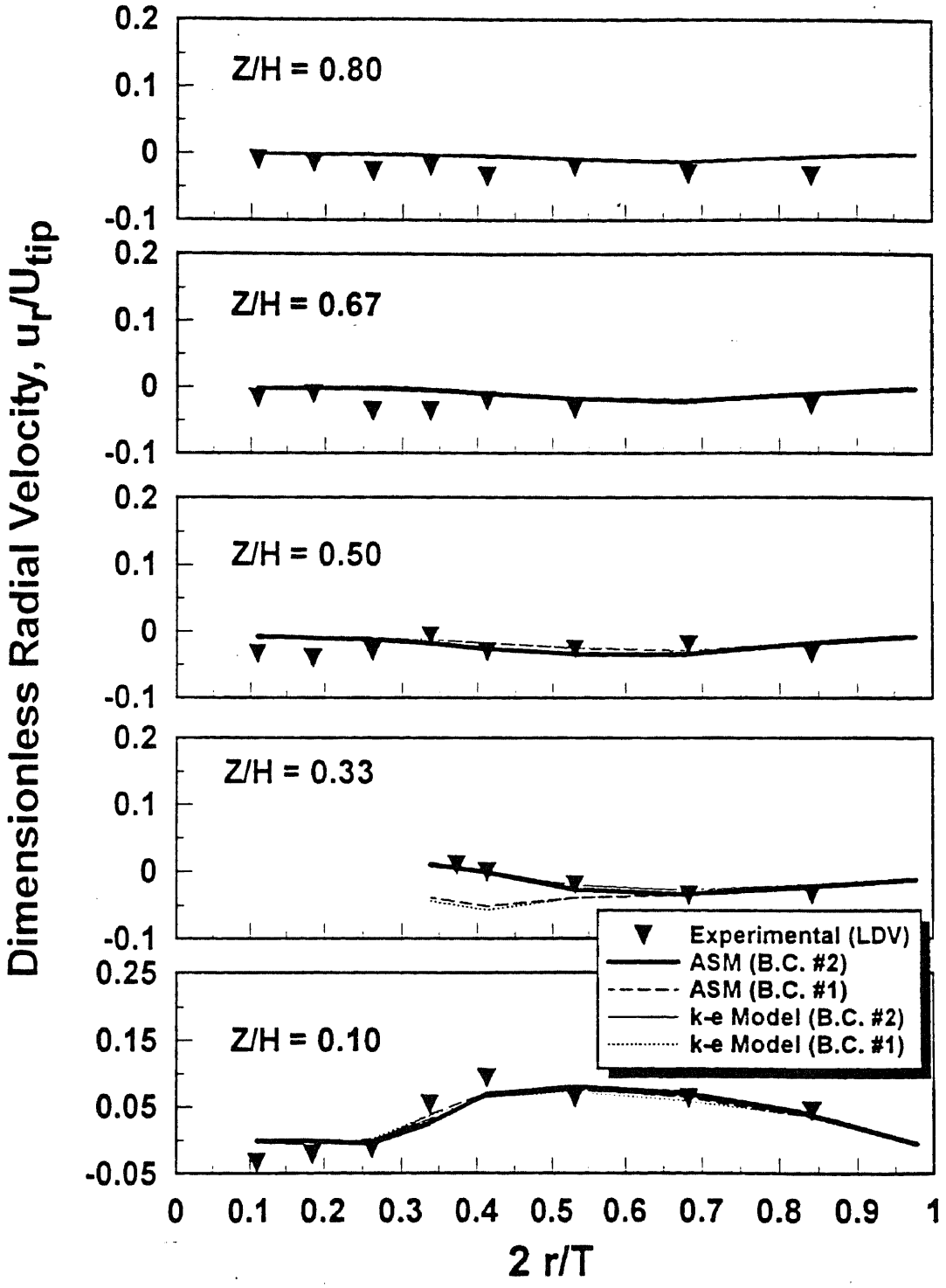

Figure 5-26. Comparison between experimental measurements and numerical predictions of the radial velocities in single PBT system.

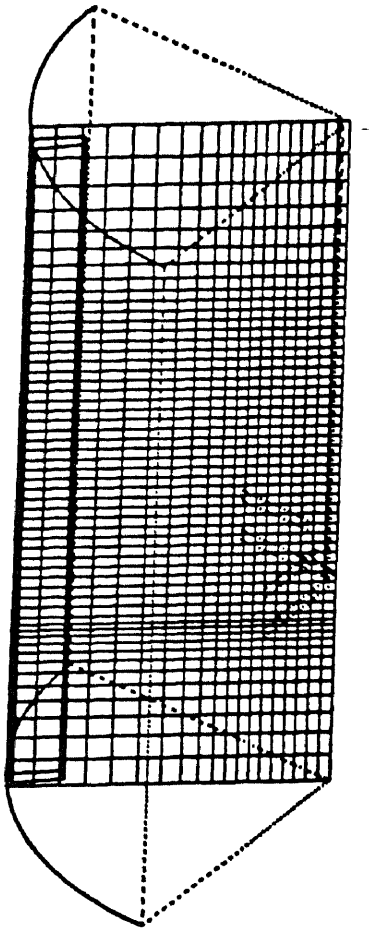

Figure 5-27. The computational grids for baffled single impeller system.

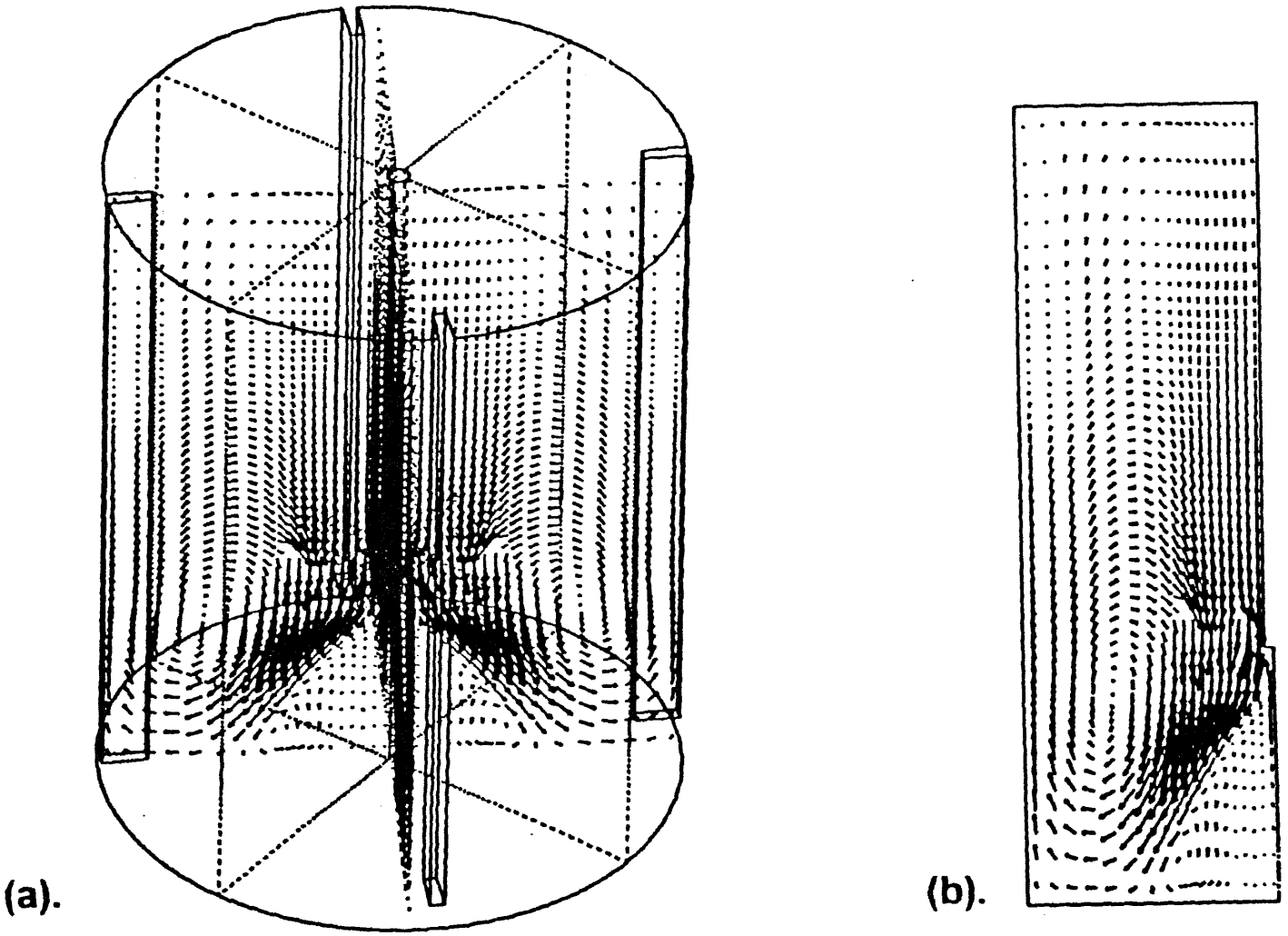

Figure 5-28. CFD prediction of velocity distribution in the vessel. System: baffled single PBT. Boundary conditions: B.C. #2. Turbulence model: ASM. (a) Tridimensional view; (b) Bidimensional cross section across the impeller shaft (only one half section shown).

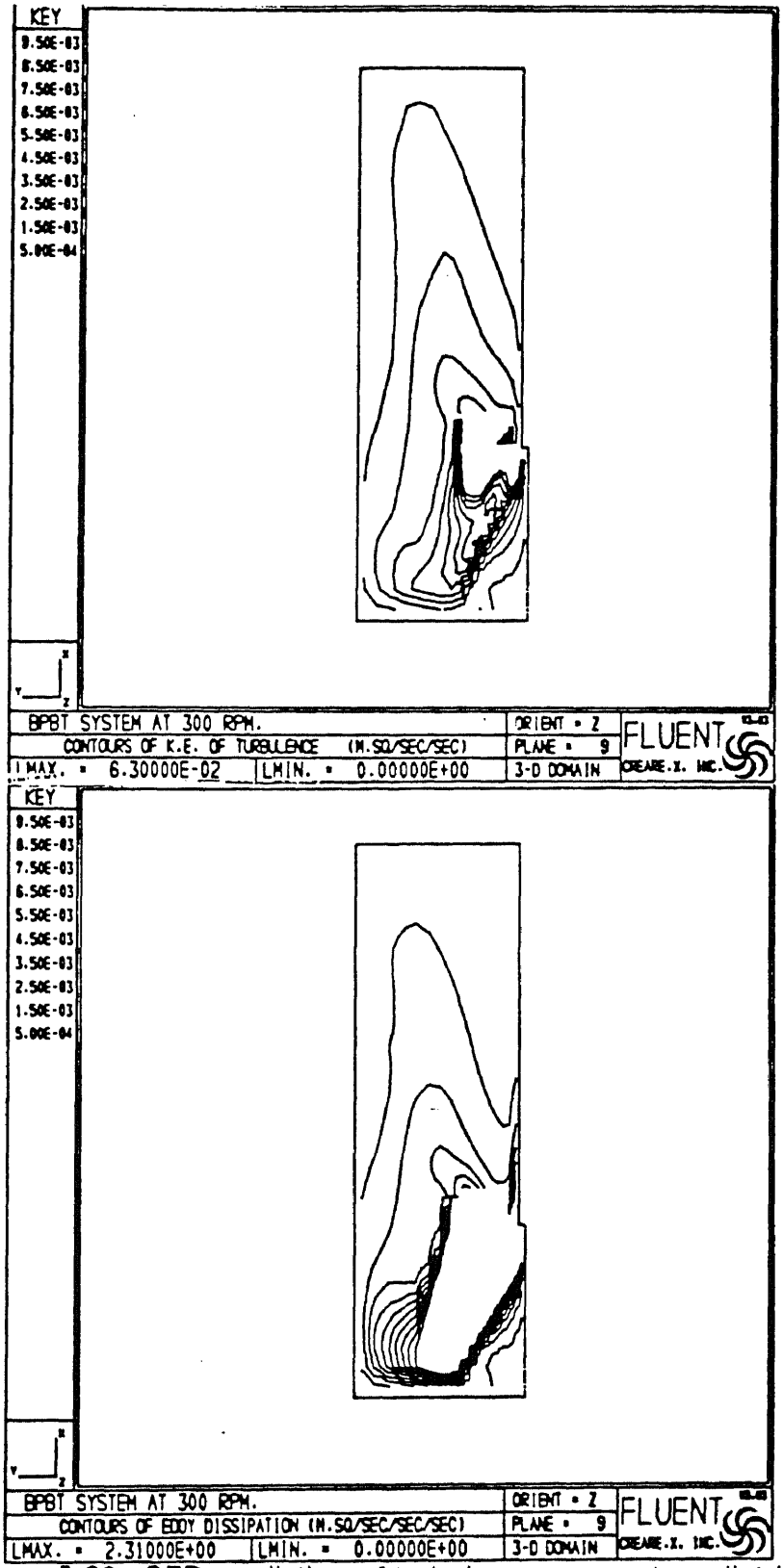

Figure 5-29. CFD prediction of turbulence parameters distribution in the vessel. System: baffled PBT. Contours for (a) turbulence kinetic energy; (b) dissipation rate.

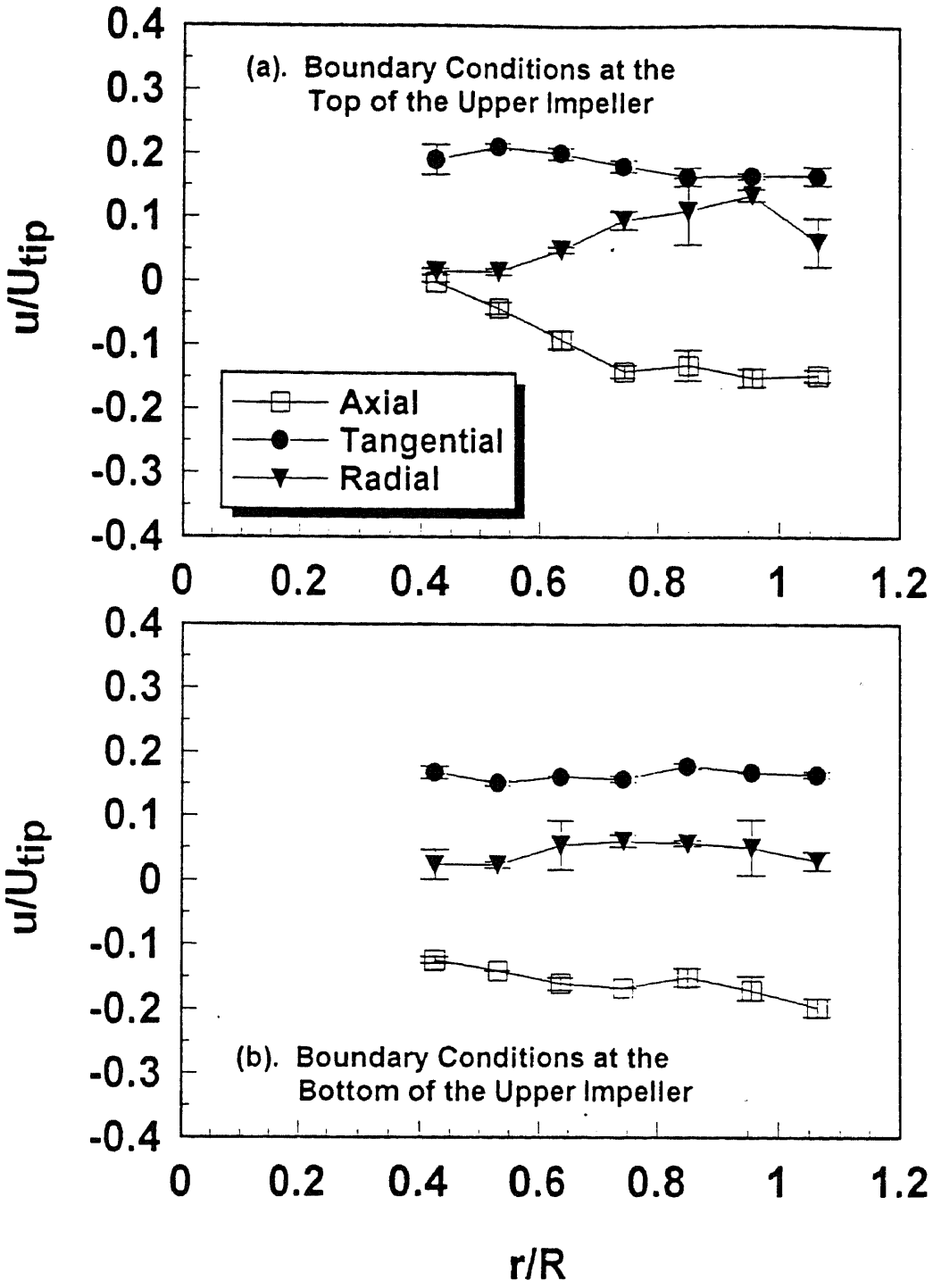

Figure 5-30. Experimentally determined (via LDV) velocities in the impeller region. These values were used as boundary conditions in the numerical CFD simulation. Double PBT system: (a) boundary conditions at the top of the upper impeller; (b) boundary conditions at the bottom of the upper impeller. Positive values indicate upwards velocities (for the axial direction). Error bars indicate standard deviation of duplicate experiments.

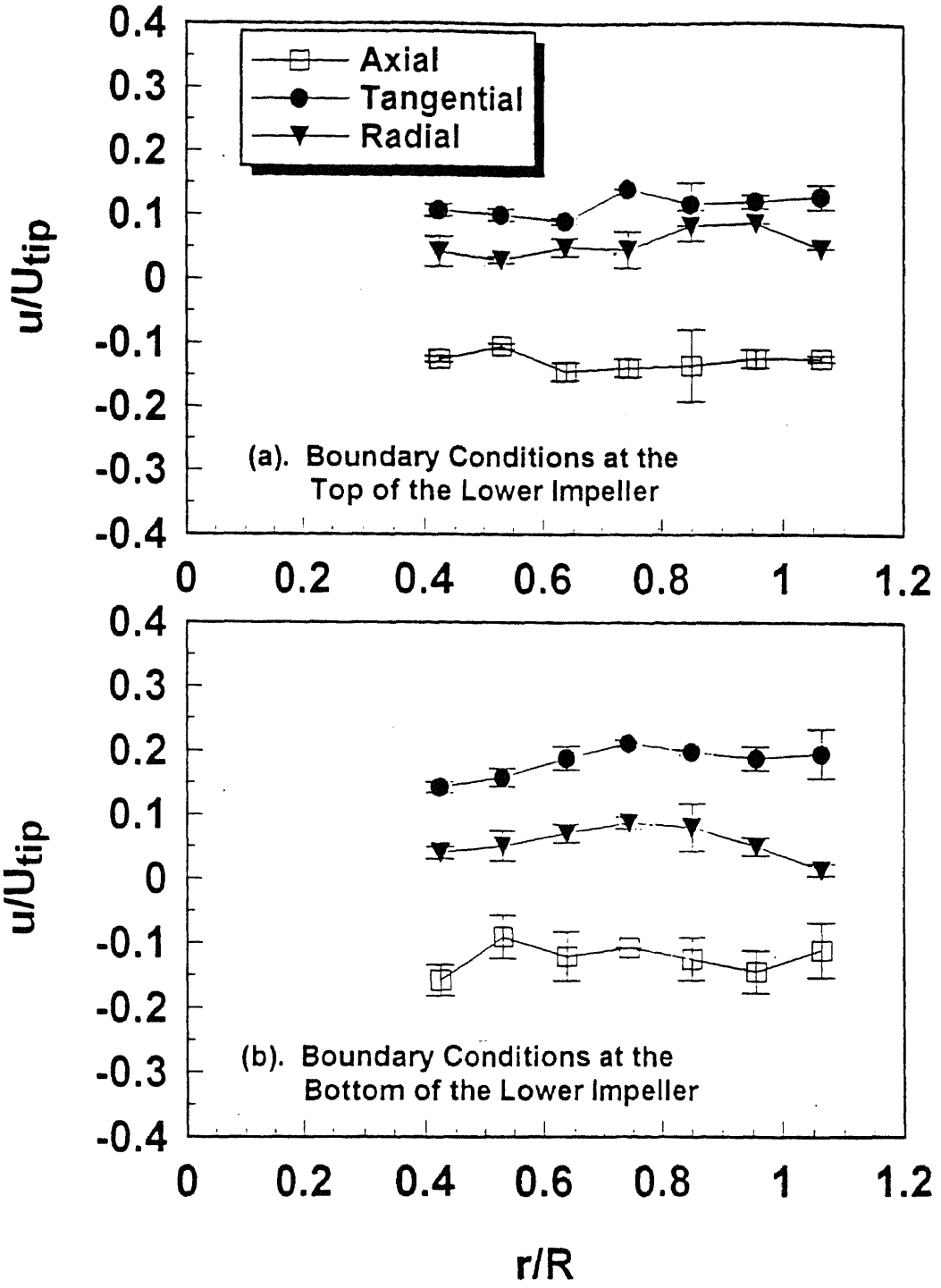

Figure 5-31. Experimentally determined (via LDV) velocities in the impeller region. These values were used as boundary conditions in the numerical CFD simulation. Double PBTs system: (a) boundary conditions at the top of the lower impeller; (b) boundary conditions at the bottom of the lower impeller. Positive values indicate upwards velocities (for the axial direction). Error bars indicate standard deviation of duplicate experiments.

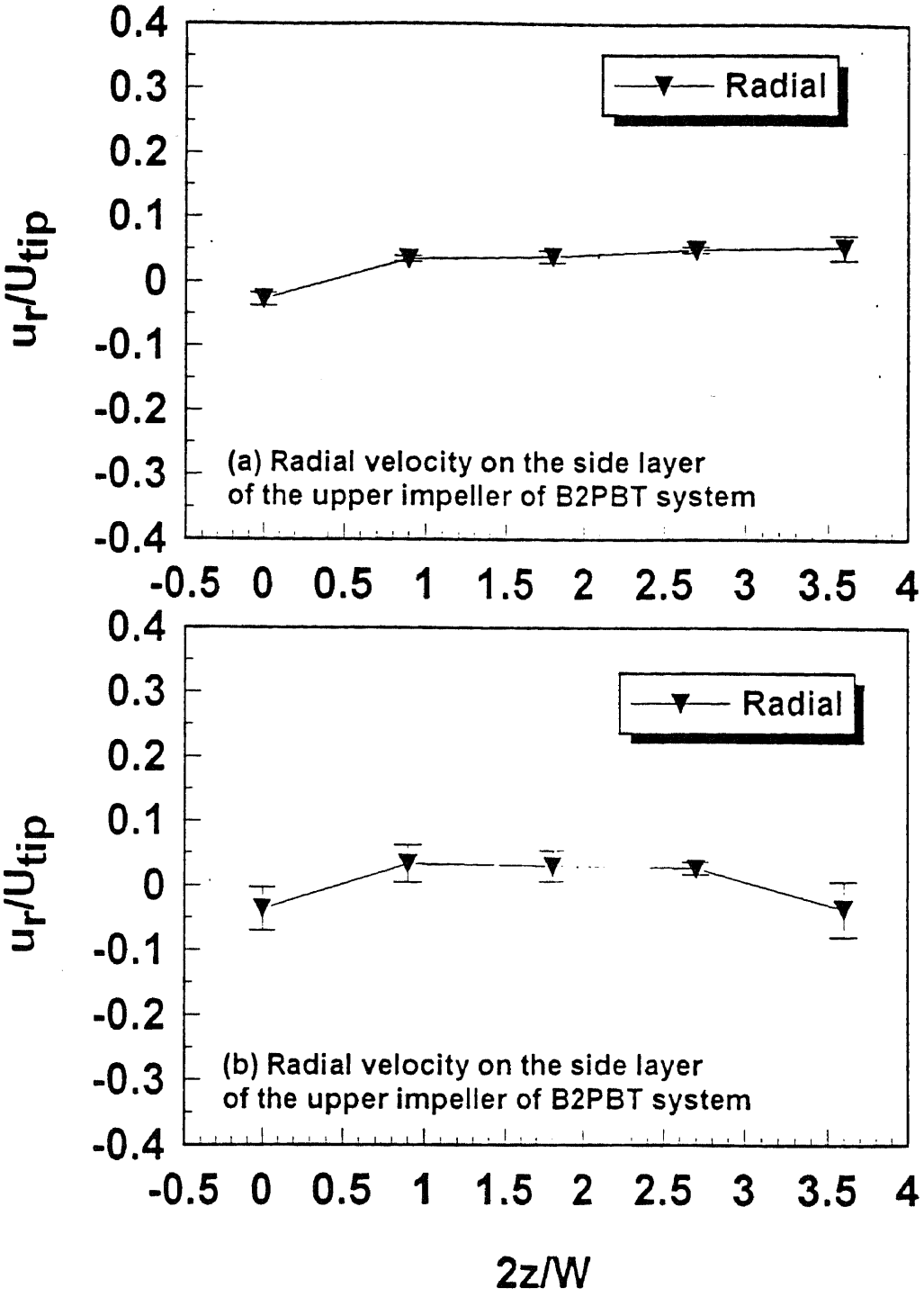

Figure 5-32. Experimentally determined (via LDV) radial velocities on the side layer of the impeller region. B2PBT system: (a) upper impeller; (b) Lower impeller. Negative value indicate outwards direction from impeller. Error bars indicate standard deviation of duplicate experiments.

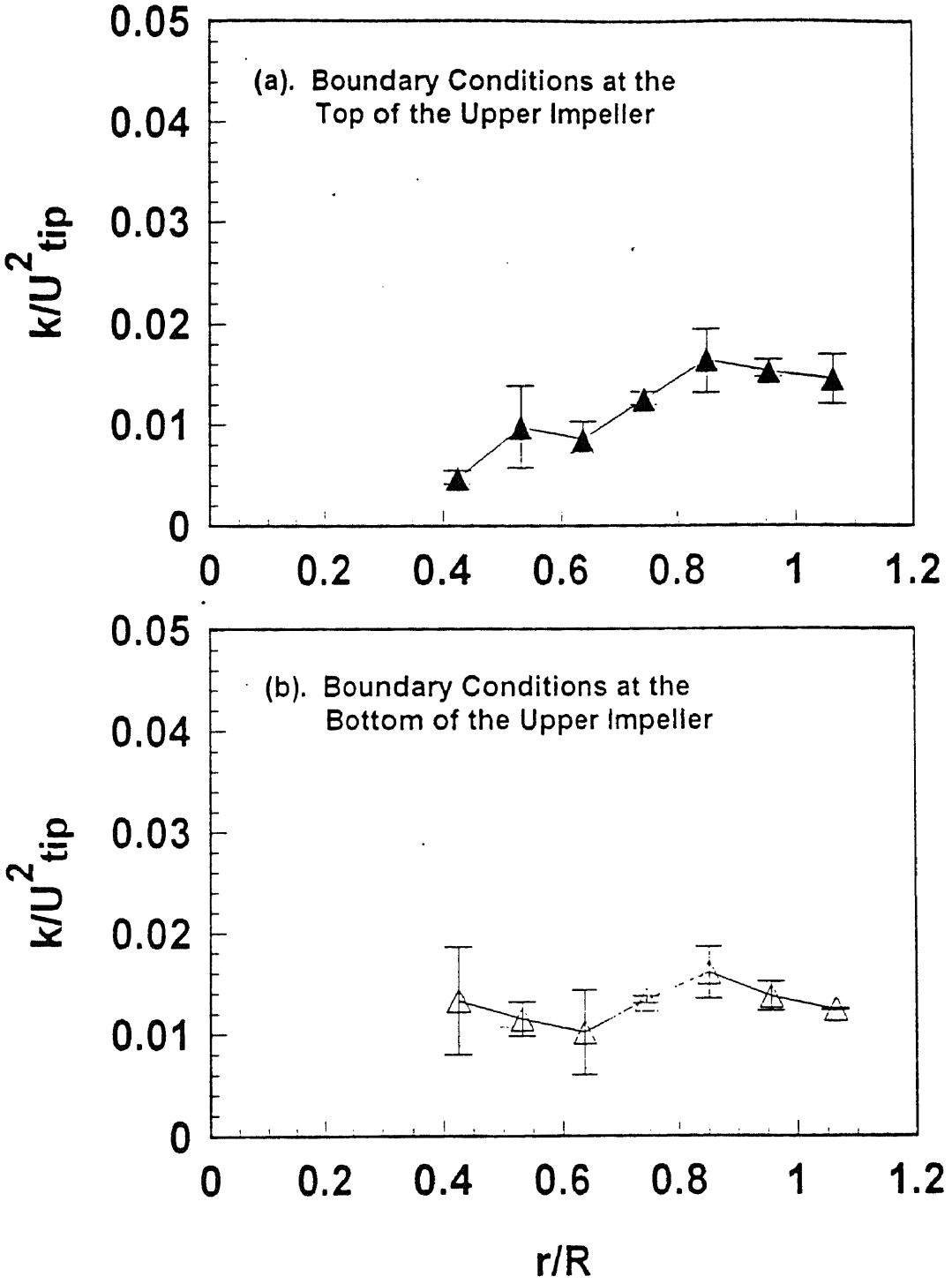

Figure 5-33. Turbulent kinetic energies in the impeller region. These values were used as the boundary conditions in the numerical CFD simulation. Double PBTs system: (a) boundary conditions at the top of the upper impeller; (b) boundary conditions at the bottom of the upper impeller. Error bars indicate standard deviation of duplicate experiments.

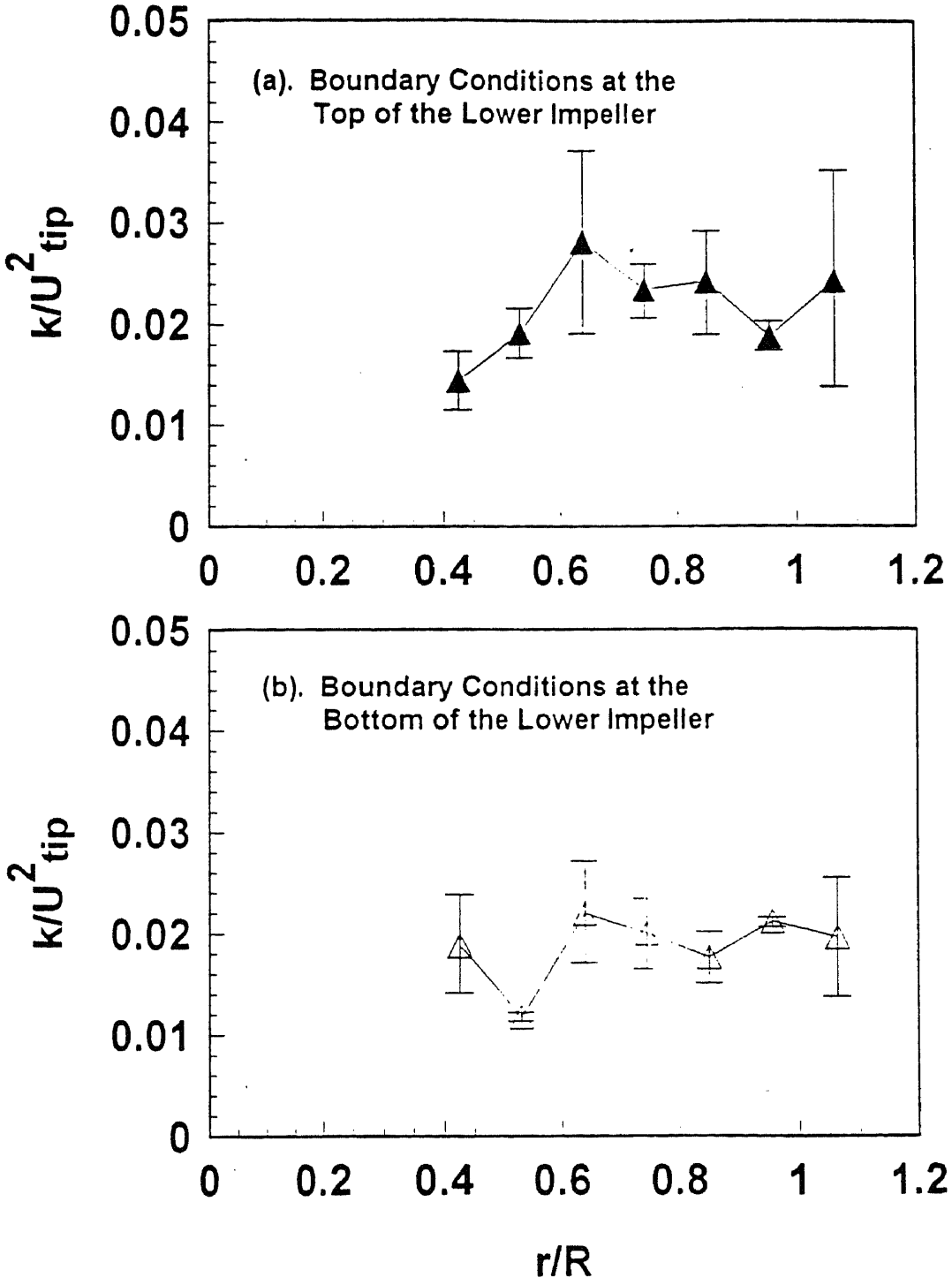

Figure 5-34. Turbulent kinetic energies in the impeller region. These values were used as the boundary conditions in the numerical CFD simulation. Double PBTs system: (a) boundary conditions at the top of the lower impeller; (b) boundary conditions at the bottom of the lower impeller. Error bars indicate standard deviation of duplicate experiments.

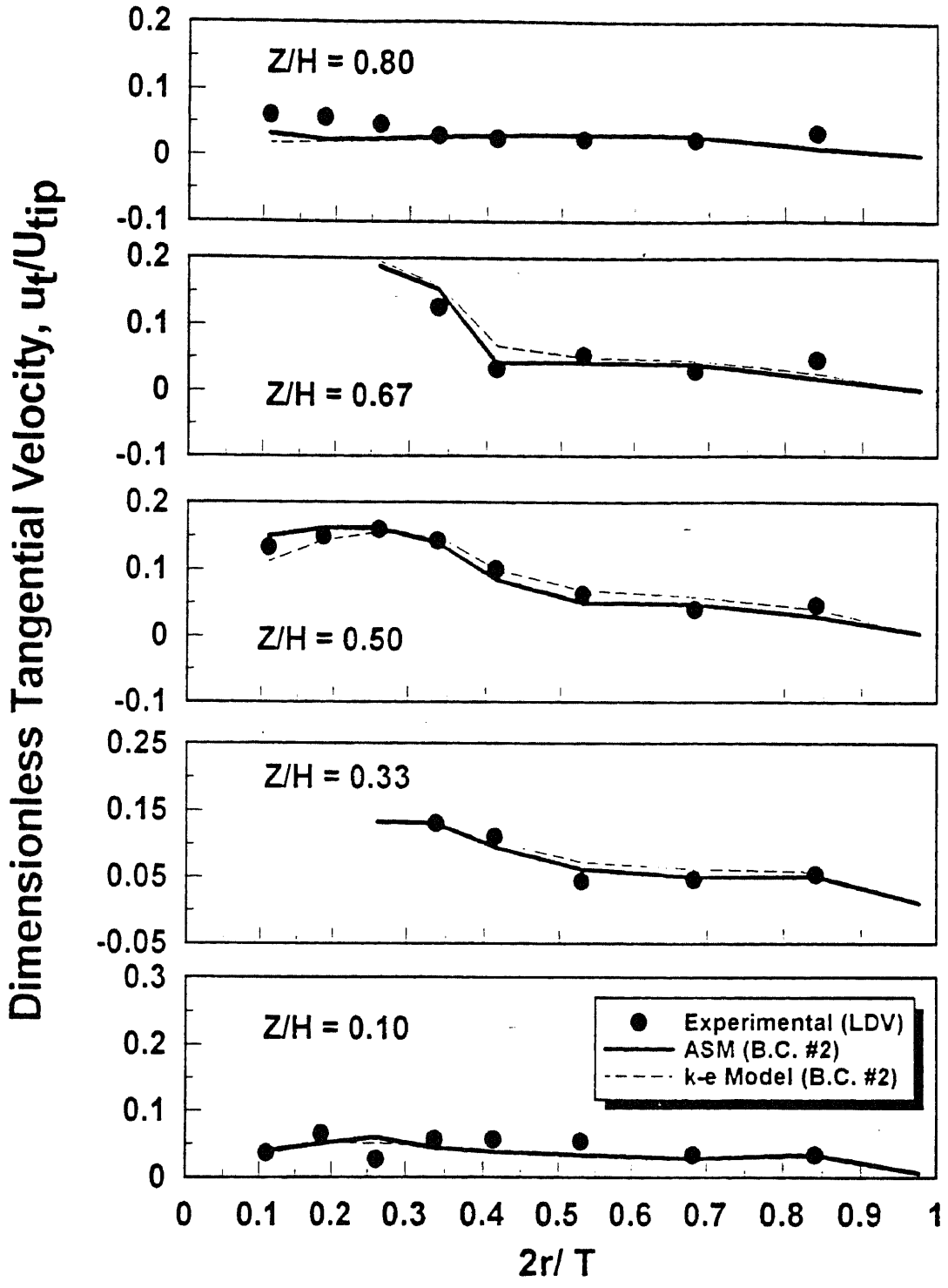

Figure 5-35. Comparison between experimental measurements and numerical predictions of the tangential velocities in double PBTs system.

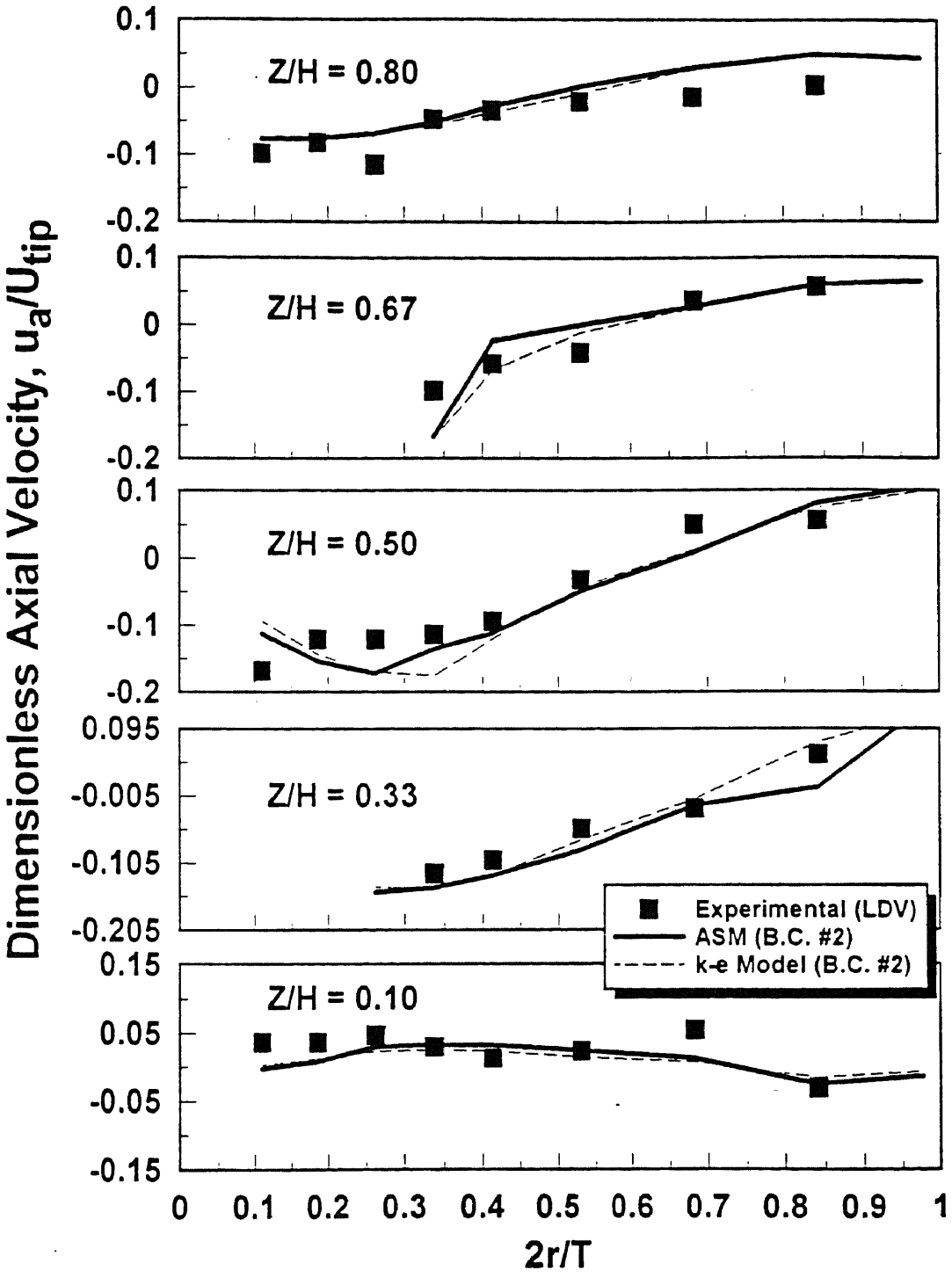

Figure 5-36. Comparison between experimental measurements and numerical predictions of the axial velocities in double PBTs system.

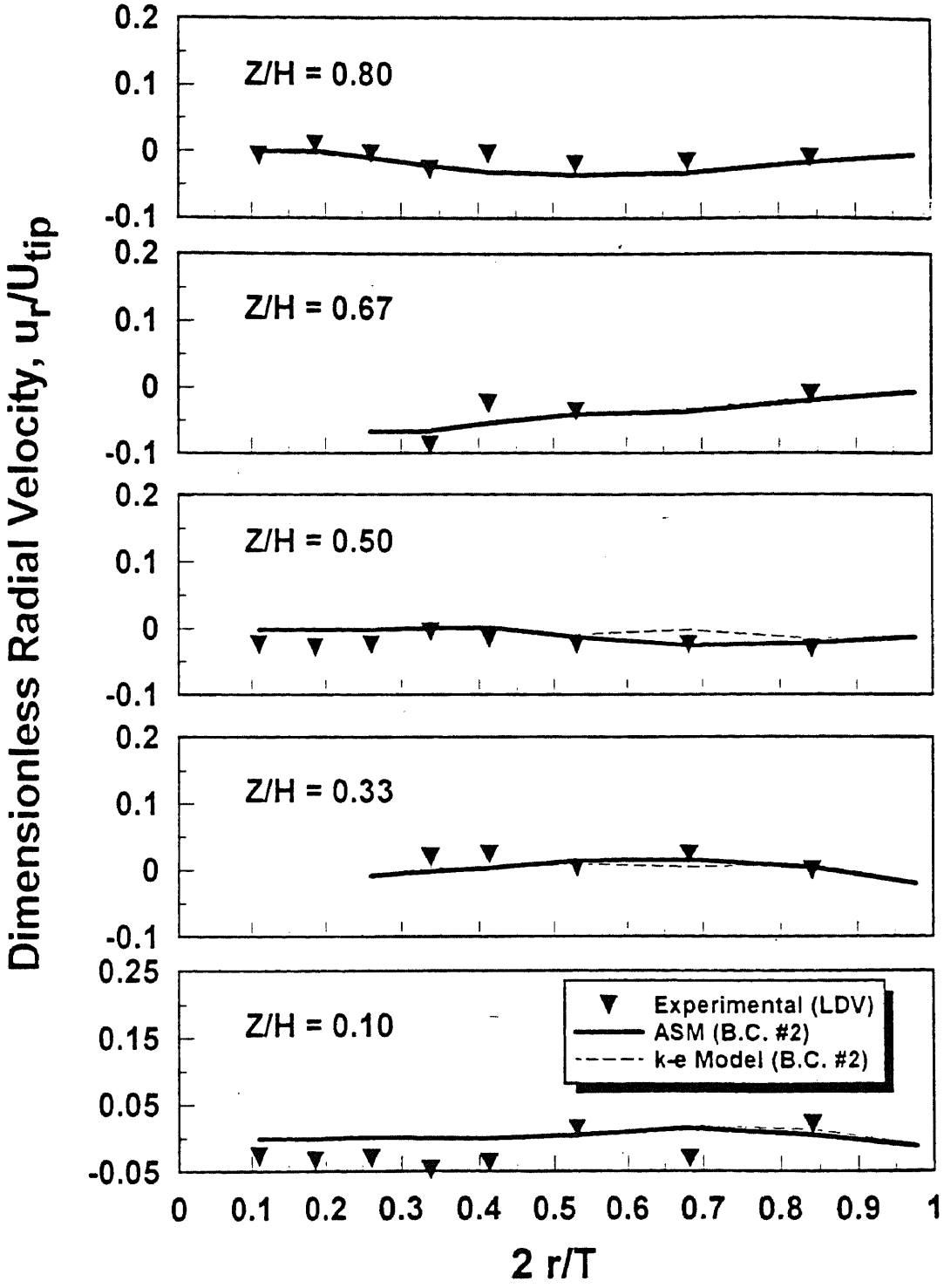

Figure 5-37. Comparison between experimental measurements and numerical predictions of the radial velocities in double PBTs system.

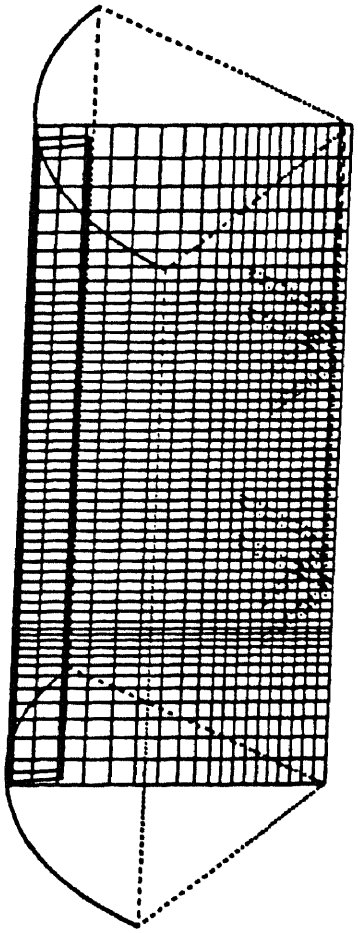

Figure 5-38. The computational grids for baffled double impeller system.

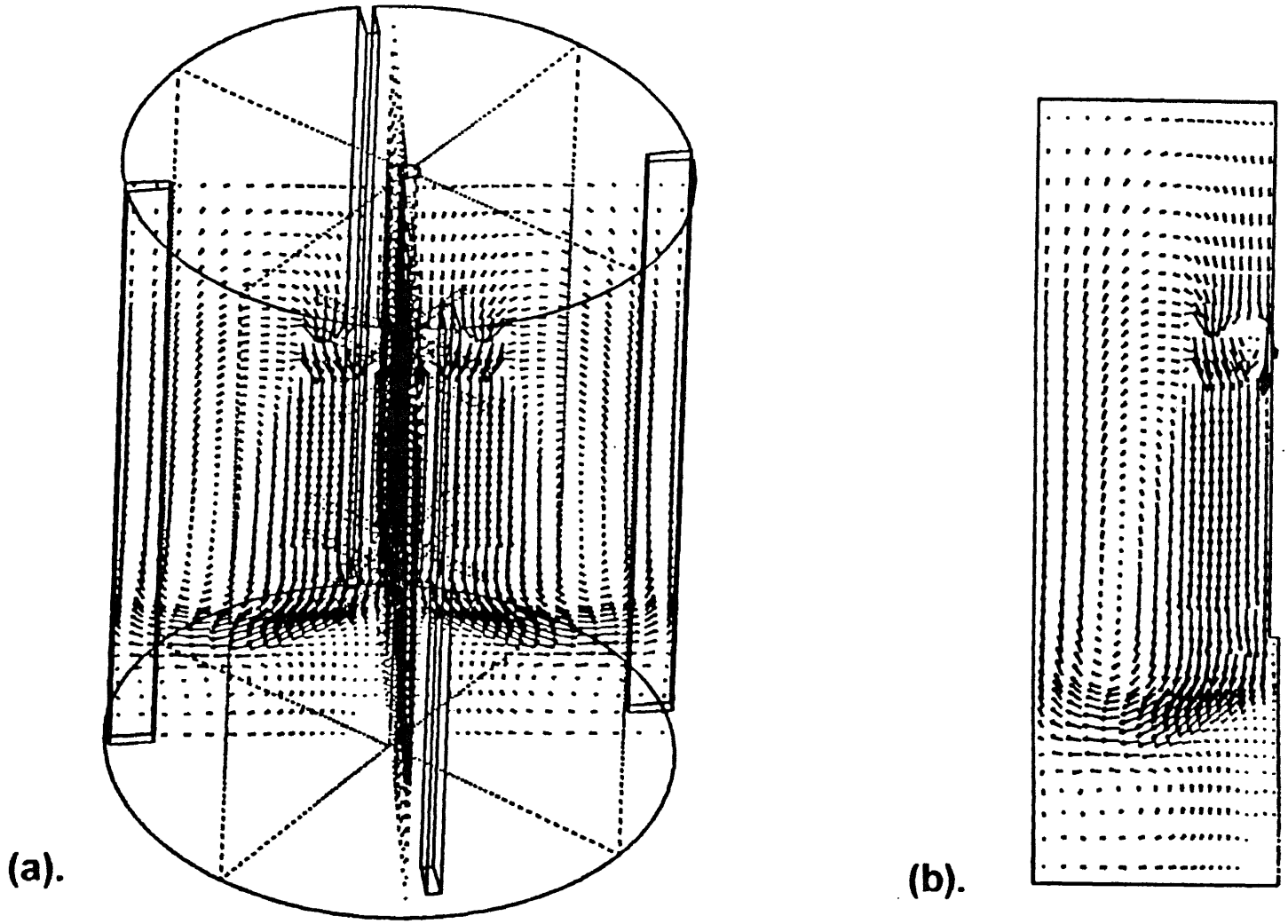

Figure 5-39. CFD prediction of velocity distribution in the vessel. System: baffled 2PBT. Boundary conditions: B.C. #2. Turbulence model: ASM. (a) Tridimensional view; (b) Bidimensional cross section across the impeller shaft (only one half section shown).

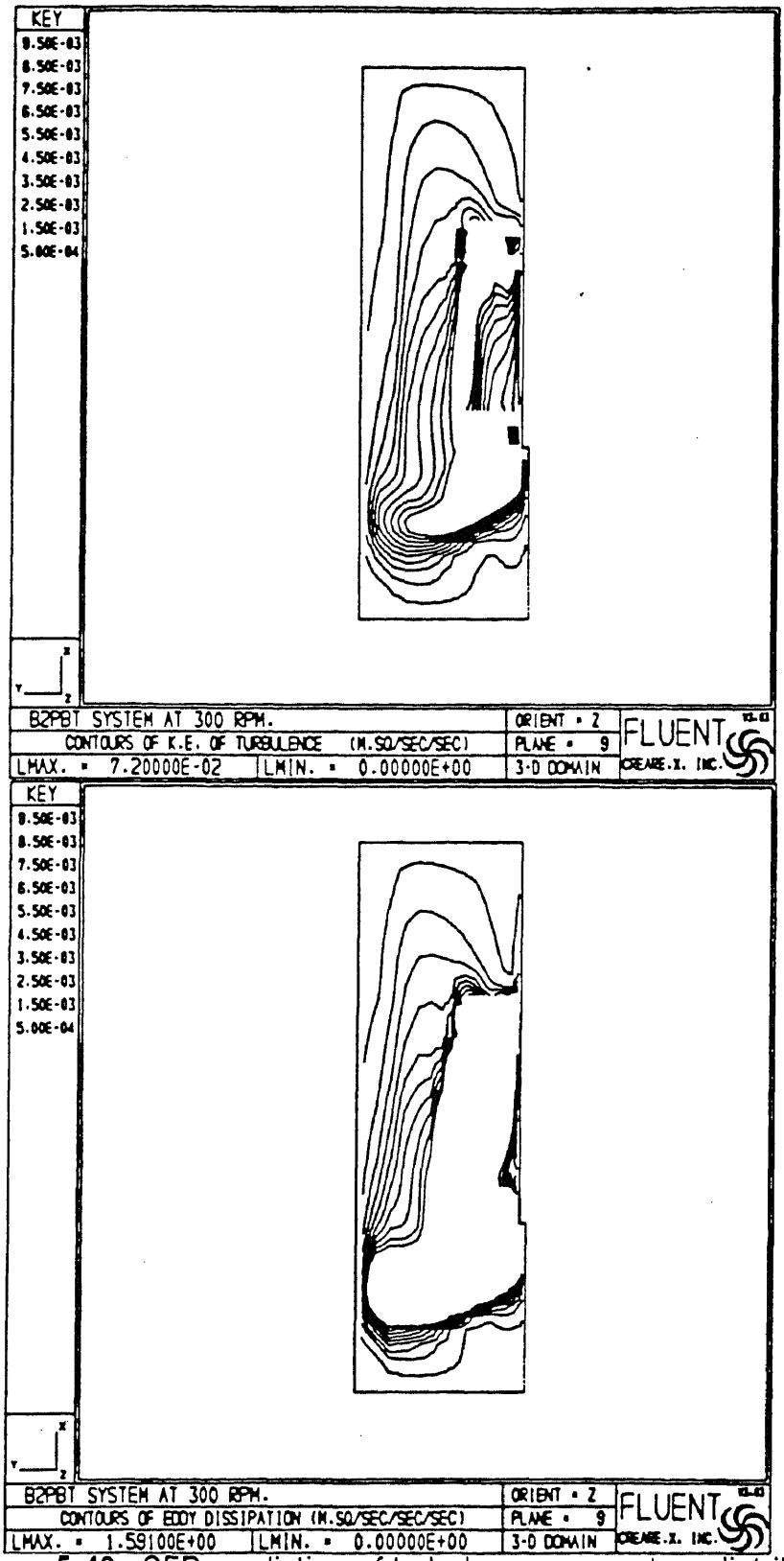

Figure 5-40. CFD prediction of turbulence parameters distribution in the vessel. System: baffled 2PBT. Contours for (a) turbulence kinetic energy; (b) dissipation rate.

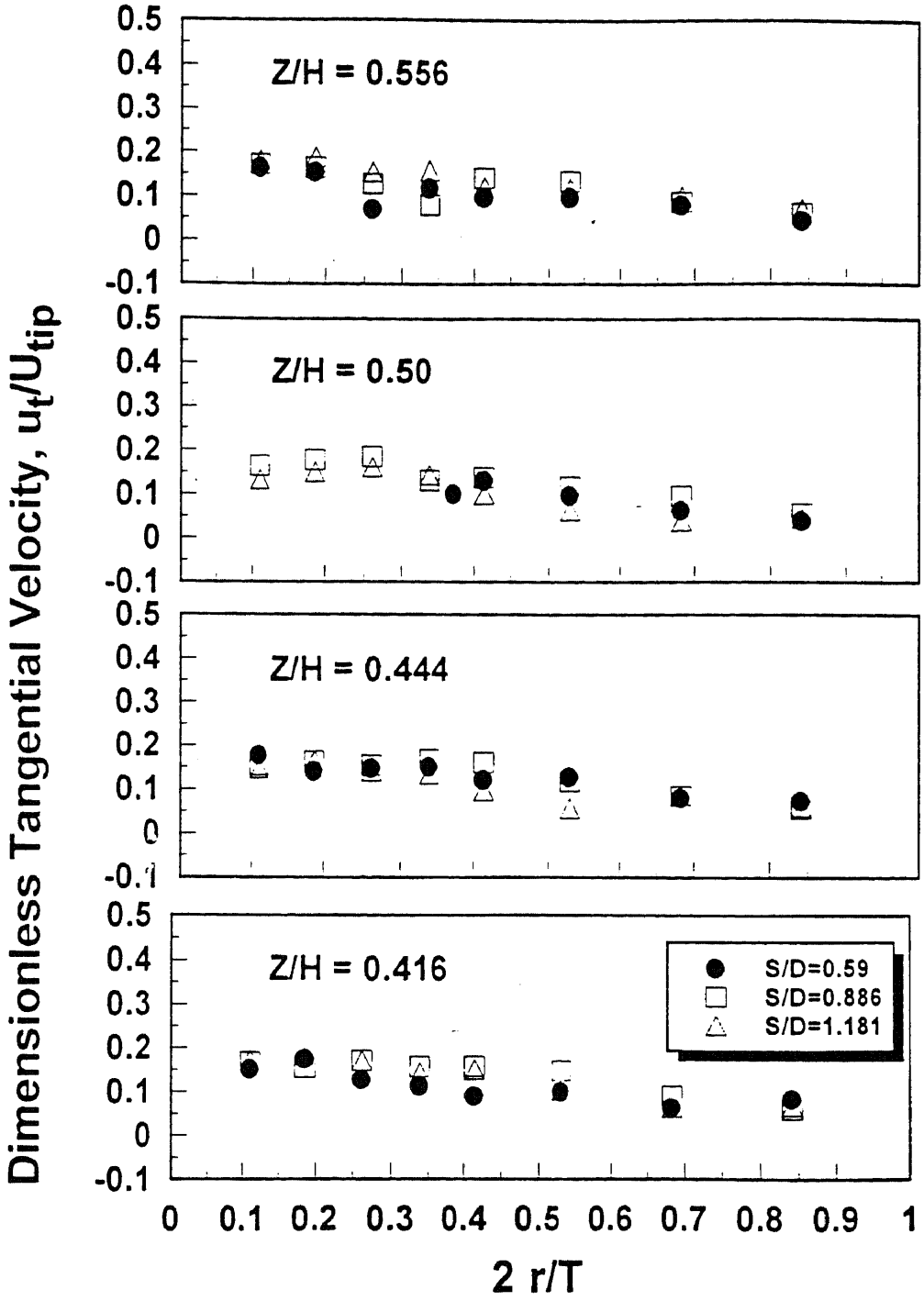

Figure 5-41. LDV measurements of the dimensionless tangential velocities along the dimensionless tank radius at impeller spacing (S/D) equal to 0.59,0.886, and 1.181 for (Z/H) at 0.416, 0.444, 0.50, and 0.556 of the B2PBT system.

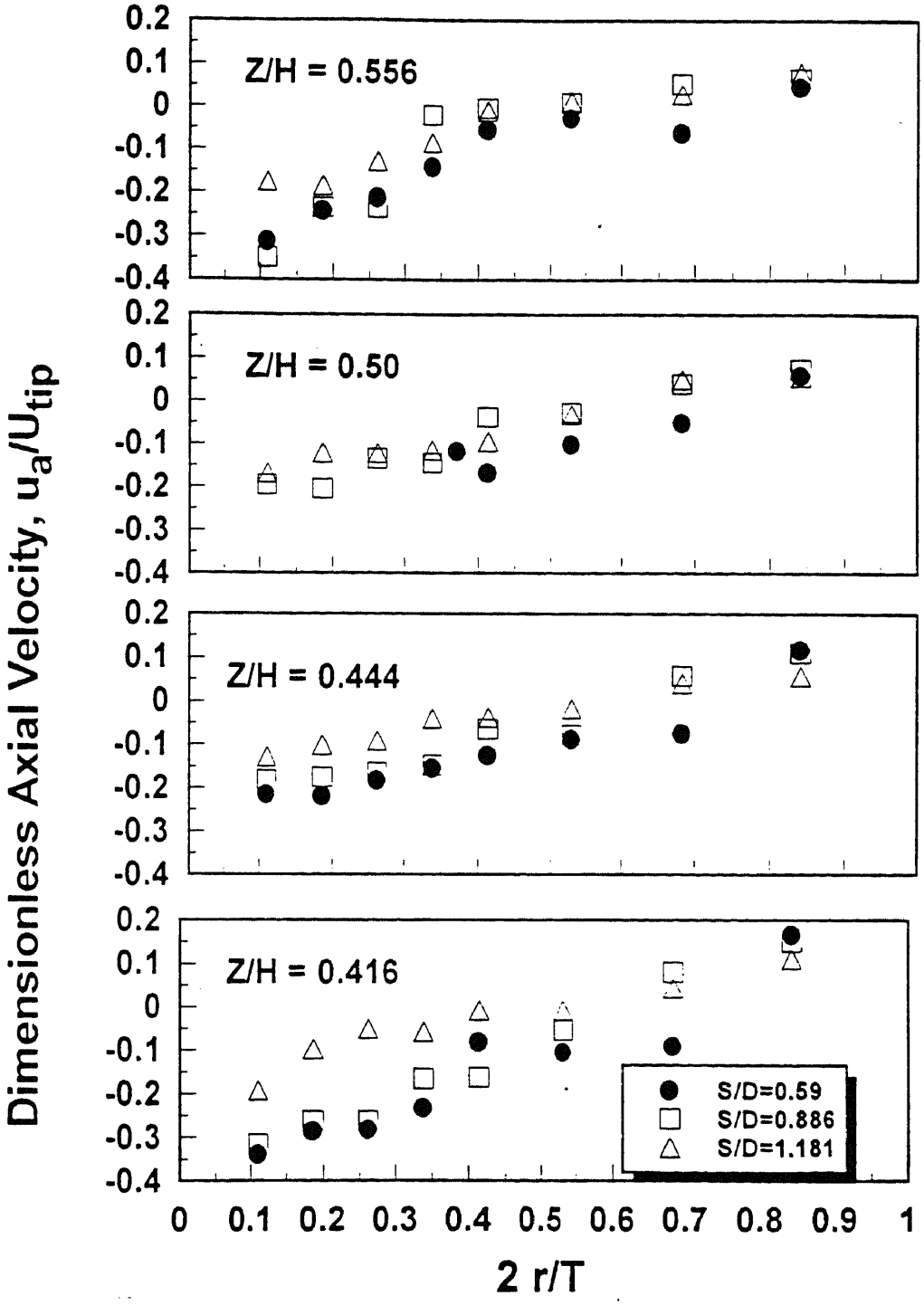

Figure 5-42. LDV measurements of the dimensionless axial velocities along the dimensionless tank radius at impeller spacing (S/D) equal to 0.59, 0.886, and 1.181 for (Z/H) at 0.416, 0.444, 0.50, and 0.556 of the B2PBT system.

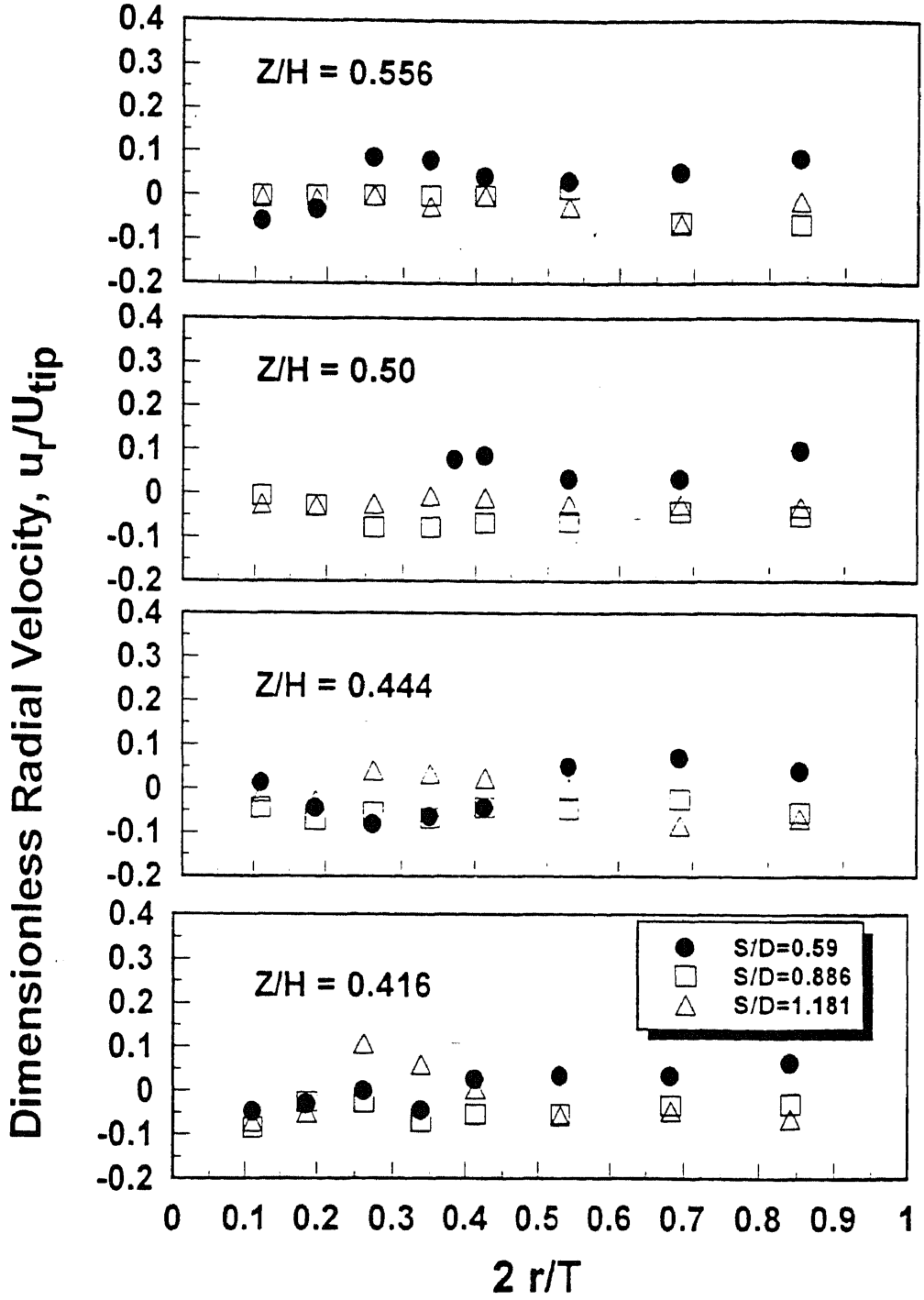

Figure 5-43. LDV measurements of the dimensionless radial velocities along the dimensionless tank radius at impeller spacing (S/D) equal to 0.59, 0.886, and 1.181 for (Z/H) at 0.416, 0.444, 0.50, and 0.556 of the B2PBT system.

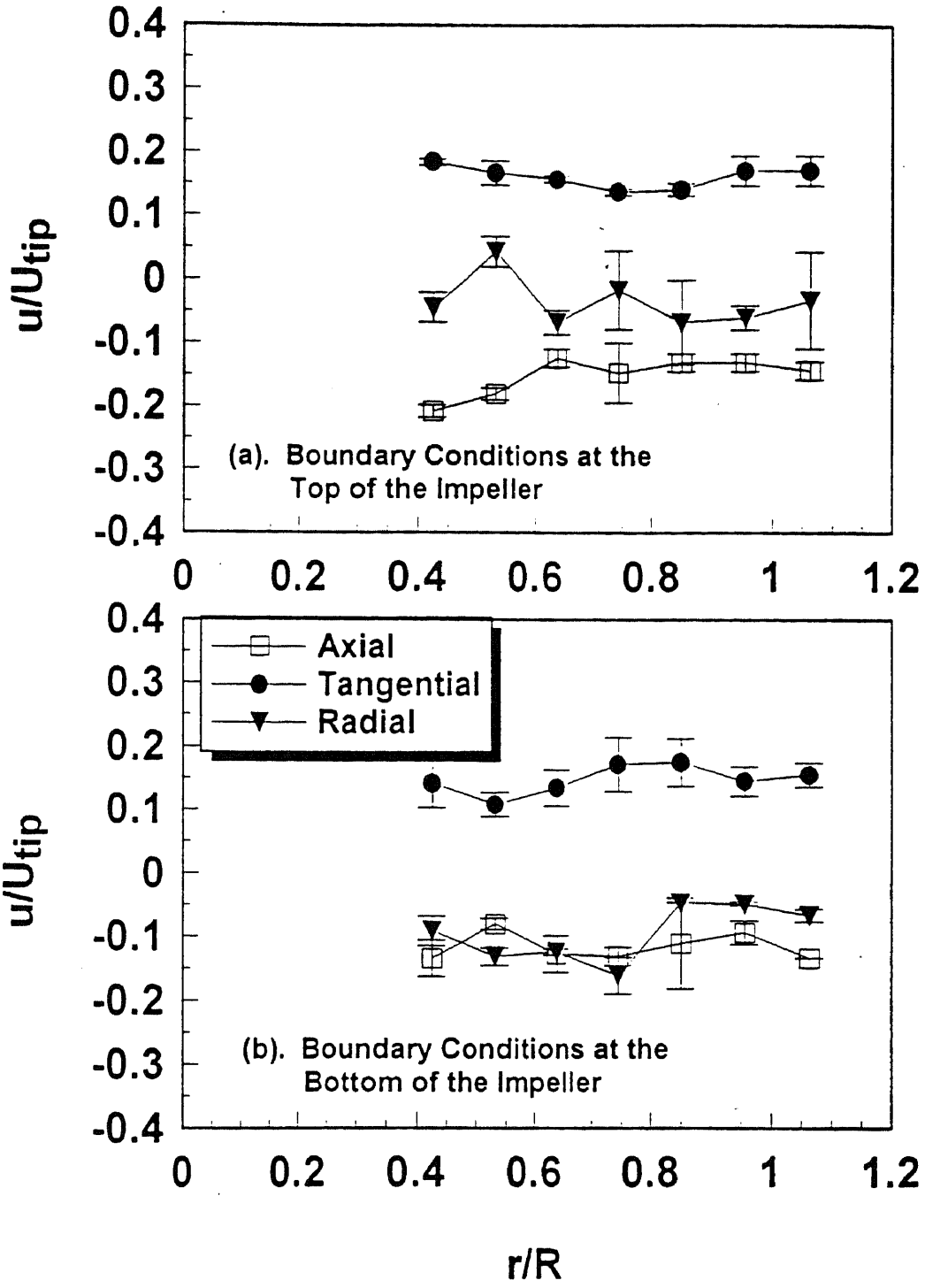

Figure 5-44. Experimentally determined (via LDV) velocities in the impeller region. These values were used as the boundary conditions in the numerical CFD simulation. Single FBT system: (a) boundary conditions at the top of the impeller; (b) boundary conditions at the bottom of the impeller. Positive values indicate upwards velocities (for the axial direction). Error bars indicate standard deviation of duplicate experiments.

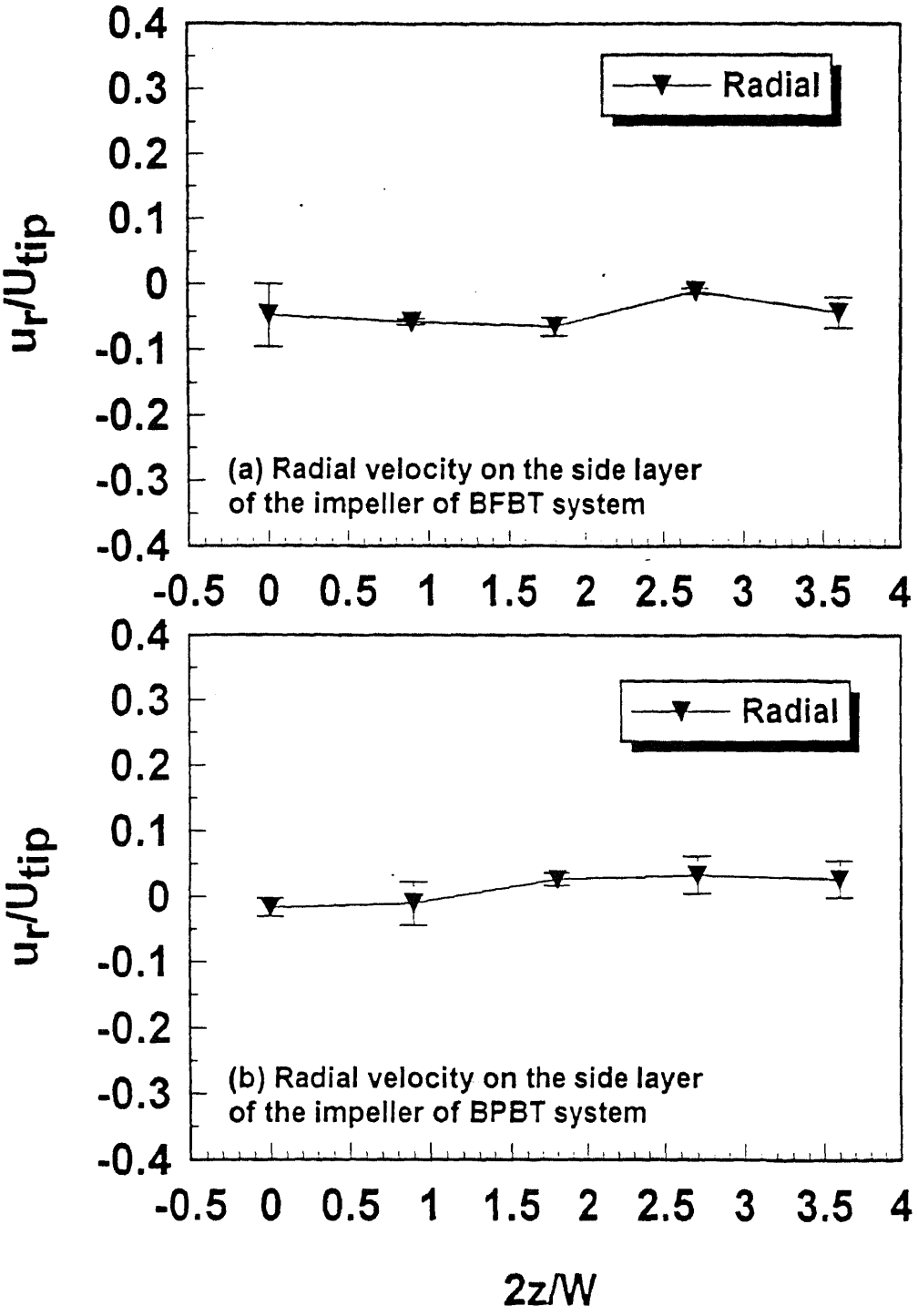

Figure 5-45. Experimentally determined (via LDV) radial velocities on the side layer of the impeller region. (a) BFPT system; (b) BPBT system. Negative value indicate outwards direction from impeller. Error bars indicate standard deviation of duplicate experiments.

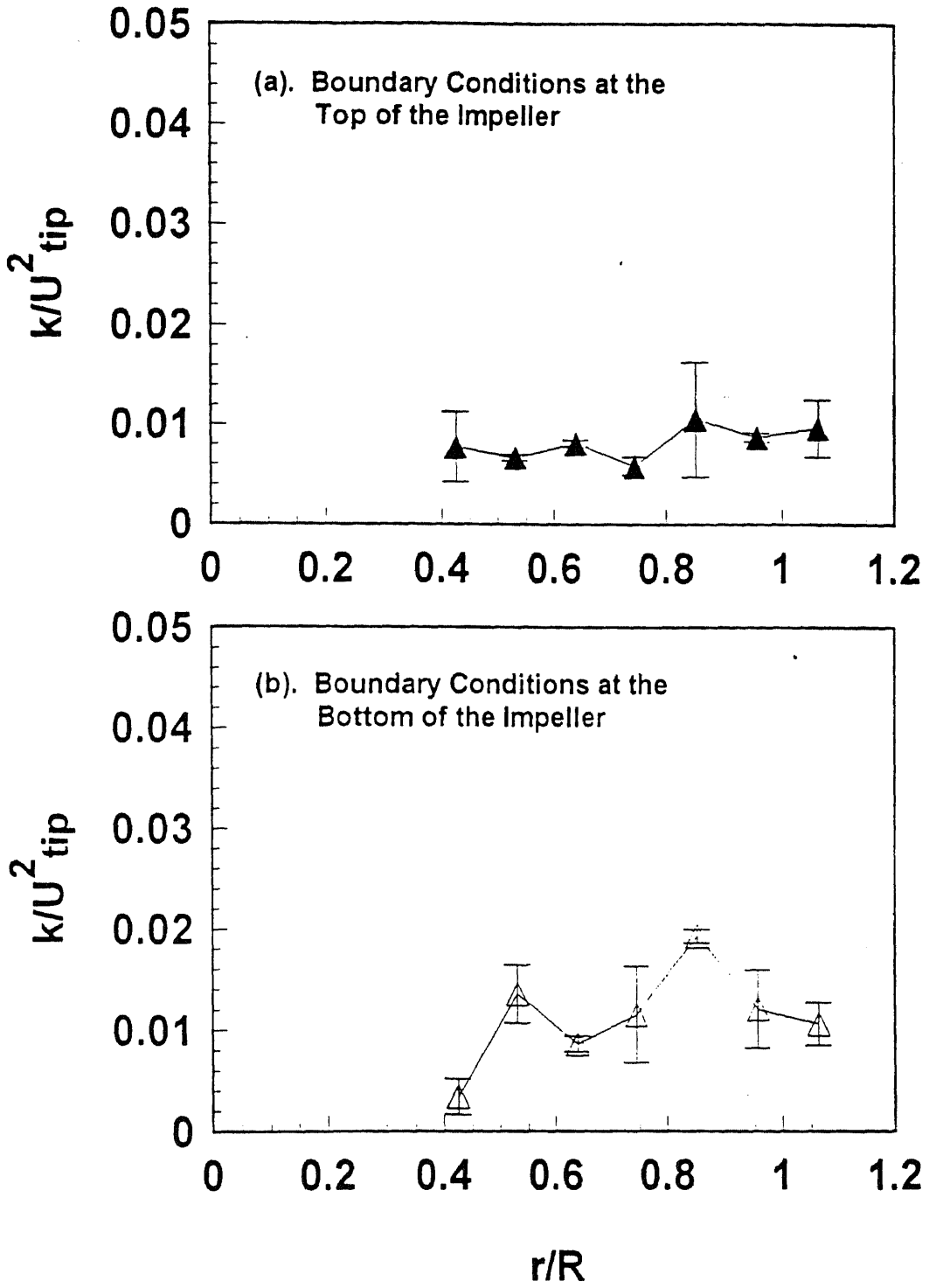

Figure 5-46. Turbulent kinetic energies in the impeller region. These values were used as the boundary conditions in the numerical CFD simulations. Single FBT system: (a) boundary conditions at the top of the impeller; (b) boundary conditions at the bottom of the impeller. Error bars indicate standard deviation of duplicate expriments.

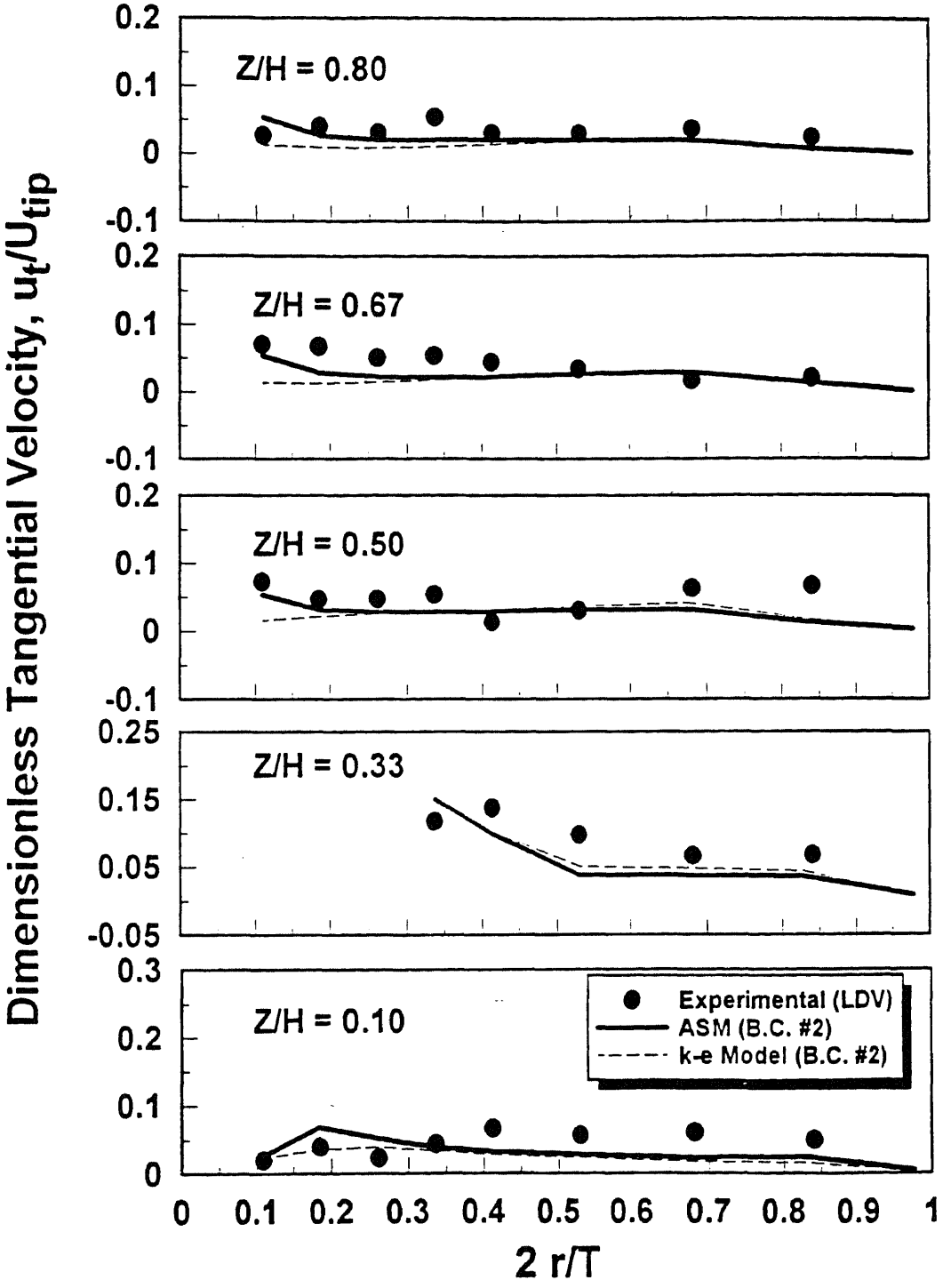

Figure 5-47. Comparison between experimental measurements and numerical predictions of the tangential velocities in single FBT system.

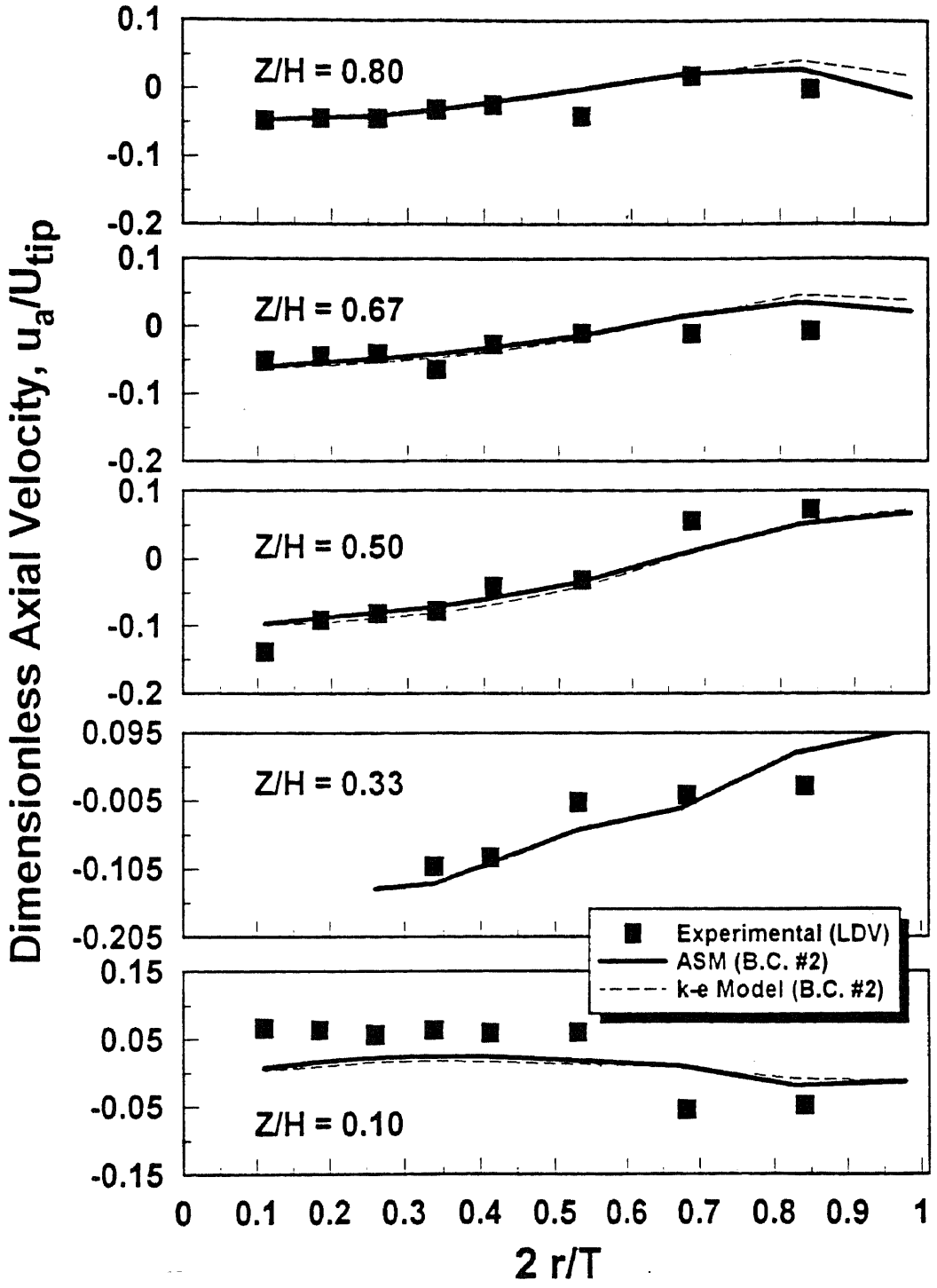

Figure 5-48. Comparison between experimental measurements and numerical predictions of the axial velocities in single FBT system.

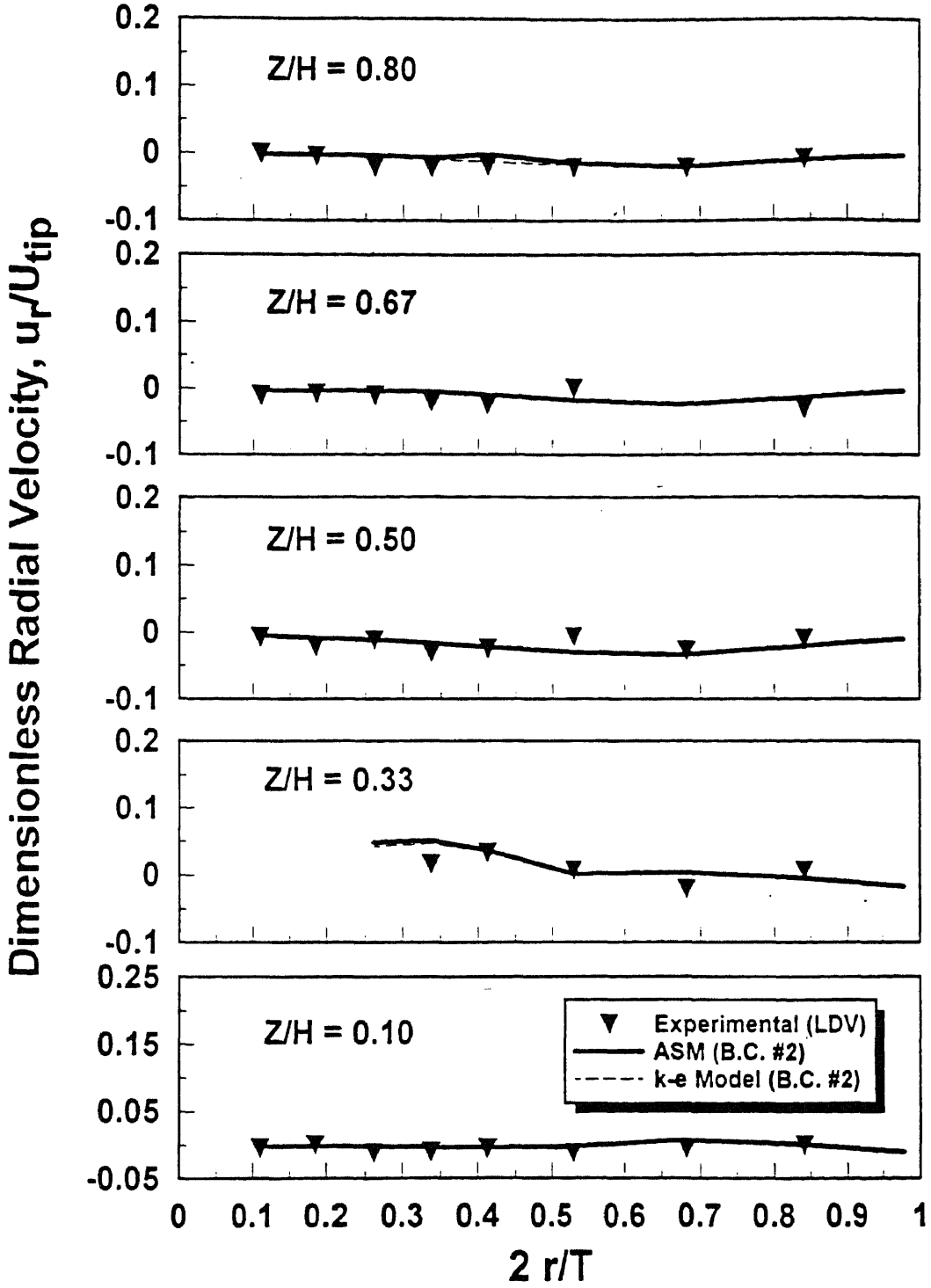

Figure 5-49. Comparison between experimental measurements and numerical predictions of the radial velocities in single FBT system.

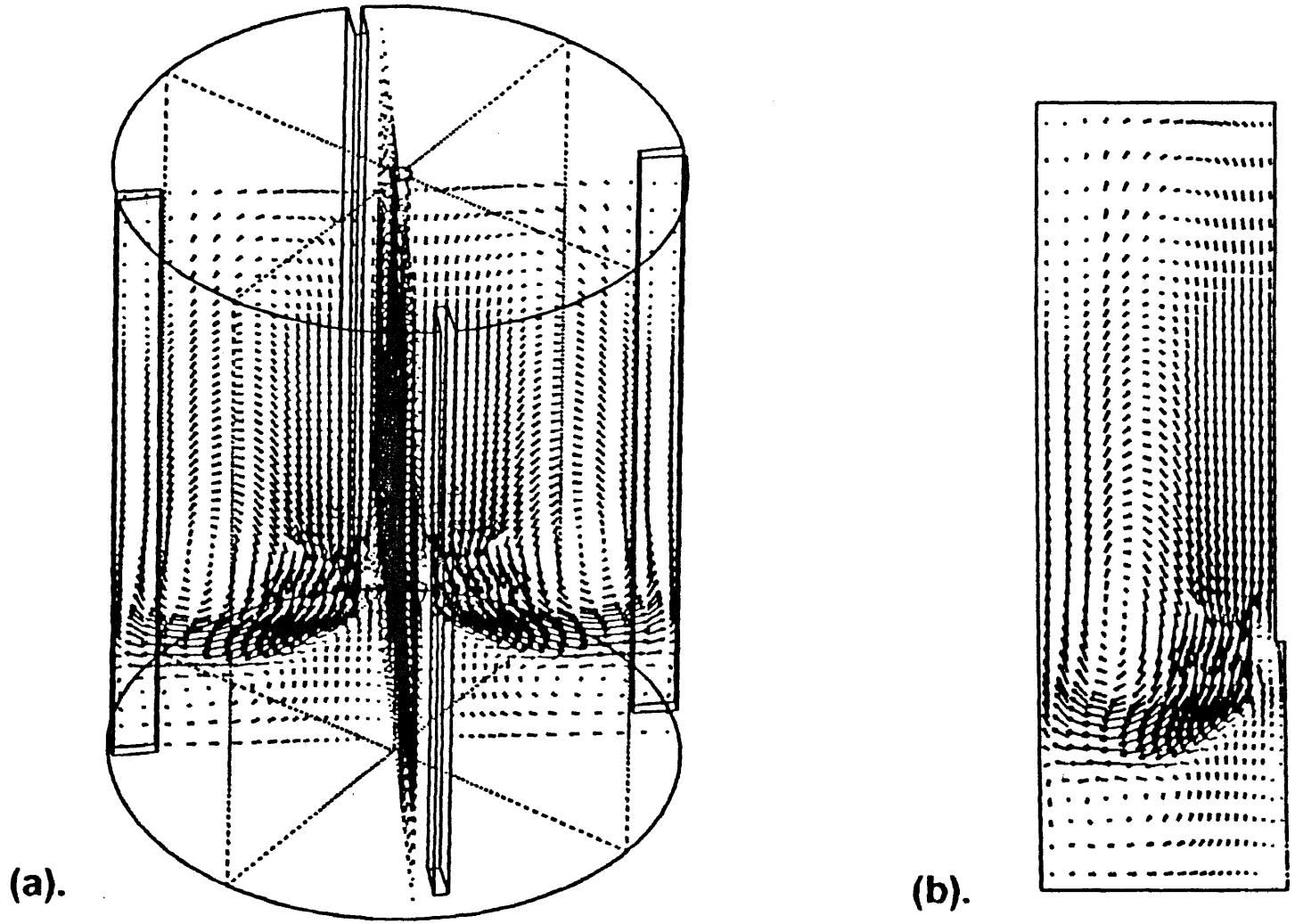

Figure 5-50. CFD prediction of velocity distribution in the vessel. System: baffled single FBT. boundary conditions: B.C. #2. Turbulence model: ASM. (a) Tridimensional view; (b) Bidimensional cross section across the impeller shaft (only one half section shown).

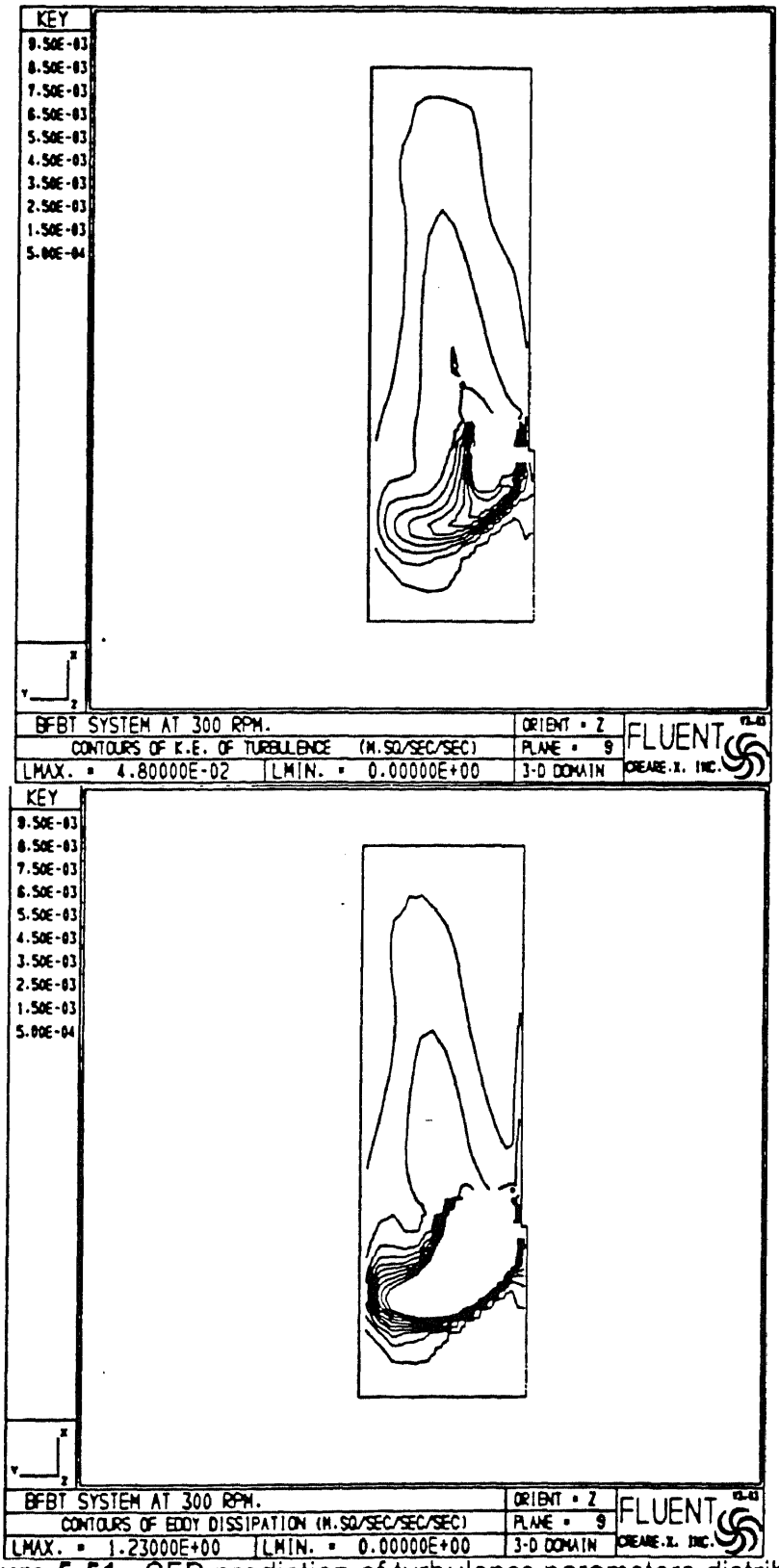

Figure 5-51. CFD prediction of turbulence parameters distribution in the vessel. System: baffled FBT. Contours for (a) turbulence kinetic energy; (b) dissipation rate.

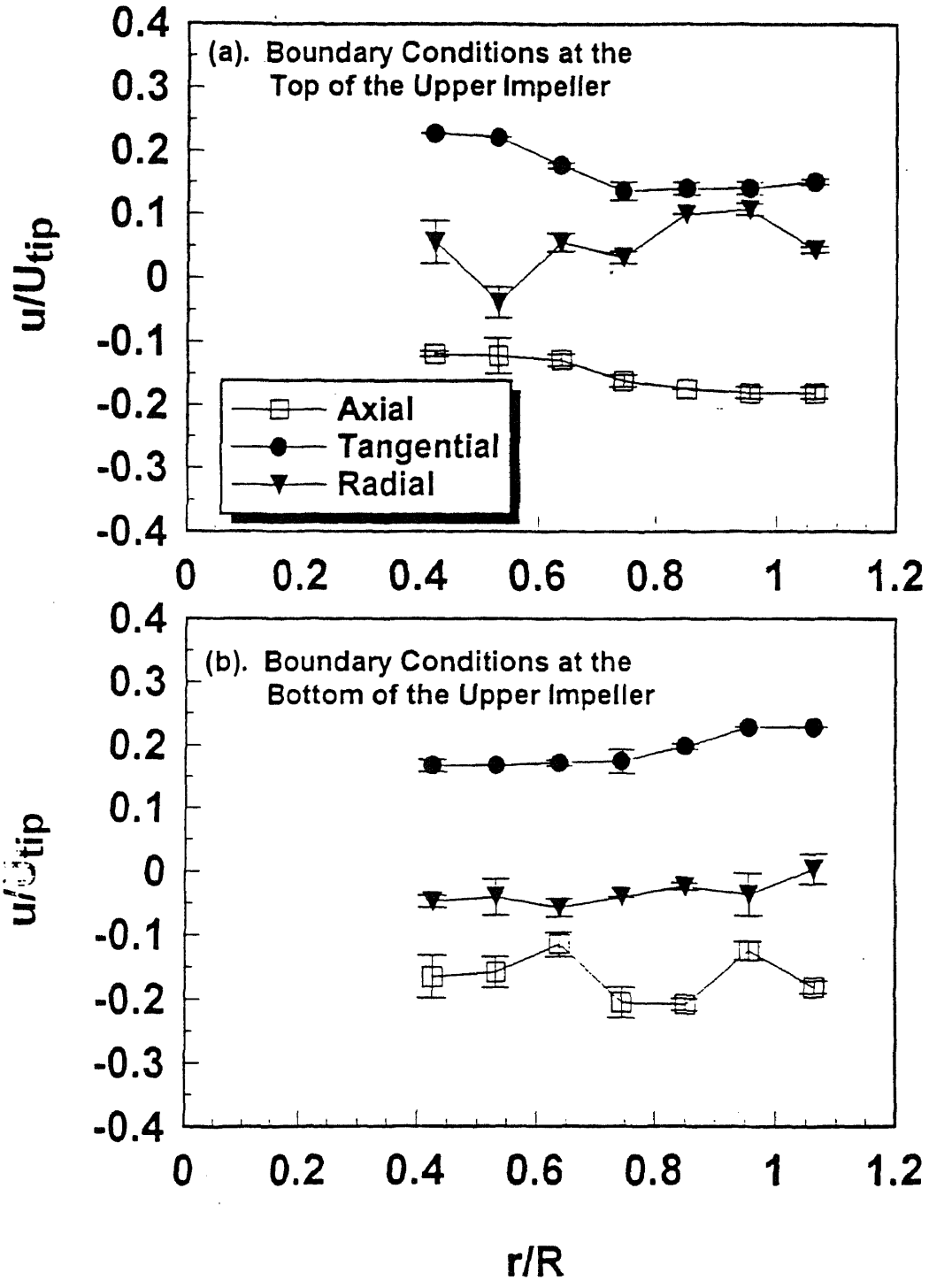

Figure 5-52. Experimentally determined (via LDV) velocities in the impeller region. These values were used as boundary conditions in the numerical CFD simulation. Double FBTs system: (a) boundary conditions at the top of the upper impeller; (b) boundary conditions at the bottom of the upper impeller. Positive values indicate upwards velocities (for the axial direction). Error bars indicate standard deviation of duplicate experiments.

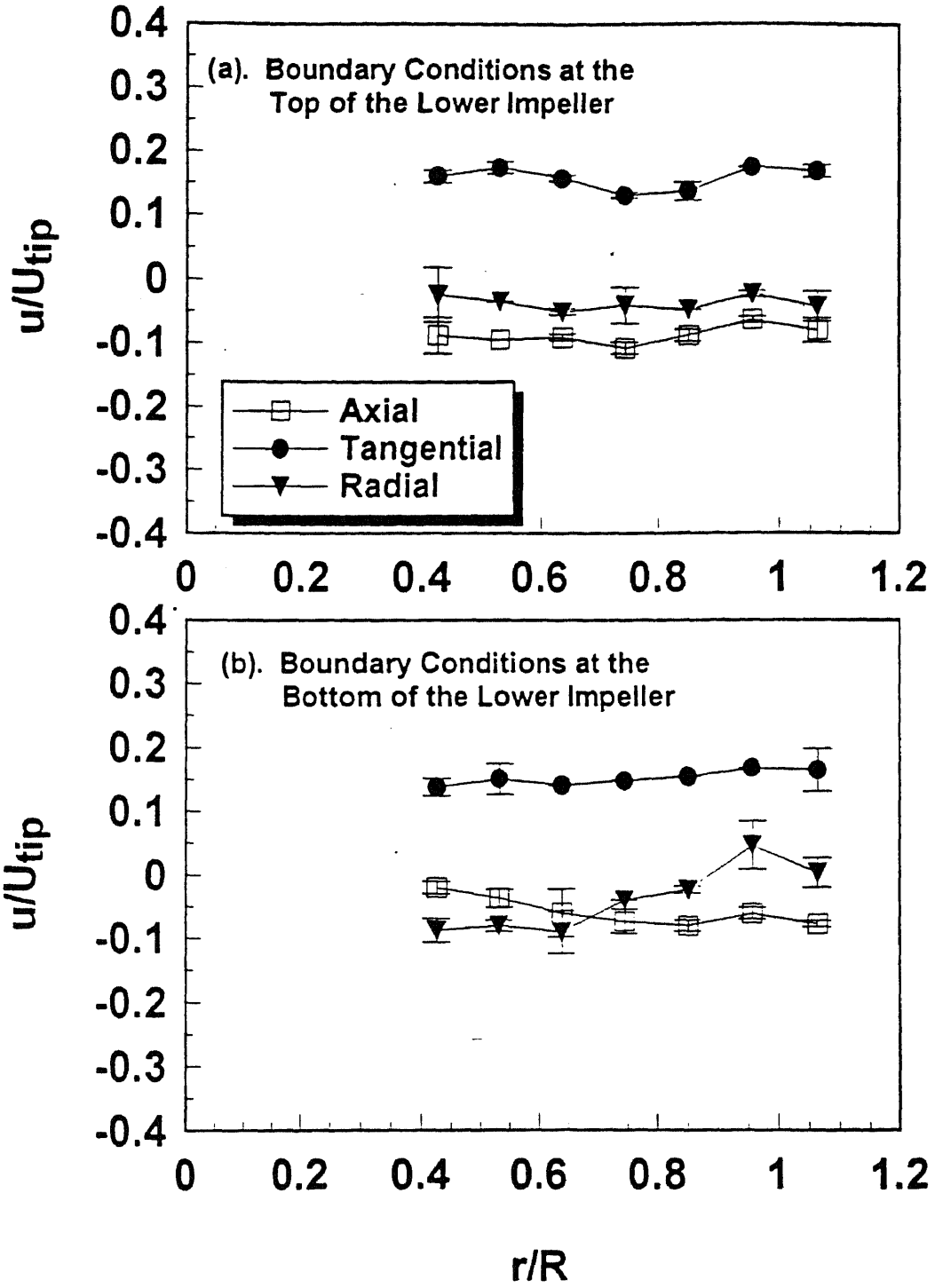

Figure 5-53. Experimentally determined (via LDV) velocities in the impeller region. These values were used as boundary conditions in the numerical CFD simulation. Double FBTs system: (a) boundary conditions at the top of the lower impeller; (b) boundary conditions at the bottom of the lower impeller. Positive values indicate upwards velocities (for the axial direction). Error bars indicate standard deviation of duplicate experiments.

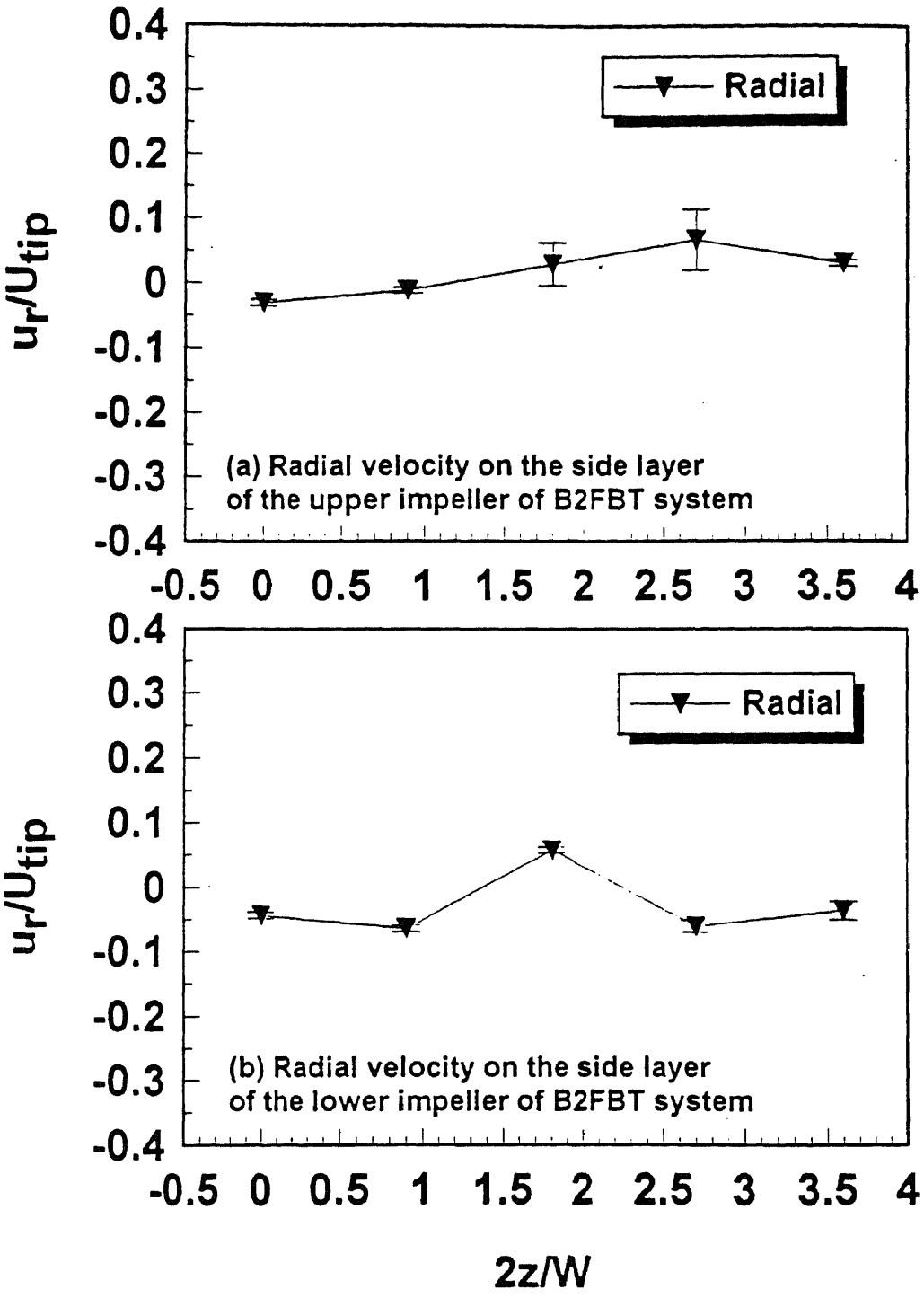

Figure 5-54. Experimentally determined (via LDV) radial velocities on the side layer of the impeller region. B2FBT system: (a) upper impeller; (b) Lower impeller. Negative value indicate outwards direction from impeller. Error bars indicate standard deviation of duplicate experiments.

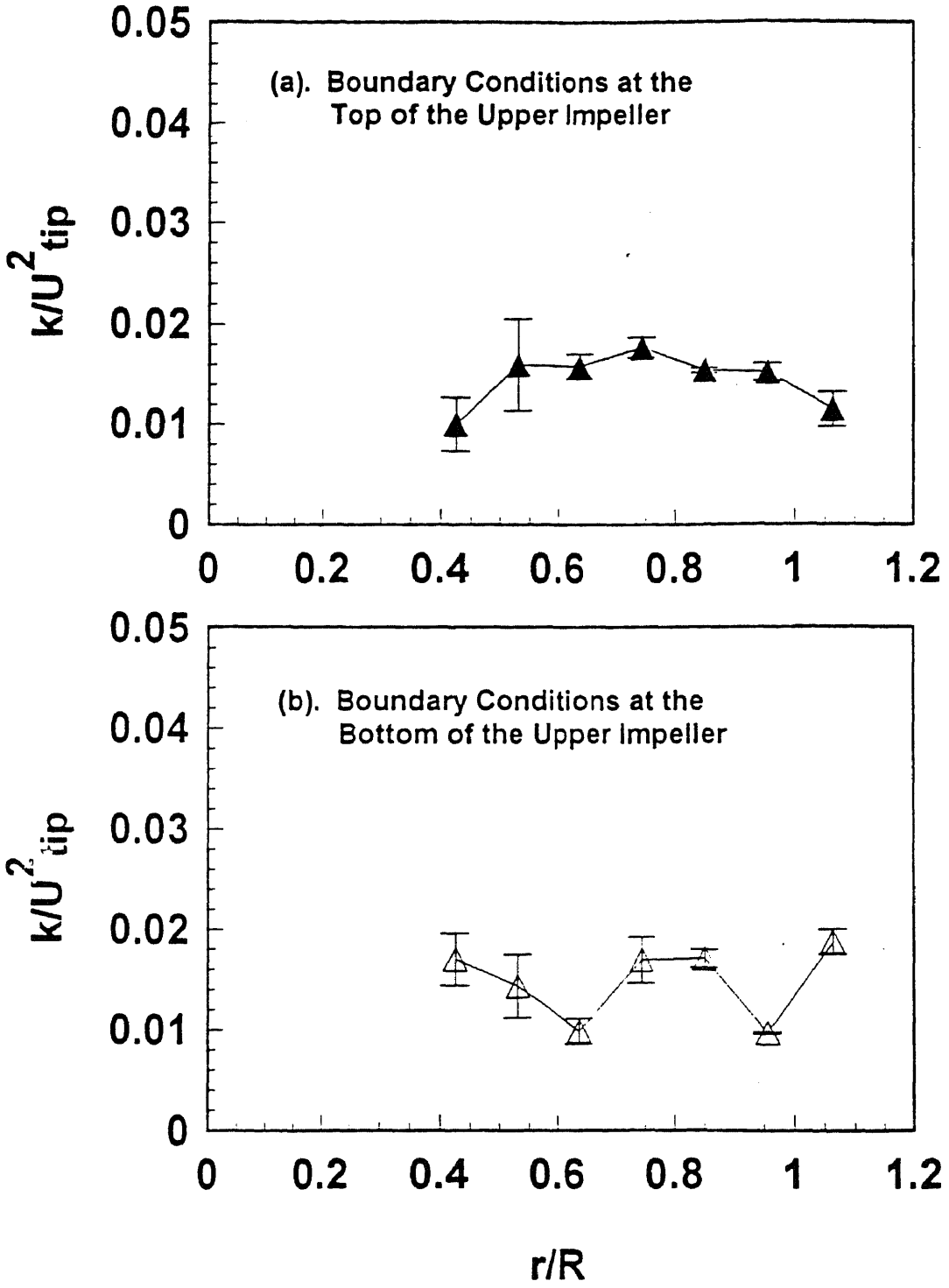

Figure 5-55. Turbulent kinetic energies in the impeller region. These values were used as the boundary conditions in the numerical CFD simulation. Double FBTs system: (a) boundary conditions at the top of the upper impeller; (b) boundary conditions at the bottom of the upper impeller. Error bars indicate standard deviation of duplicate experiments.

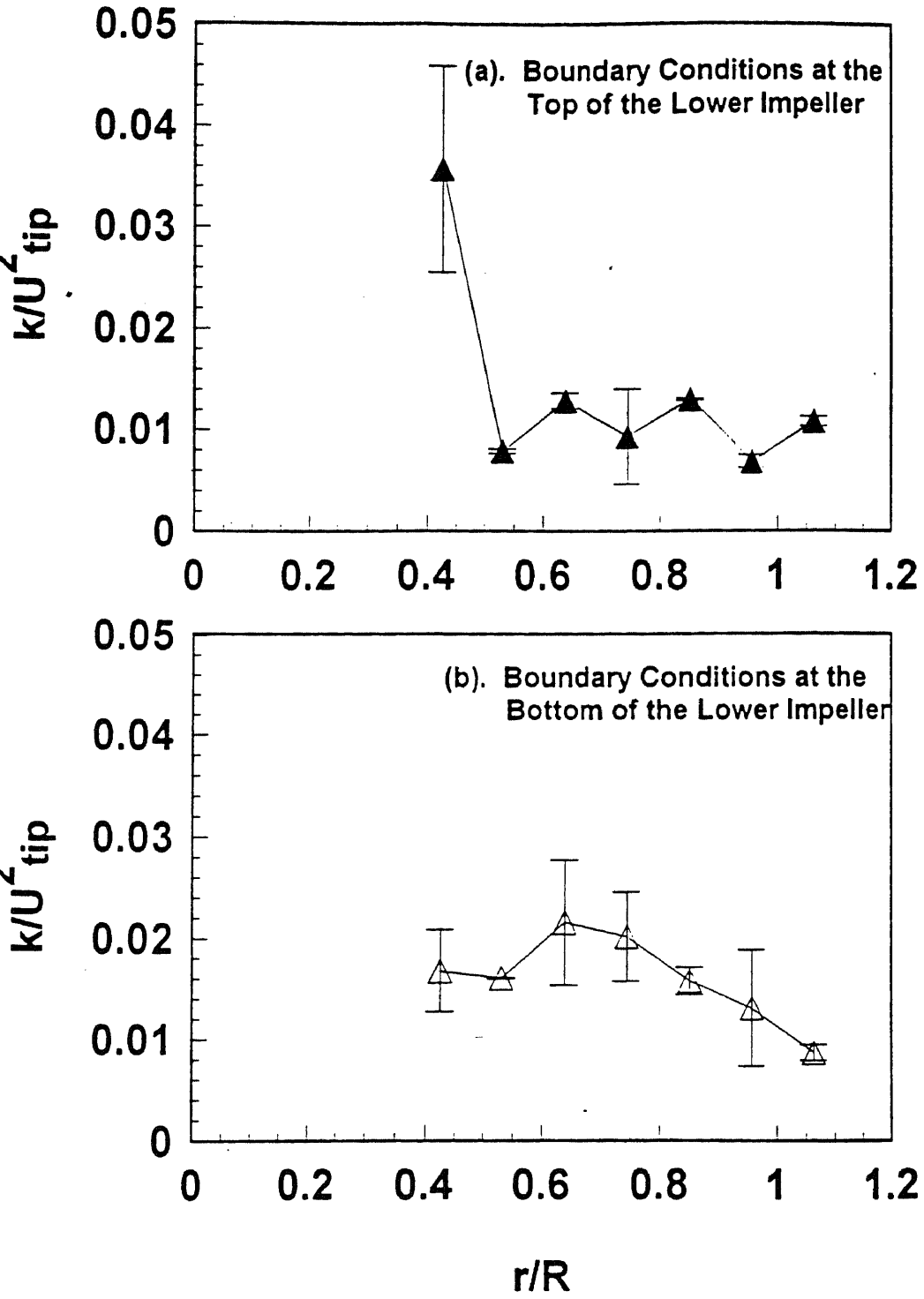

Figure 5-56. Turbulent kinetic energies in the impeller region. These values were used as the boundary conditions in the numerical CFD simulation. Double FBTs system: (a) boundary conditions at the top of the lower impeller; (b) boundary conditions at the bottom of the lower impeller. Error bars indicate standard deviation of duplicate experiments.

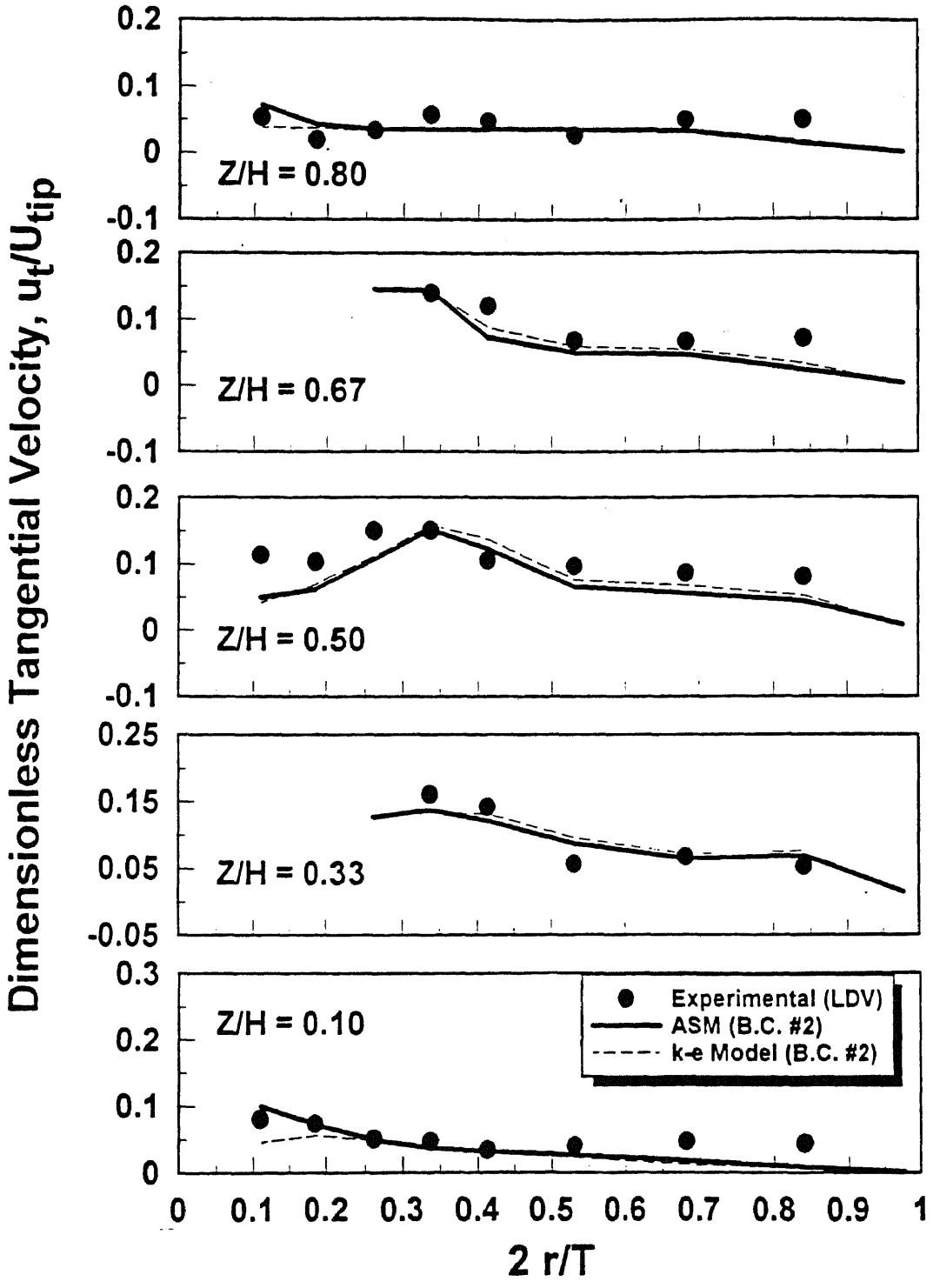

Figure 5-57. Comparison between experimental measurements and numerical predictions of the tangential velocities in double FBTs system.

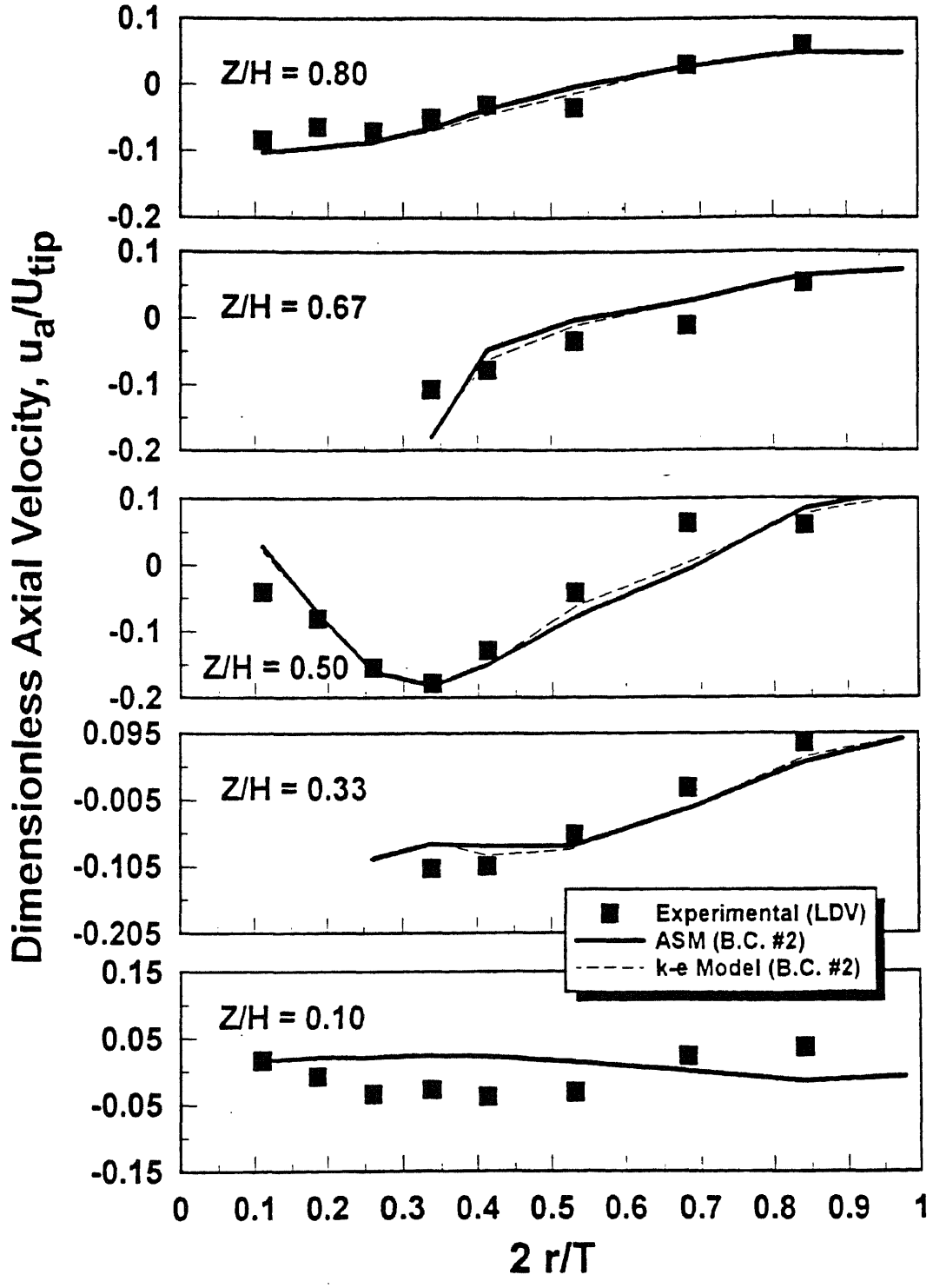

Figure 5-58. Comparison between experimental measurements and numerical predictions of the axial velocities in double FBTs system.

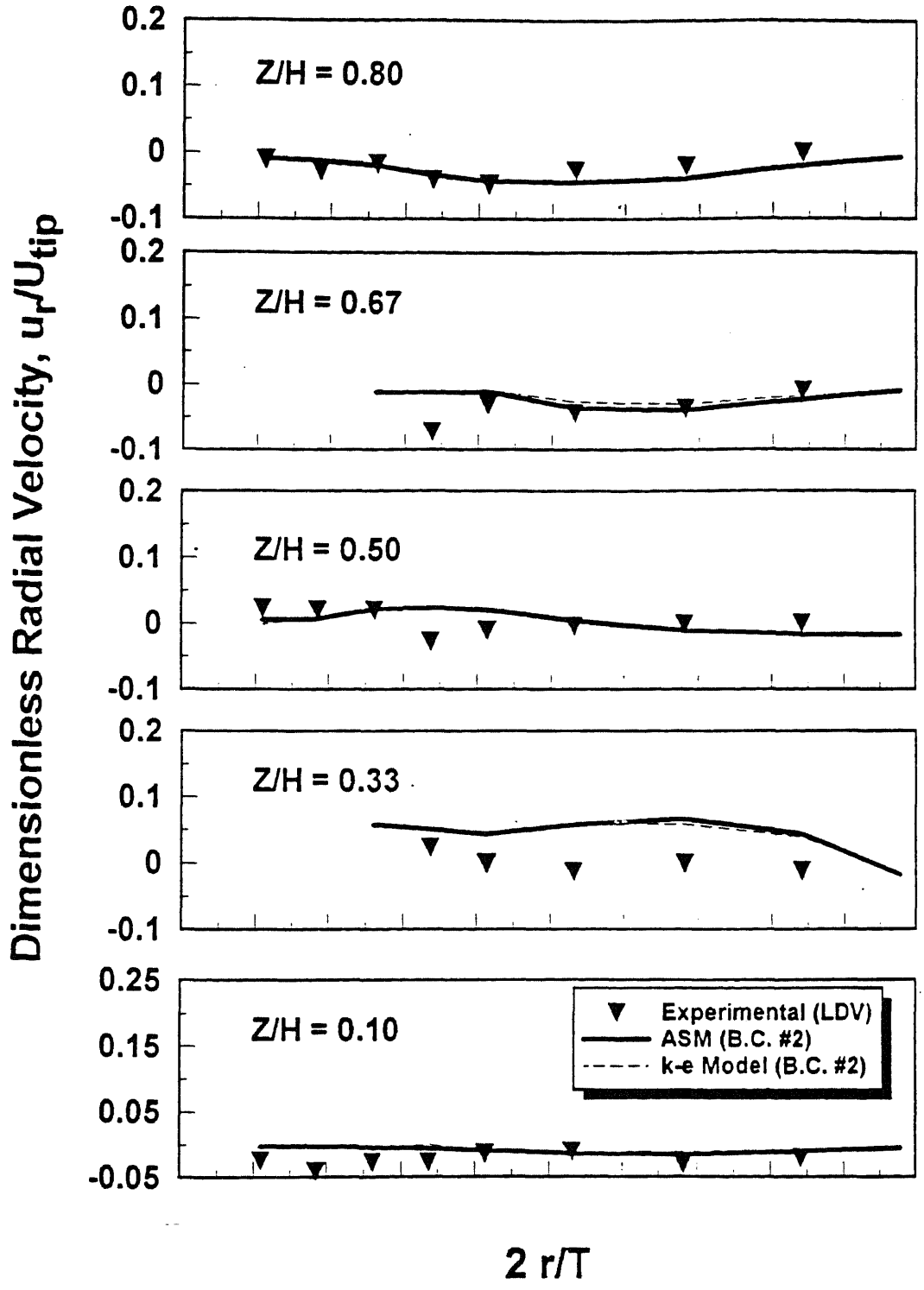

Figure 5-59. Comparison between experimental measurements and numerical predictions of the radial velocities in double FBTs system.

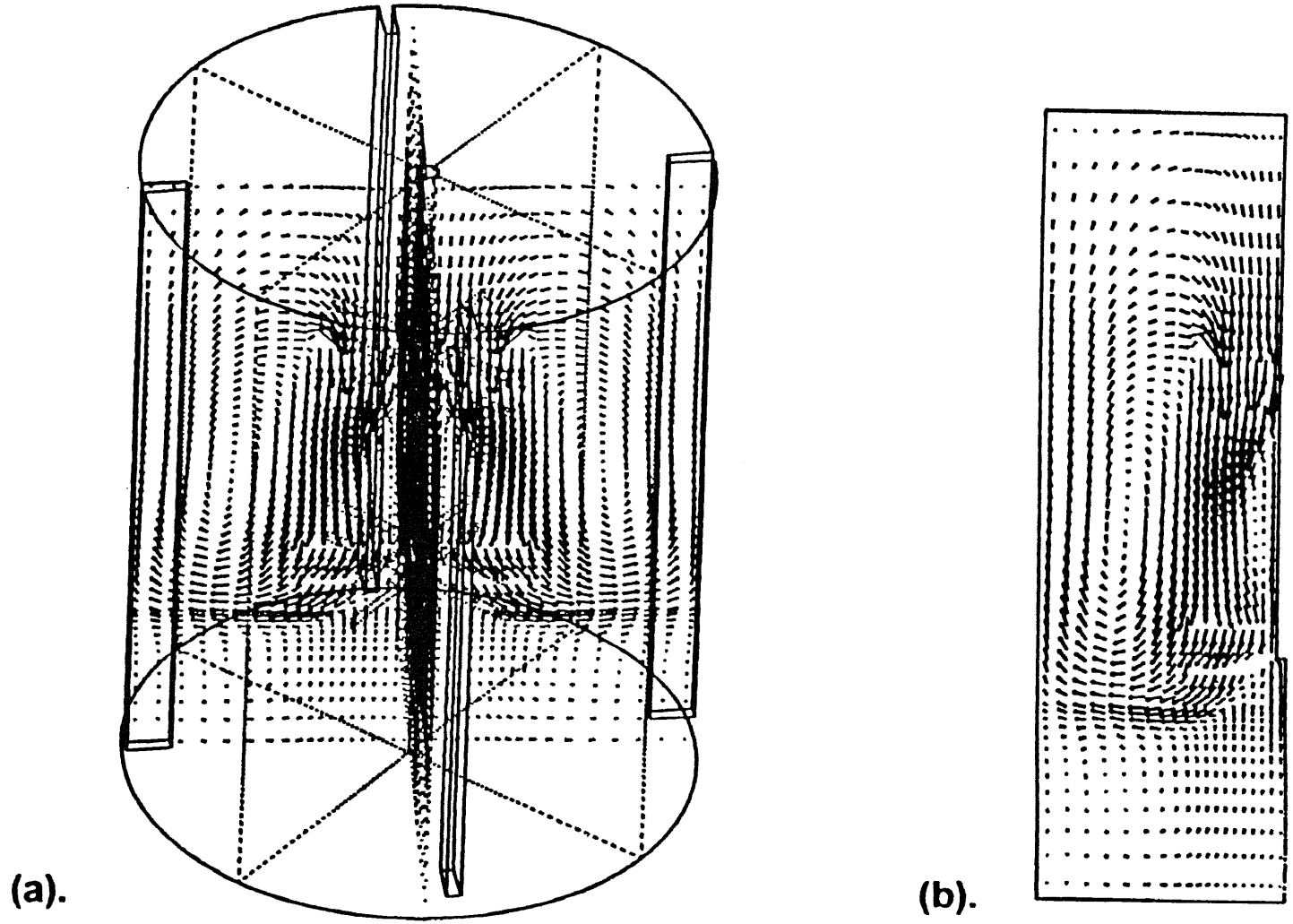

Figure 5-60. CFD prediction of velocity distribution in the vessel. System: baffled 2FBT. boundary conditions: B.C. #2. Turbulence model: ASM. (a) Tridimensional view; (b) Bidimensional cross section across the impeller shaft (only one half section shown).

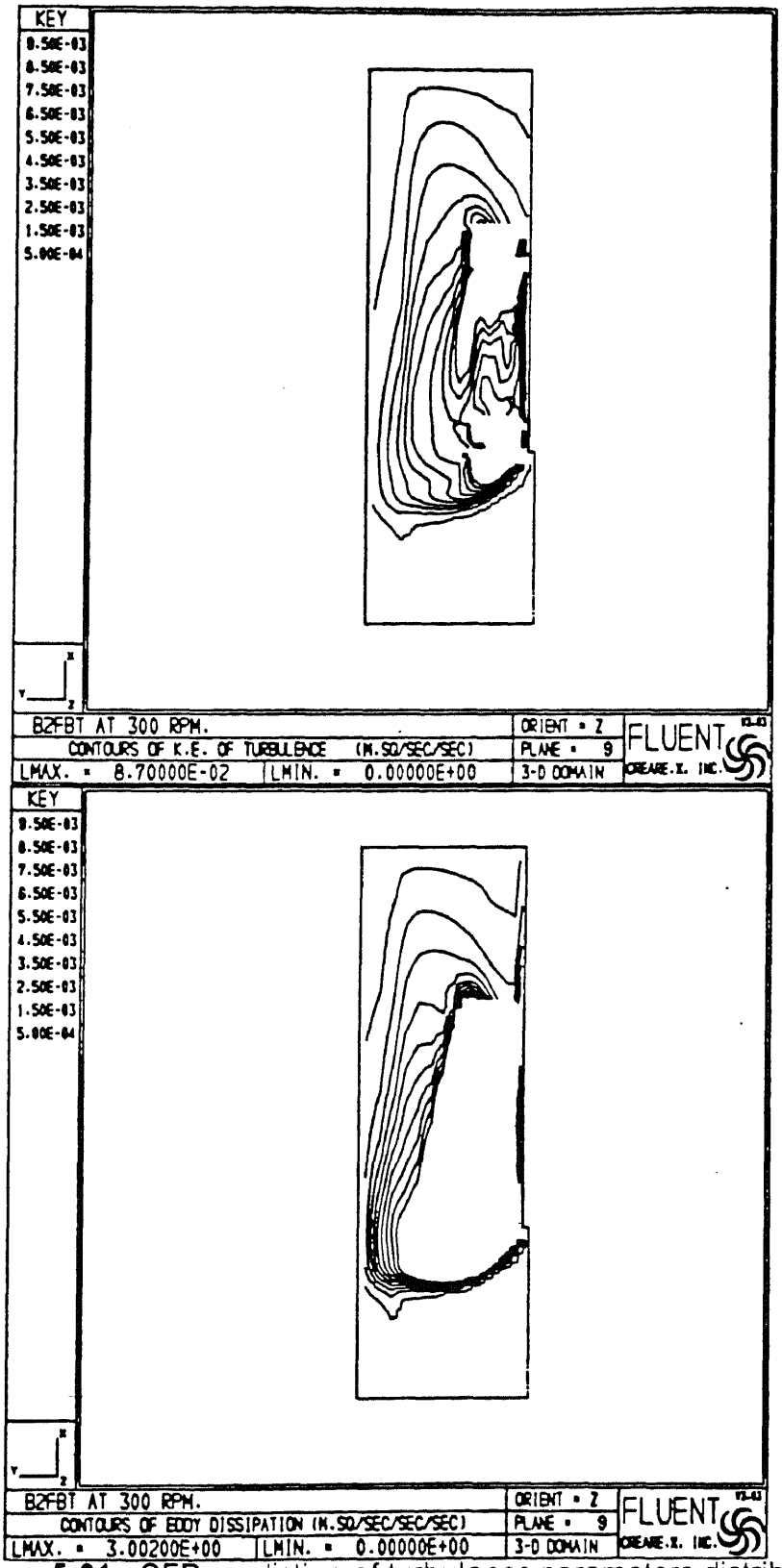

Figure 5-61. CFD prediction of turbulence parameters distribution in the vessel. System: baffled 2FBT. Contours for (a) turbulence kinetic energy; (b) dissipation rate.

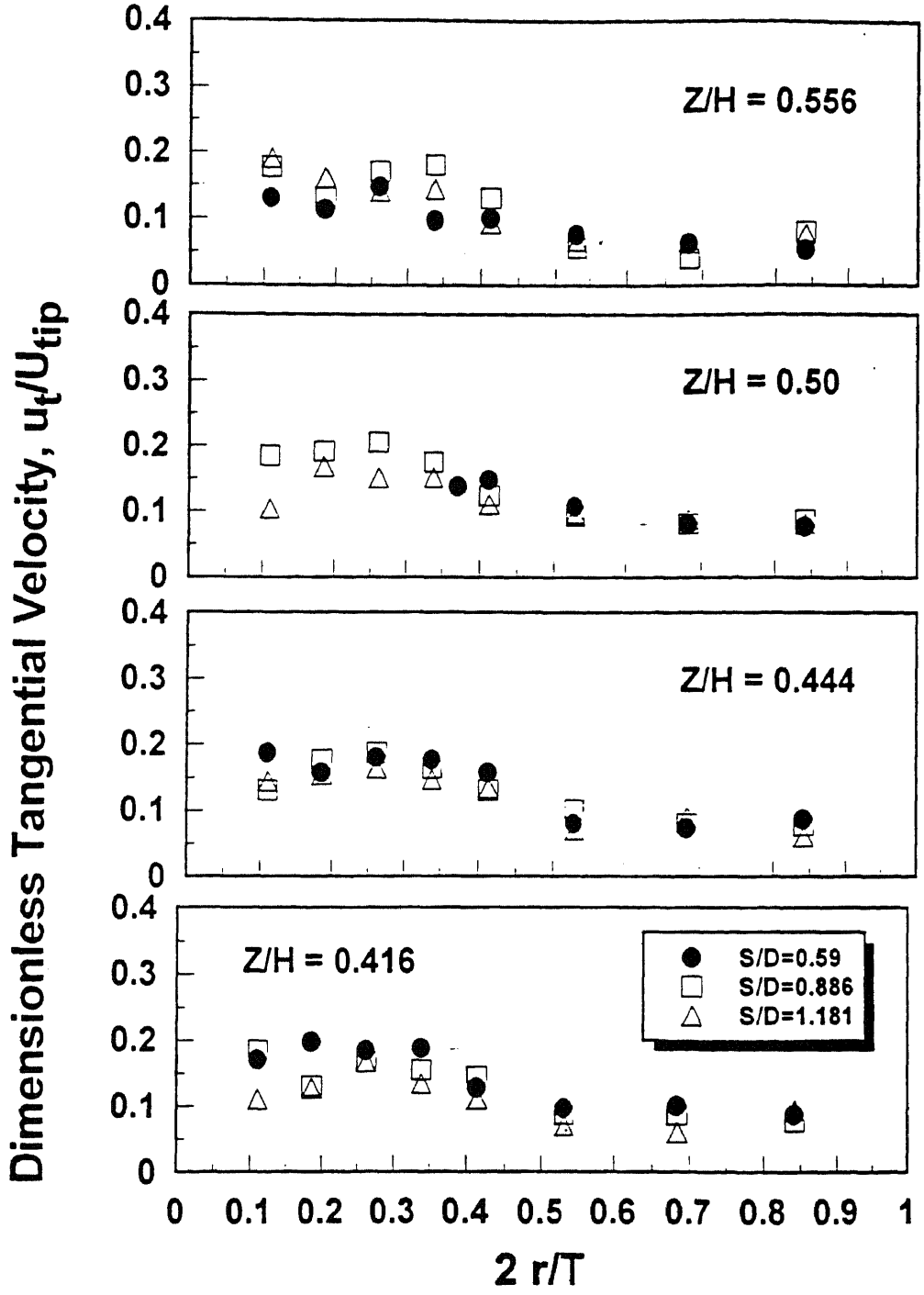

Figure 5-62. LDV measurements of the dimensionless tangential velocities along the dimensionless tank radius at impeller spacing (S/D) equal to 0.59, 0.886, and 1.181 for (Z/H) at 0.416, 0.444, 0.50, and 0.556 of the B2FBT system.

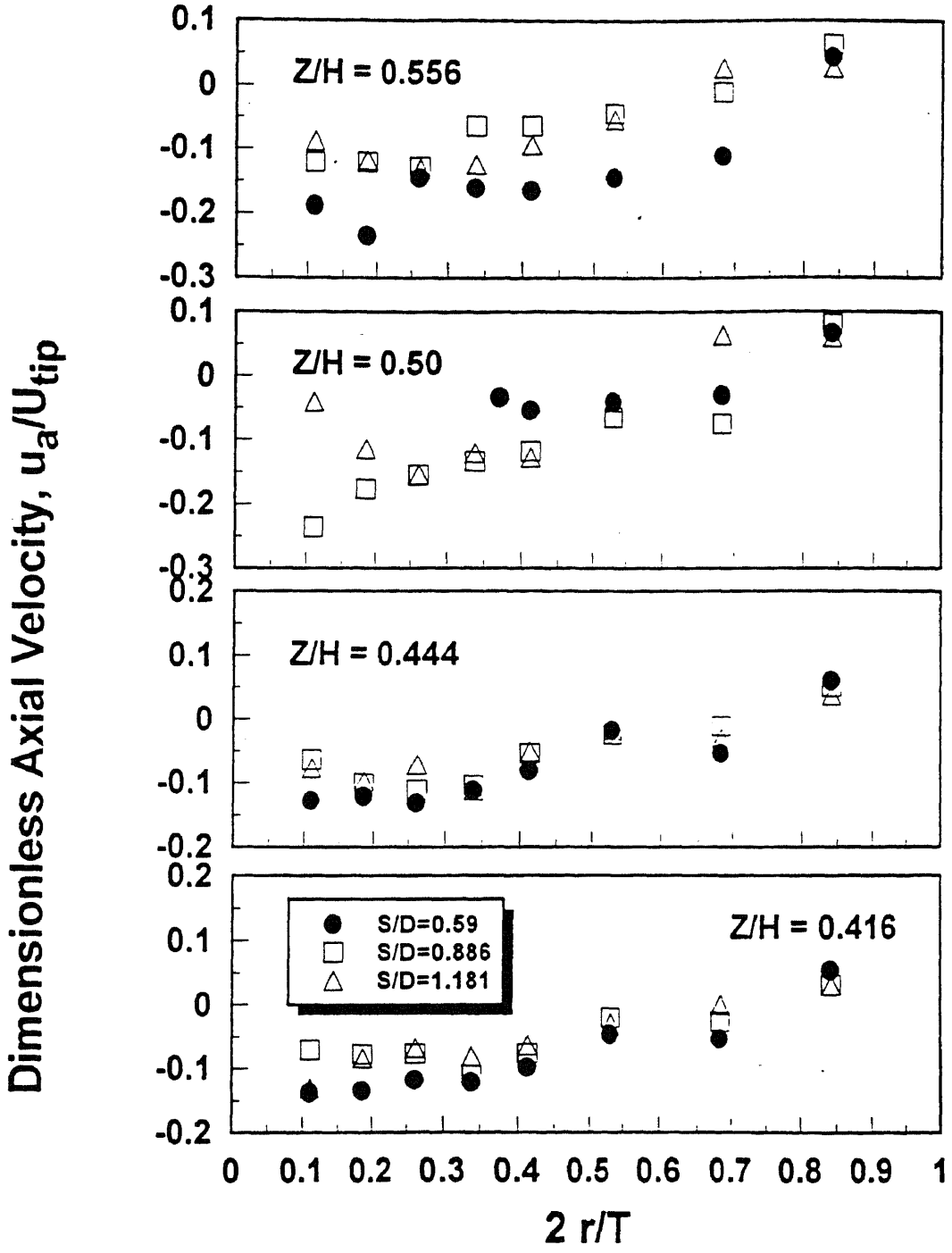

Figure 5-63. LDV measurements of the dimensionless axial velocities along the dimensionless tank radius at impeller spacing (S/D) equal to 0.59, 0.886, and 1.181 for (Z/H) at 0.416, 0.444, 0.50, and 0.556 of the B2FBT system.

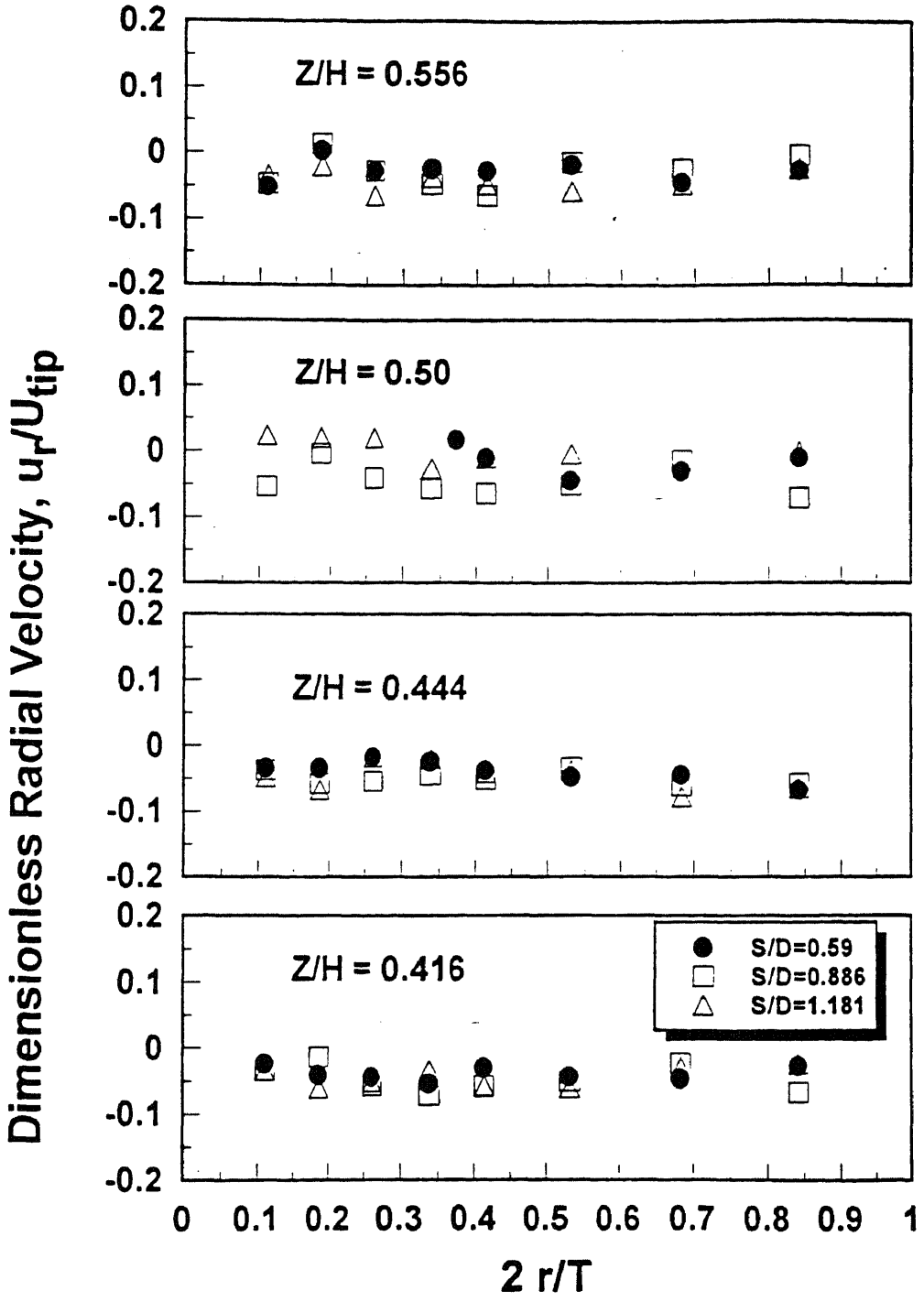

Figure 5-64. LDV measurements of the dimensionless radial velocities along the dimensionless tank radius at impeller spacing (S/D) equal to 0.59, 0.886,and 1.181 for (Z/H) at 0.416, 0.444, 0.50, and 0.556 of the B2FBT system.

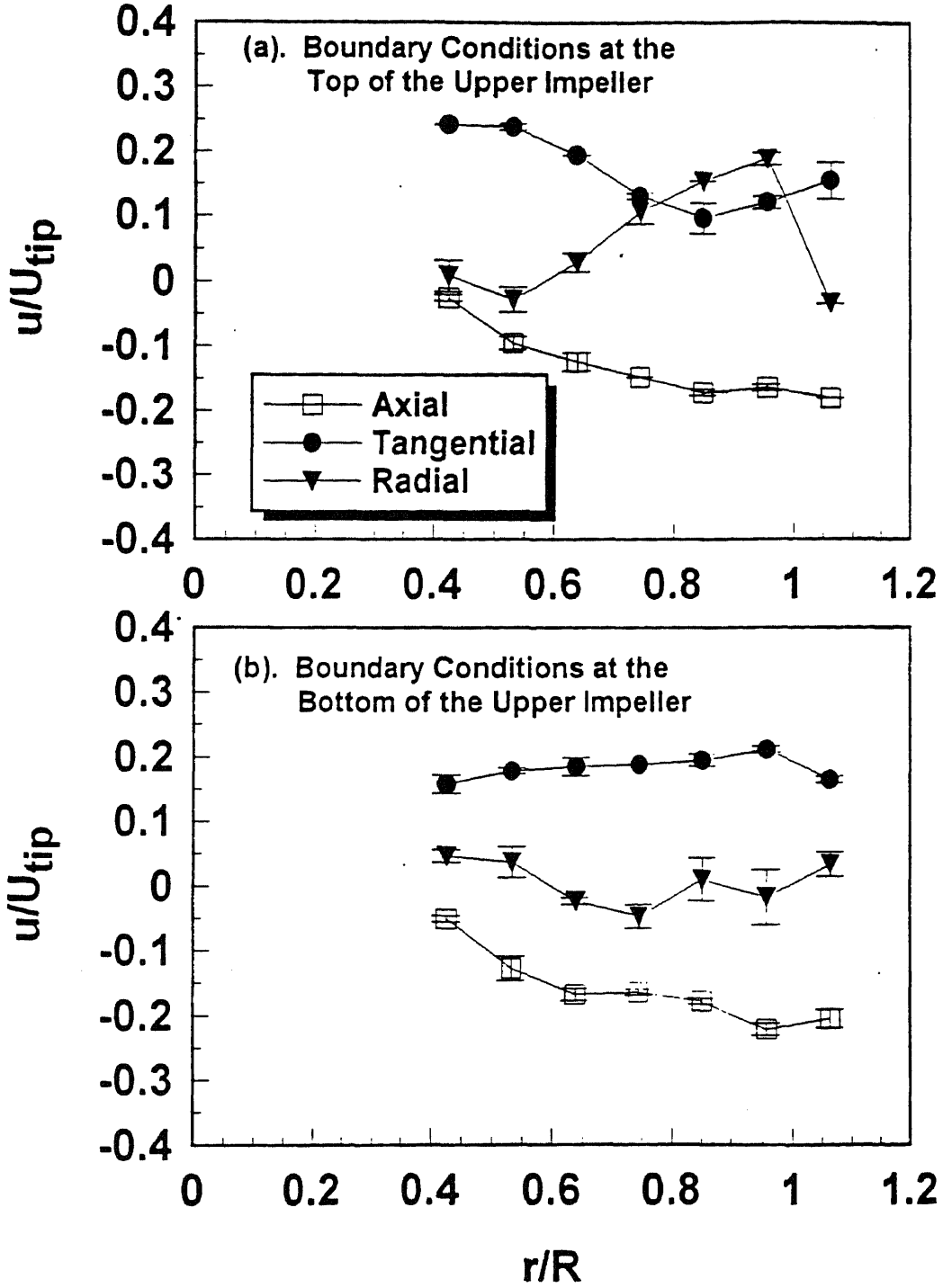

Figure 5-65. Experimentally determined (via LDV) velocities in the impeller region. These values were used as the boundary conditions in the numerical CFD simulation. Baffled PFBT system: (a) boundary conditions at the top of the upper impeller; (b) boundary conditions at the bottom of the upper impeller. Positive values indicate upwards velocities (for the axial direction). Error bars indicate standard deviation of duplicate experiments.

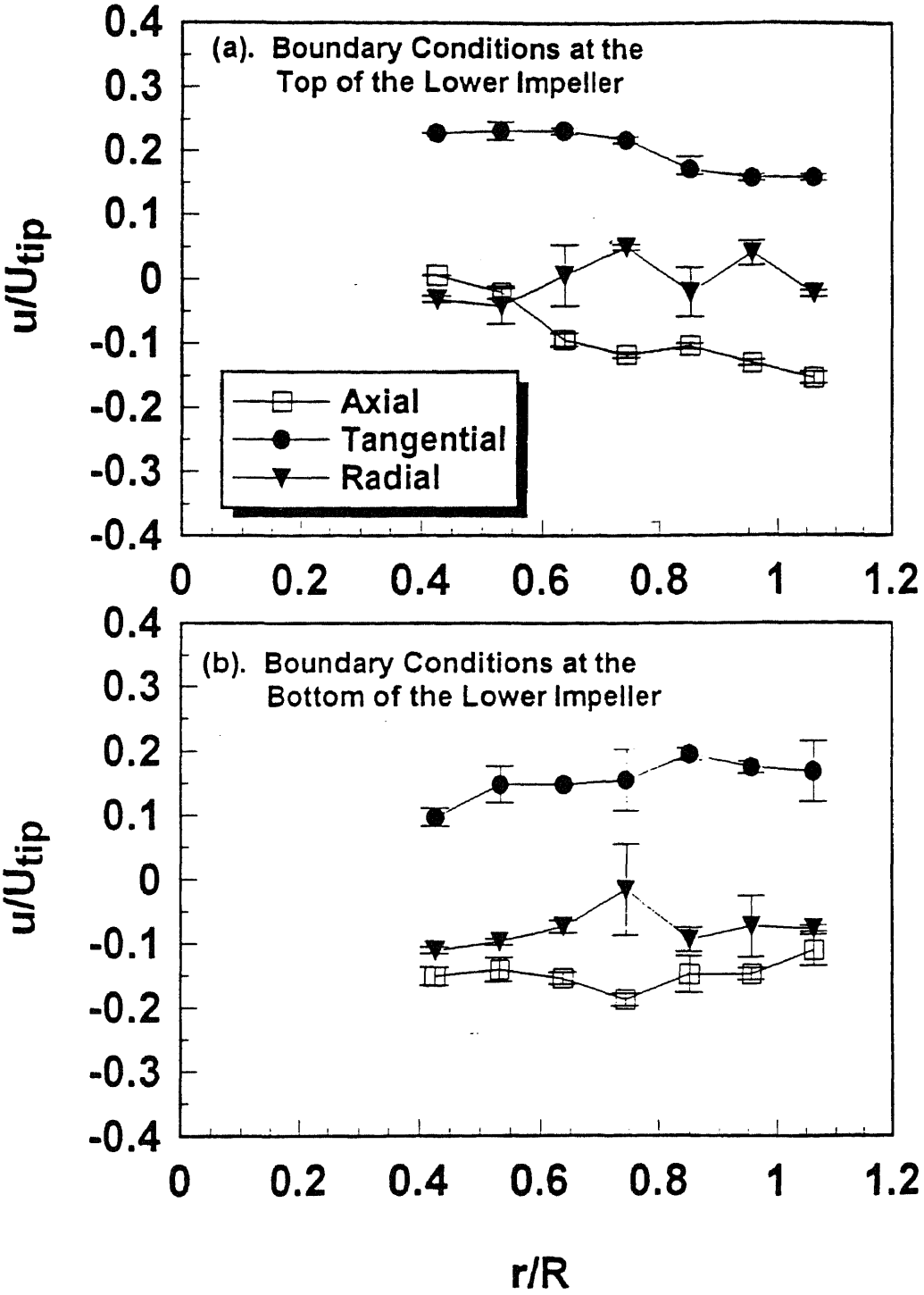

Figure 5-66. Experimentally determined (via LDV) velocities in the impeller region. These values were used as the boundary conditions in the numerical CFD simulation. Baffled PFBT system: (a) boundary conditions at the top of the lower impeller; (b) boundary conditions at the bottom of the lower impeller. Positive values indicate upwards velocities (for the axial direction). Error bars indicate standard deviation of duplicate experiments.

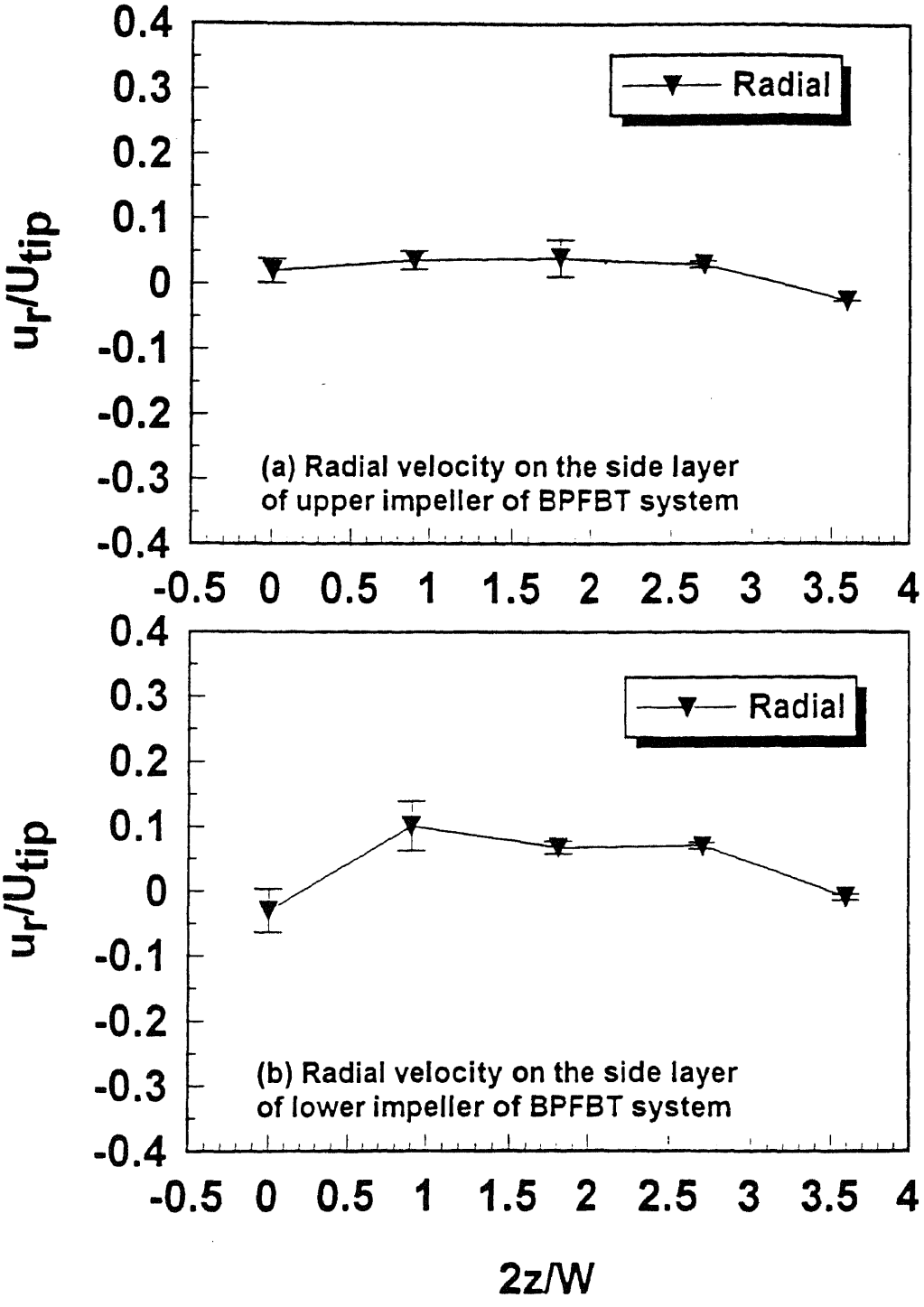

Figure 5-67. Experimentally determined (via LDV) radial velocities on the side layer of the impeller region. BPFBT system: (a) upper impeller; (b) lower impeller. Negative value indicate outwards direction from impeller. Error bars indicate standard deviation of duplicate experiments.

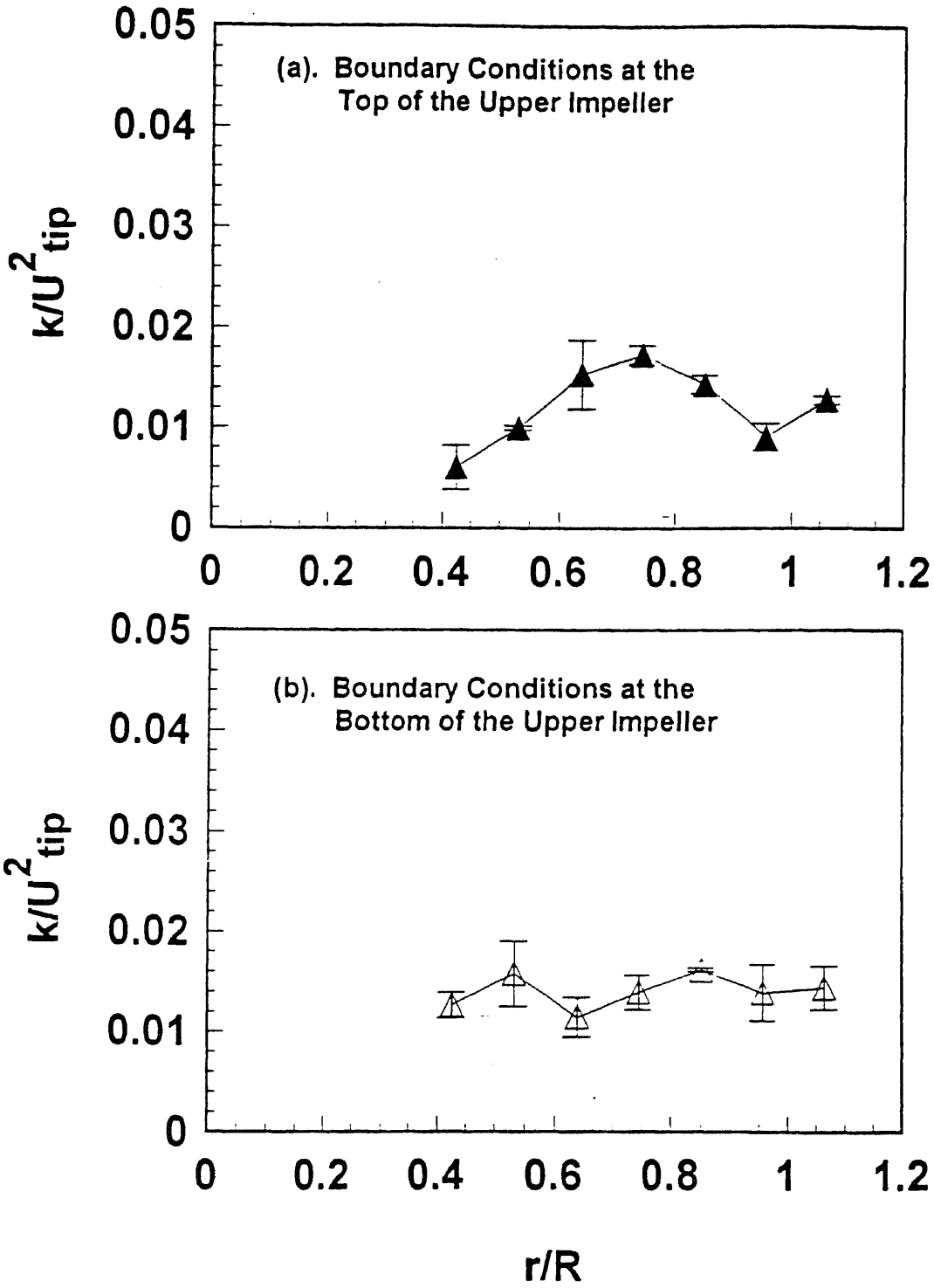

Figure 5-68. Turbulent kinetic energies in the impeller region. These values were used as the boundary conditions in the numerical CFD simulation. Baffled PFBT system: (a) boundary conditions at the top of the upper impeller; (b) boundary conditions at the bottom of the upper impeller. Error bars indicate standard deviation of duplicate experiments.

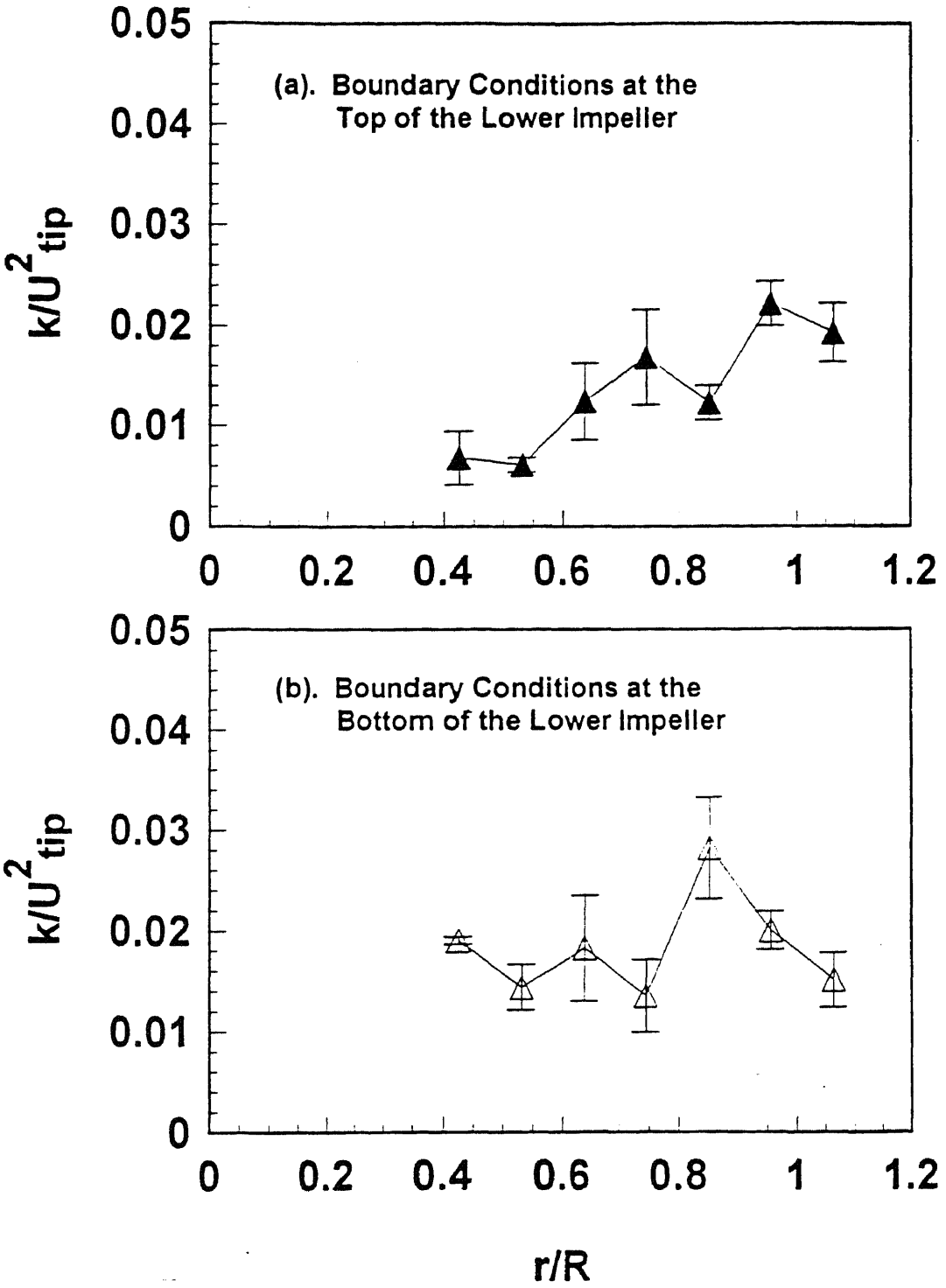

Figure 5-69. Turbulent kinetic energies in the impeller region. These values were used as the boundary conditions in the numerical CFD simulation. Baffled PFBT system: (a) boundary conditions at the top of the lower impeller; (b) boundary conditions at the bottom of the lower impeller. Error bars indicate standard deviation of duplicate experiments.

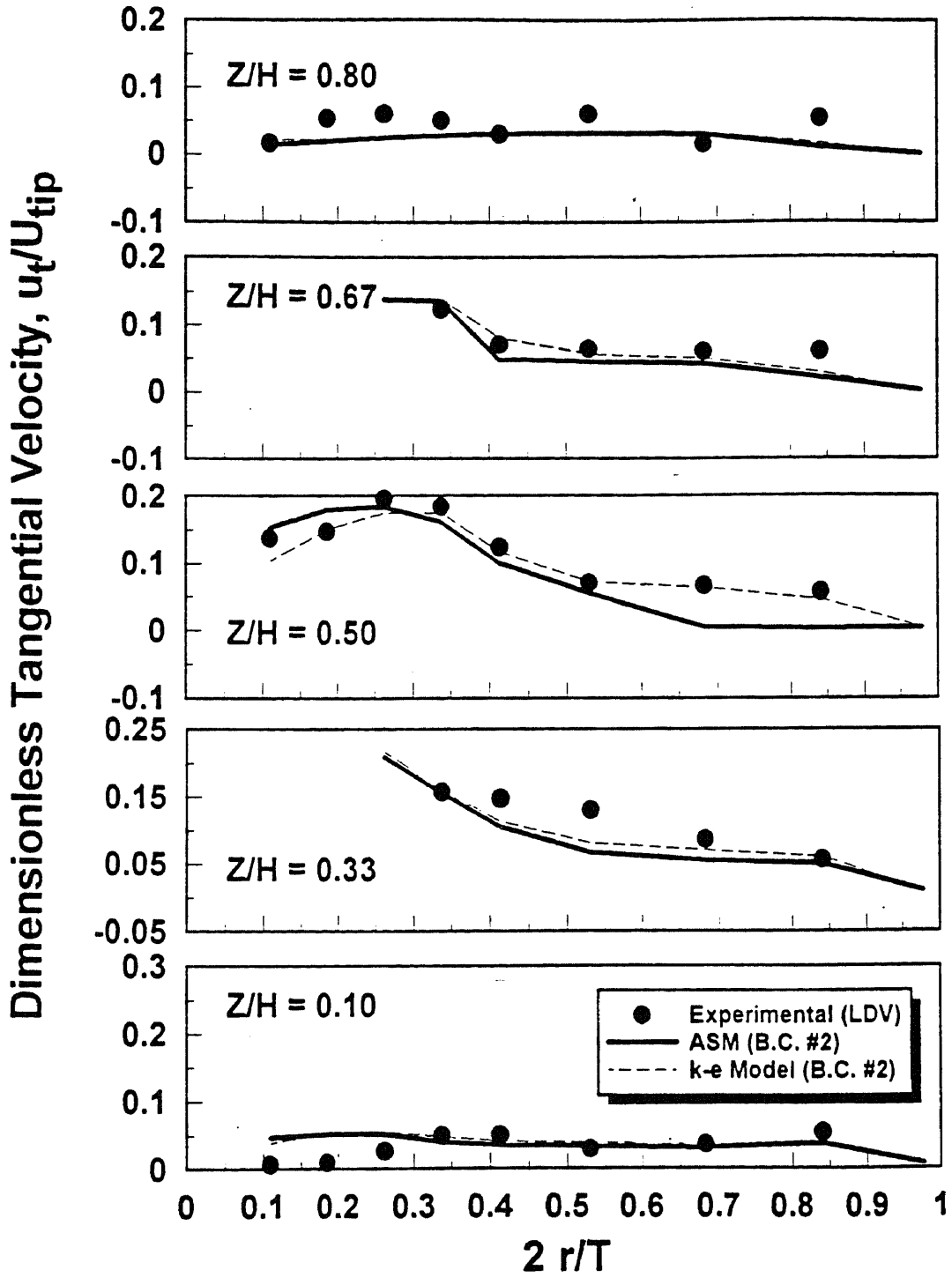

Figure 5-70. Comparison between experimental measurements and numerical predictions of the tangential velocities in baffled PFBT system.

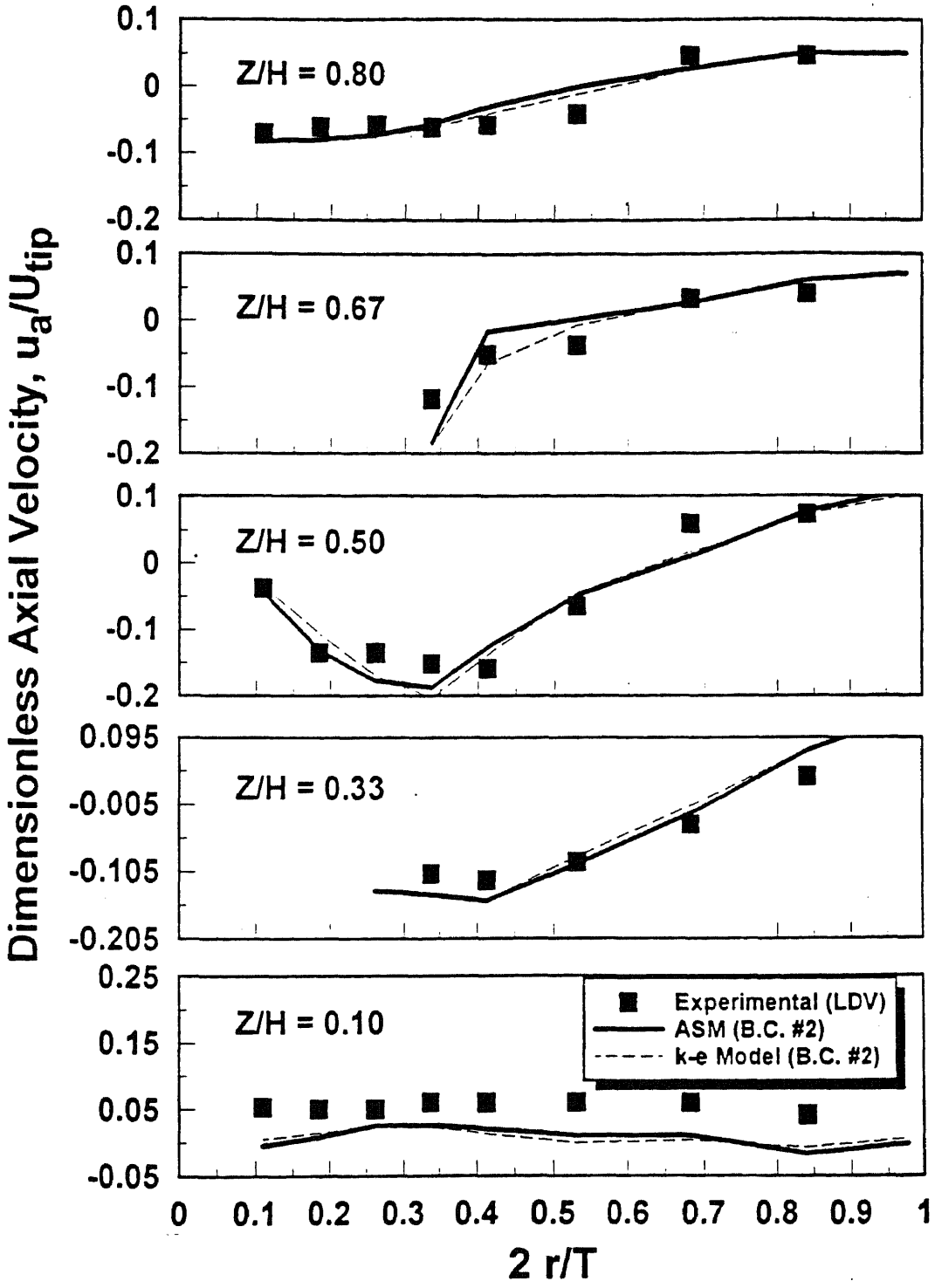

Figure 5-71. Comparison between experimental measurements and numerical predictions of the axial velocities in baffled PFBT system.

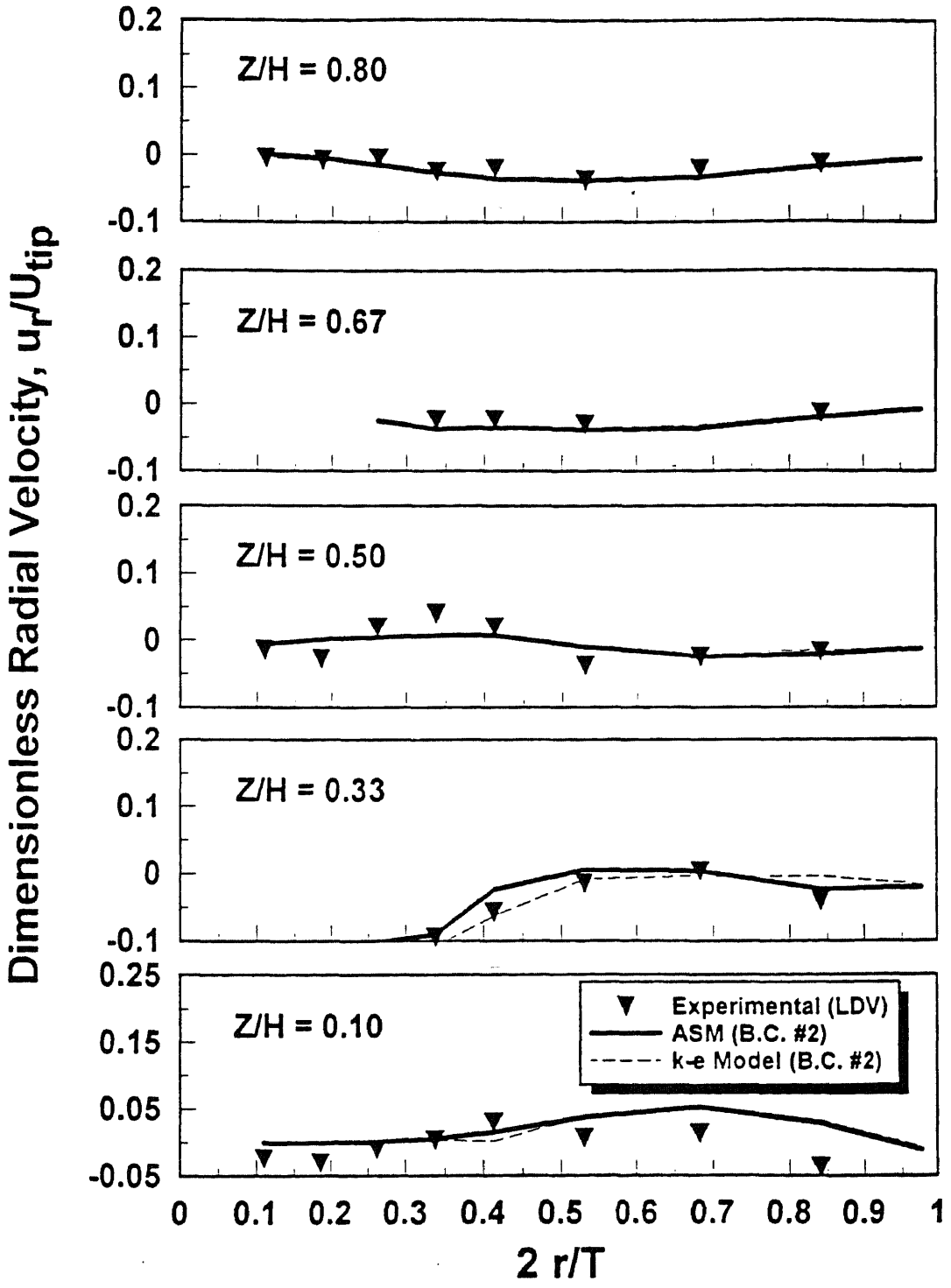

Figure 5-72. Comparison between experimental measurements and numerical predictions of the radial velocities in baffled PFBT system.

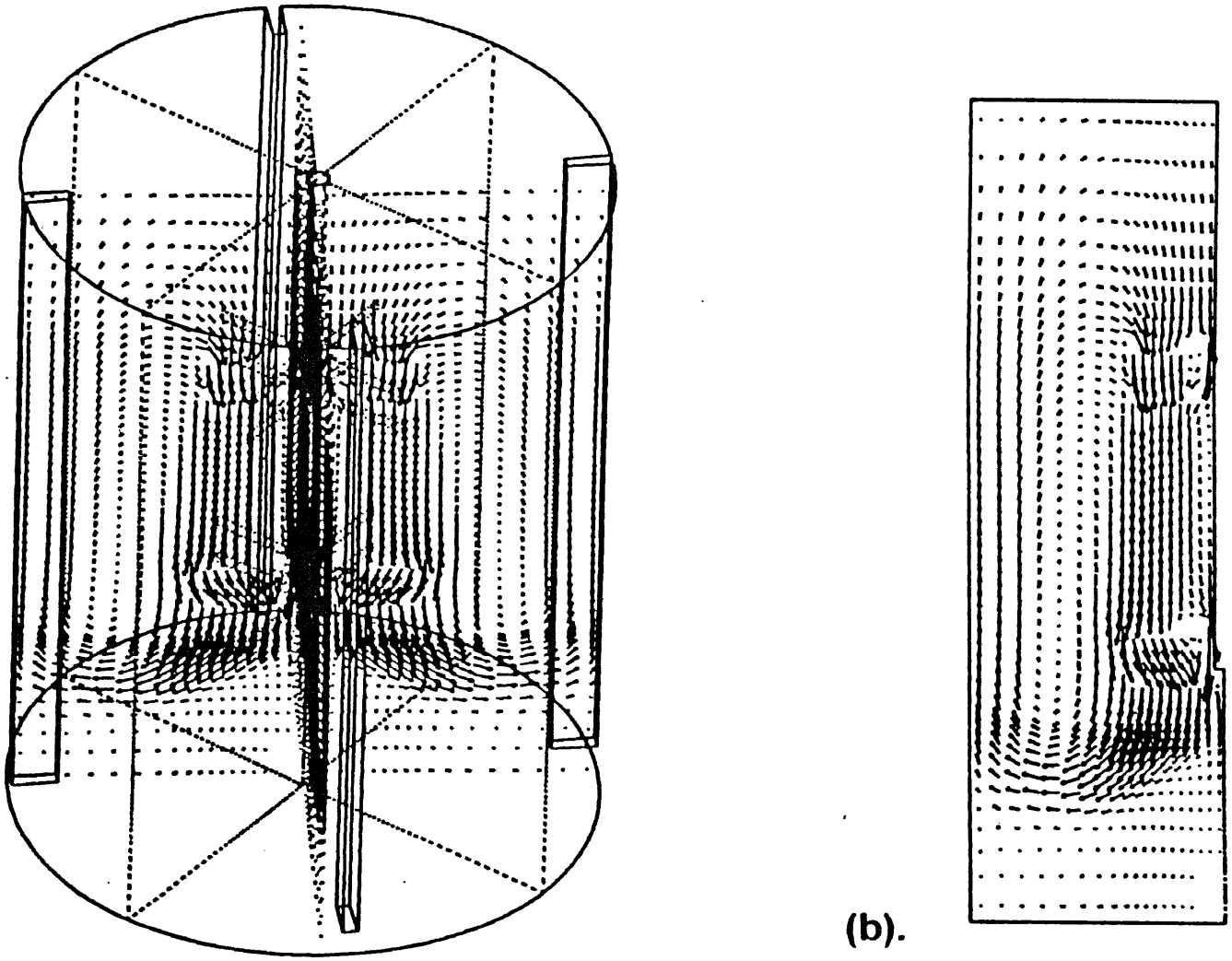

Figure 5-73. CFD prediction of velocity distribution in the vessel. System: baffled PFBT. boundary conditions: B.C. #2. Turbulence model: ASM. (a) Tridimensional view; (b) Bidimensional cross section across the impeller shaft (only one half section shown).

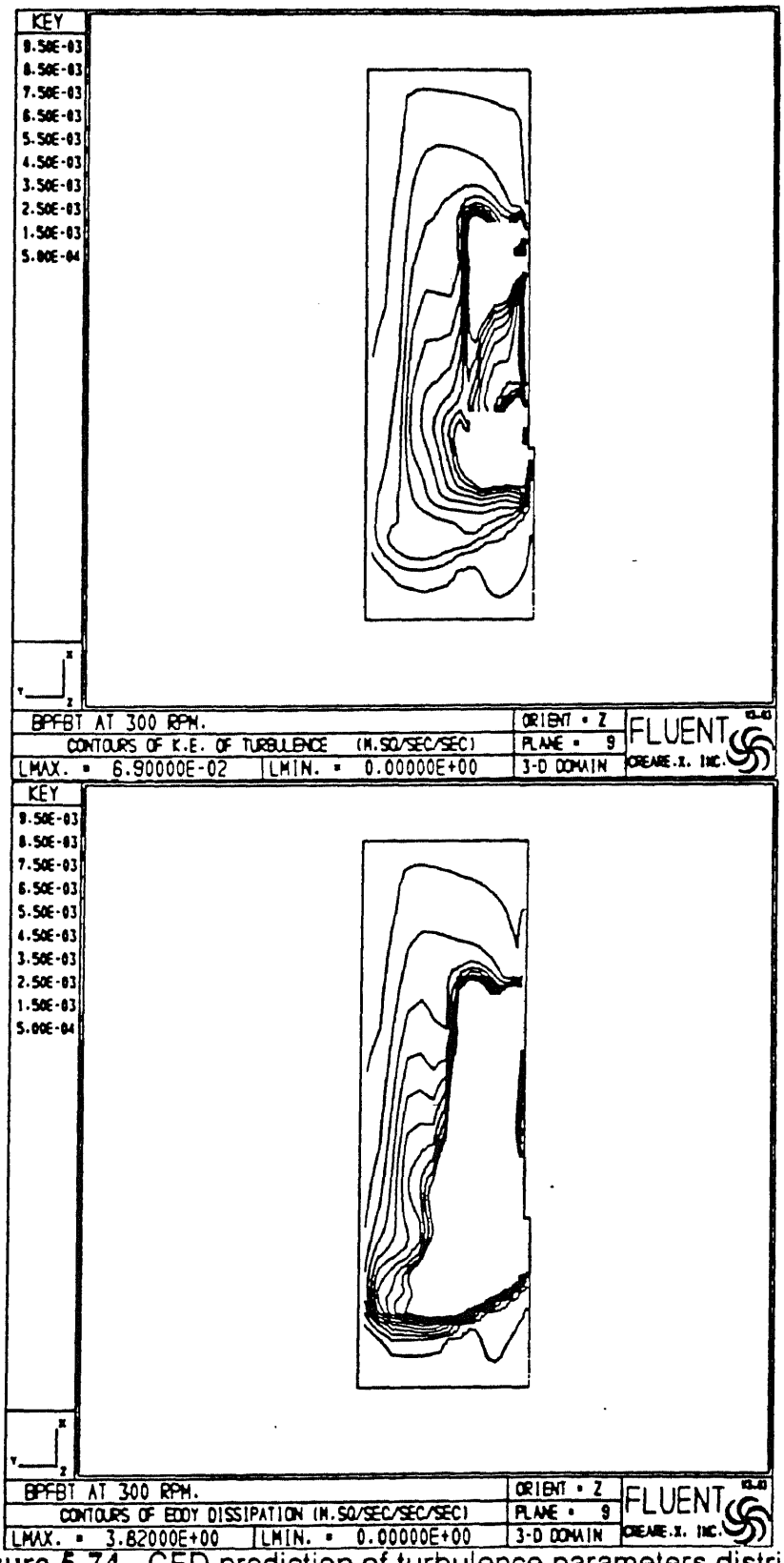

Figure 5-74. CFD prediction of turbulence parameters distribution in the vessel. System: baffled PFBT. Contours for (a) turbulence kinetic energy; (b) dissipation rate.

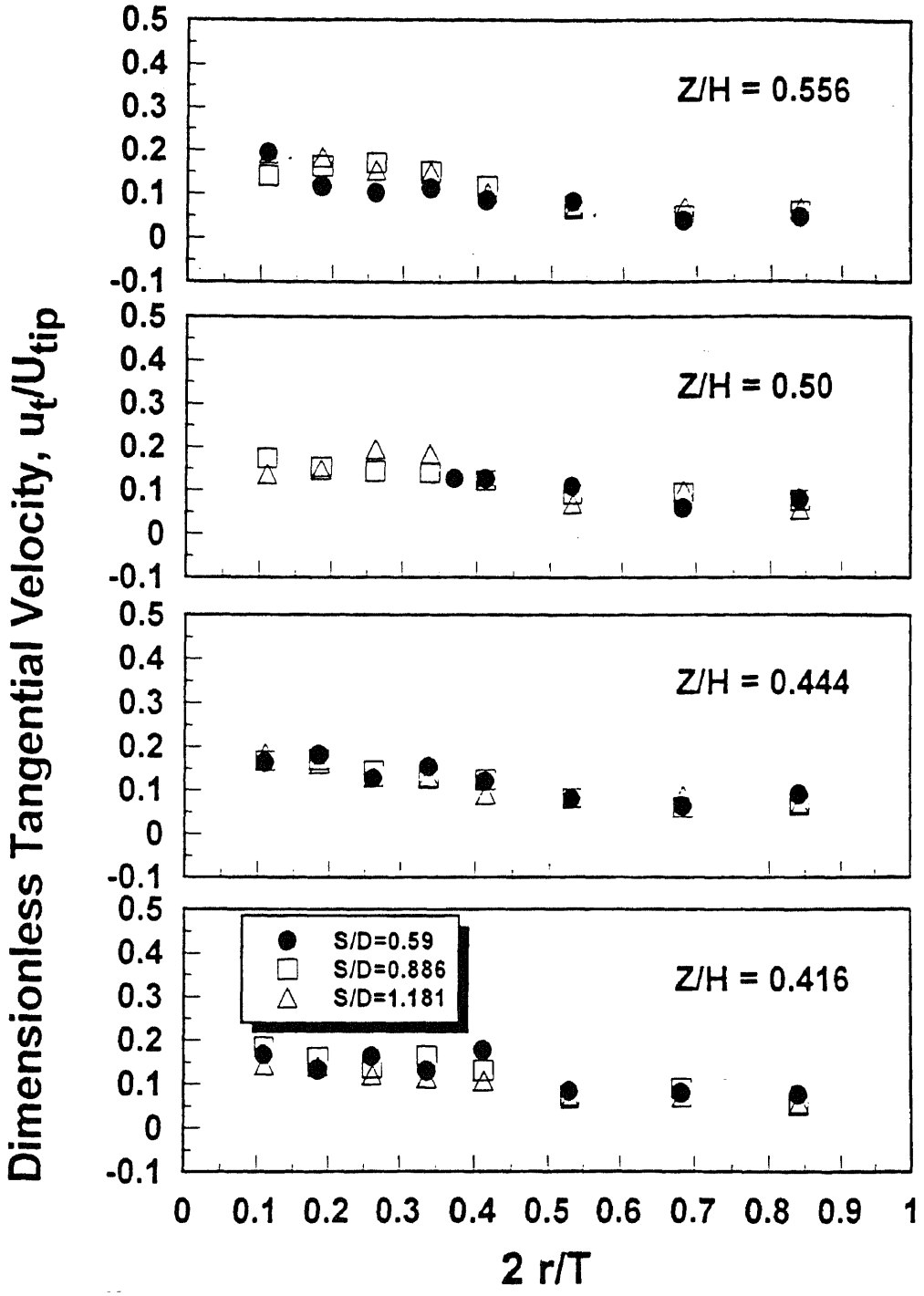

Figure 5-75. LDV measurements of the dimensionless tangential velocities along the dimensionless tank radius at impeller spacing (S/D) equal to 0.59, 0.886, and 1.181 for (Z/H) at 0.416, 0.444, 0.50, and 0.556 of the BPFBT system.

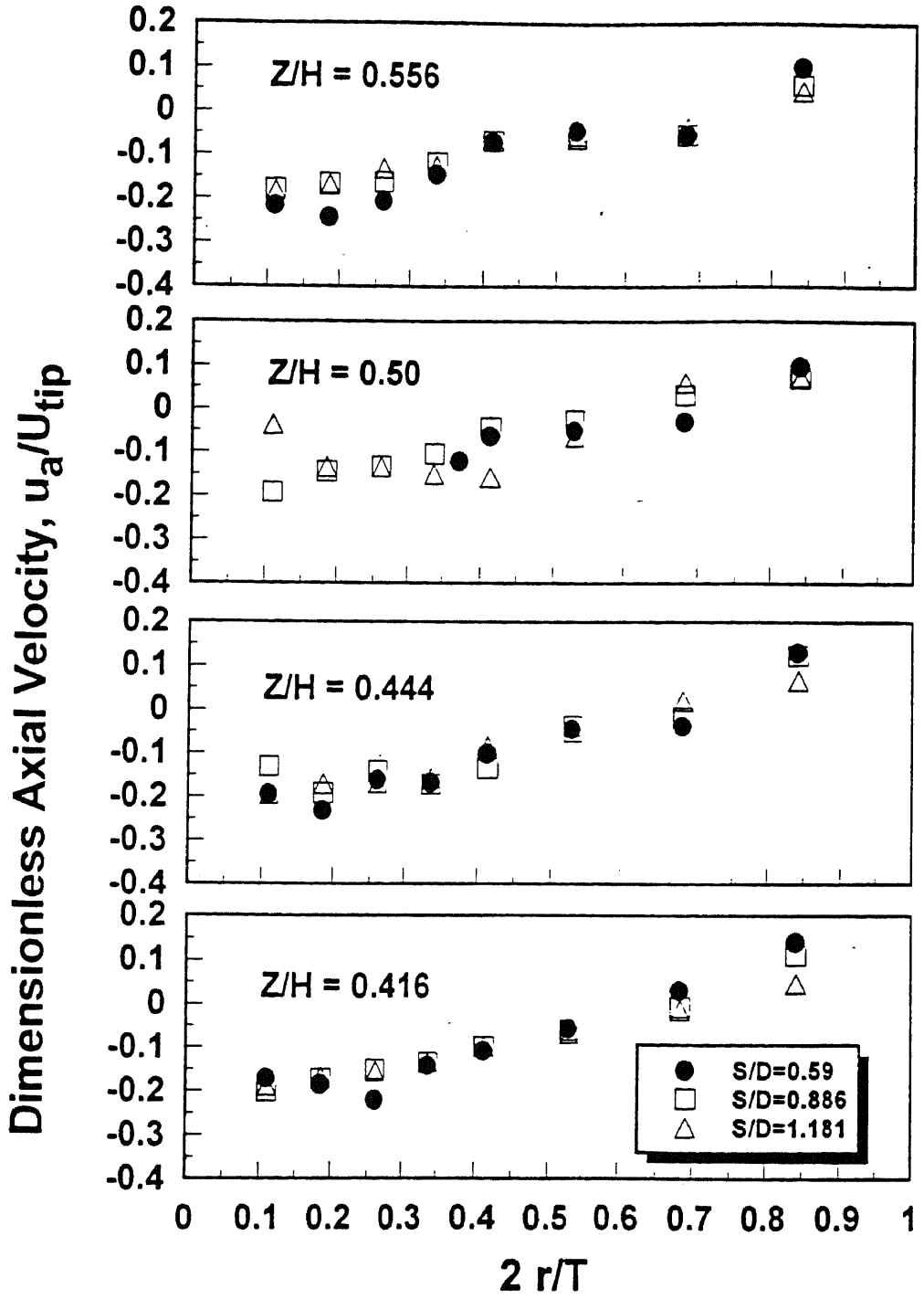

Figure 5-76. LDV measurements of the dimensionless axial velocities along the dimensionless tank radius at impeller spacing (S/D) equal to 0.59, 0.886, and 1.181 for (Z/H) at 0.416, 0.444, 0.50, and 0.556 of the BPFBT system.

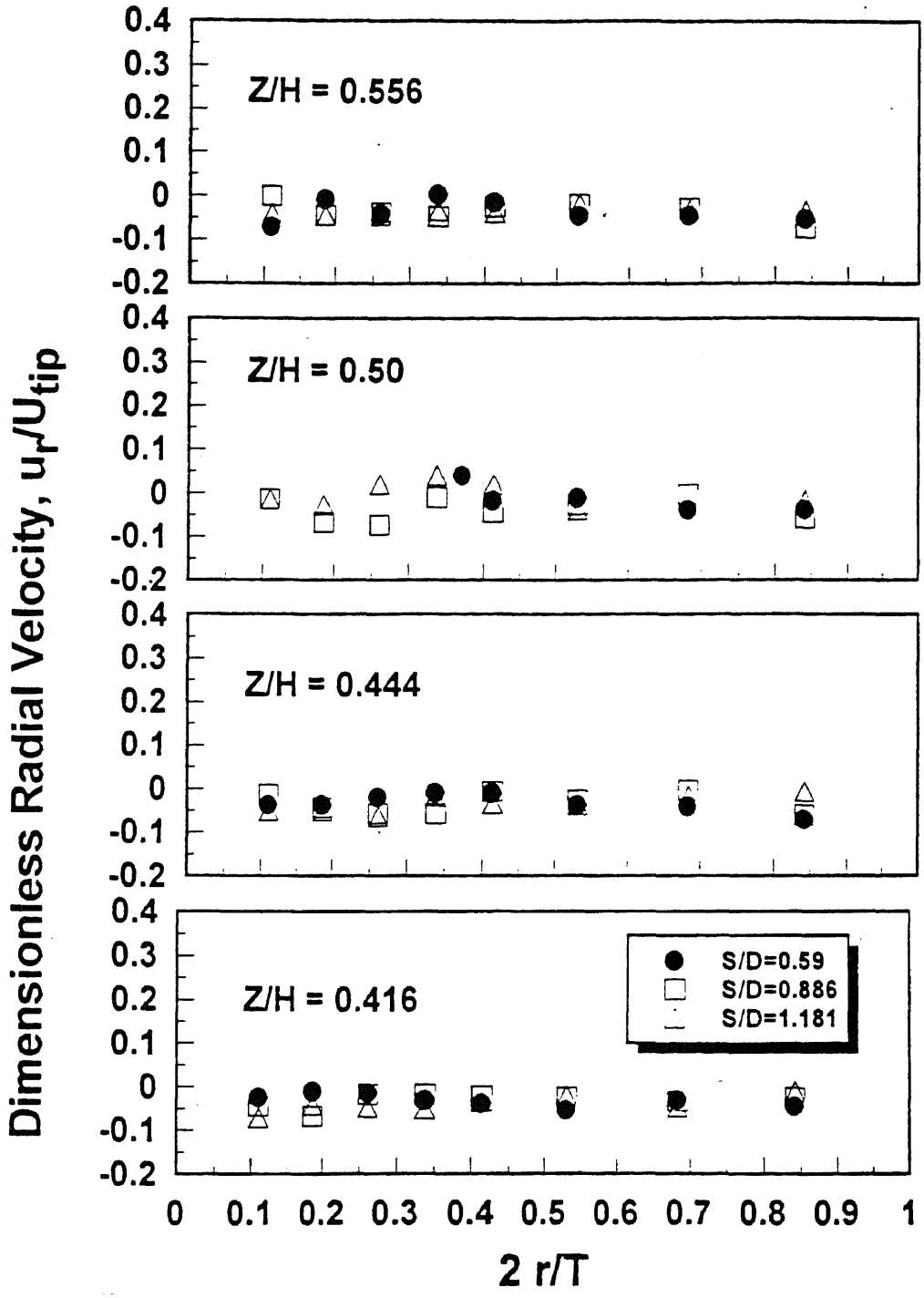

Figure 5-77. LDV measurements of the dimensionless radial velocities along the dimensionless tank radius at impeller spacing (S/D) equal to 0.59, 0.886, and 1.181 for (Z/H) at 0.416, 0.444, 0.50, and 0.556 of the BPFBT system.

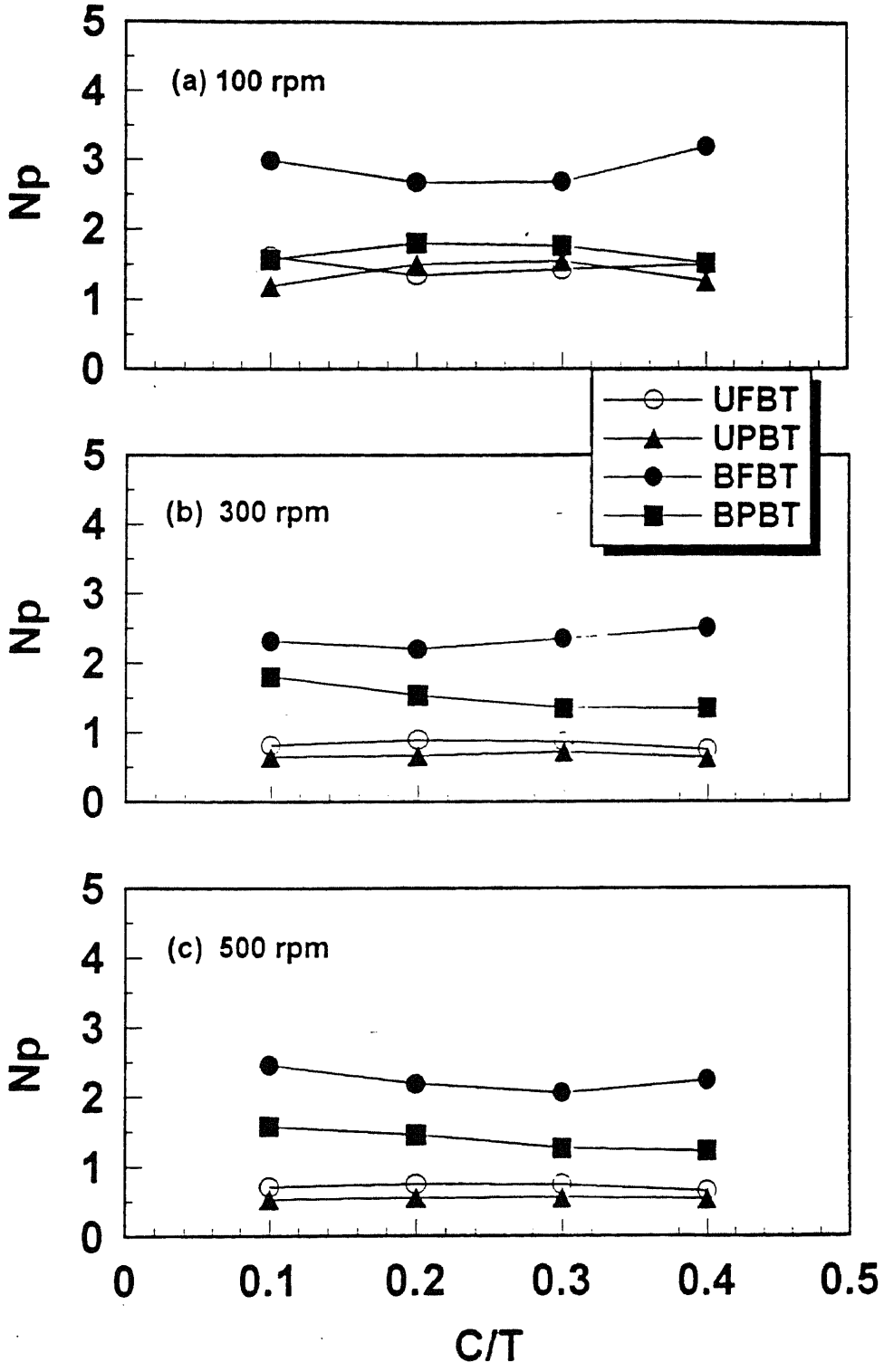

Figure 5-78. Power number (Np) versus impeller off bottom clearance ratio (C/T) at rpm equal to (a) 100, (b) 300, and (c) 500.

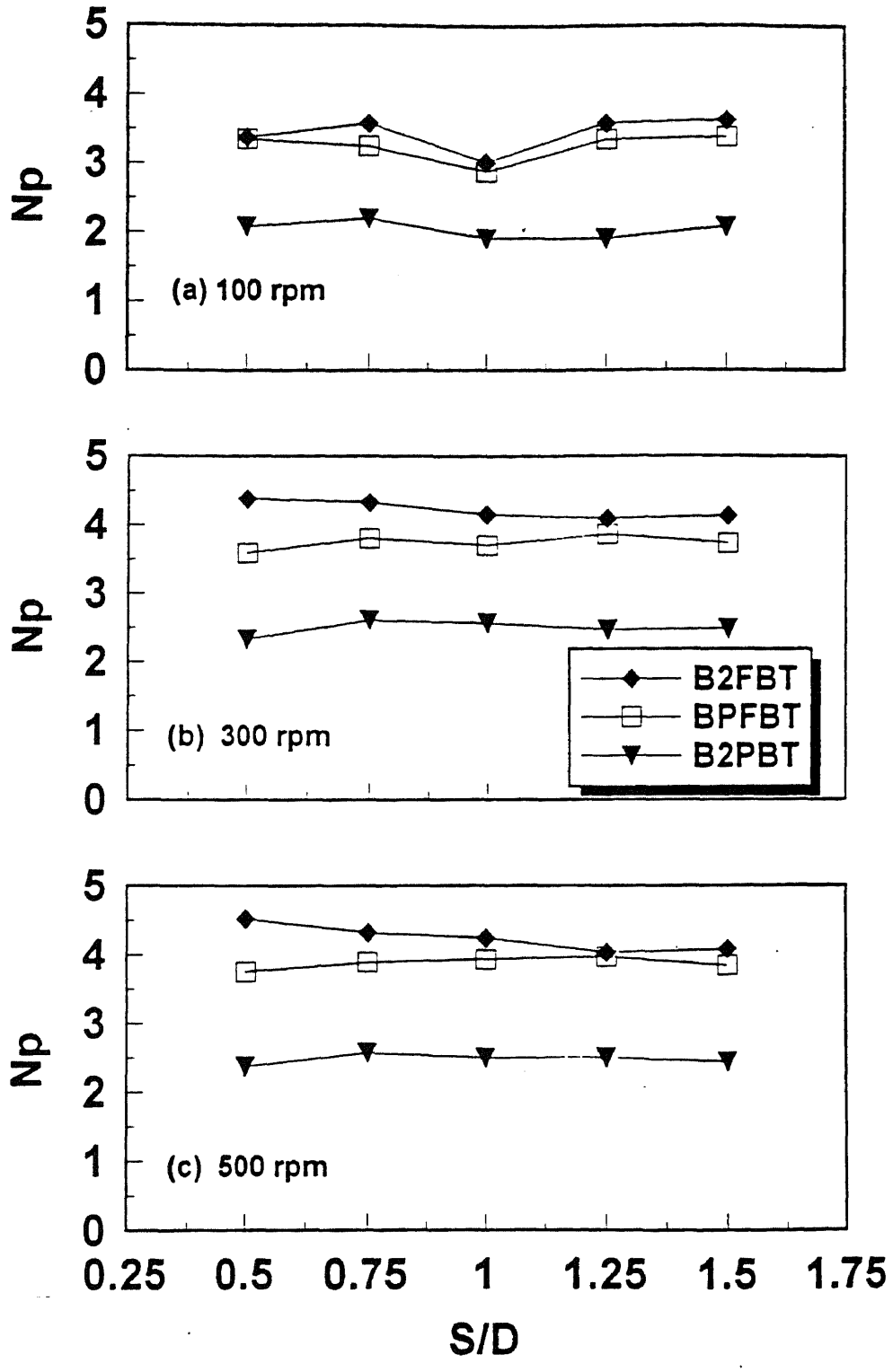

Figure 5-79. Power number (Np) versus impeller spacing (S/D) at rpm equal to (a) 100, (b) 300, and (c) 500.

APPENDIX B

SIMULATION PROGRAM SETUP FOR UNBAFFLED CONFIGURATION

This appendix contains the procedures for setting up the computer program of unbaffled configuration.

B.1 Stationary Reference Frame

Customize the length unit . Define domain size, number of cells, and activate turbulent flow.

```
s1 no
ex su
no
yes 3
centimeters
0.01
no
quit
dd num
53
26
17
done
ds yes
33.6
0
14.5
1.047197
done
dv
yes
c
done
quit
```

Generating a non-uniform grid

```
gg
yes 5
0.87 4.2232 8
1 10 19
1.15 17.4832 11
1
yes 5
1 1.2 3
1.18 4.0616 5
1 11.8166 10
0.835
yes 4
0.835 0.508
```

1 0.54768
1.197

Set cells.
Wall zone 1: tank walls—w1
2: impeller wall—w0
3: Inlet cells—i0

sc 1 53 1 1 1 17 s
sc 1 53 26 26 1 17 w 1
sc 1 1 1 26 1 17 w 1
sc 53 53 2 26 1 17 w 1
sc 14 53 2 3 1 17 w 0
sc 1 53 1 26 1 1 cyclic
sc 1 53 1 26 17 17 cyclic
sc 17 17 5 11 1.17 i 0
sc 21 21 5 11 1 17 i 0

Define density, viscosity, and boundary conditions.
Before the properties are defined, reset the length unit to meters by first setting units to the British system, then back to SI.

ex
su
yes
x
su
no
x
quit
pc
de, n, 1000
vi, 0.001
quit
quit
n
ex
sp
x
yes
yes
0.001
n
c
done

pa
...key in the location of the *i0* cell and then the corresponding velocities, k, and ε.
quit

Set sweep, underrelaxation and variables.

ex sweep
25
5
5
10
5
5
1
3
yes
done
u1
0.1
0.1
0.1
1.0
0.1
0.1
0.1
done
sv
yes
yes
yes
yes
yes
yes
done
quit

Solution step 1: Use the k-ε model and get iteration started.

sc ufbt.cas
ex install
optimizer-solver (no for all)
done
basic (no for vector hardware)
done
quit

quit
c1 500
sd ufbt.dat

Solution step 2: Turn on ASM in the expert menu. Solve for the ASM model.

ex sp
x
x
x
x
x
x
x
yes
x
x
x
c
done
quit
sc ufbta.cas
ex install
optimizer-solver (no for all)
done
basic (no for vector hardware)
done
quit
quit
c1 500
sd ufbta.dat

B.2 Rotating Reference Frame

Customize the length unit . Define domain size, number of cells, and activate turbulent flow.

s1 no
ex su
no
yes 3
centimeters
0.01
no
quit

dd num
53
26
17
done
ds yes
33.6
0
14.5
1.047197
done
dv
yes
c
done
quit

Generating a non-uniform grid

gg
yes 5
0.87 4.2232 8
1 10 19
1.15 17.4832 11
1
yes 5
1 1.2 3
1.18 4.0616 5
1 11.8166 10
0.835
yes 4
0.835 0.508
1 0.54768
1.197

Set cells.
Wall zone 1: tank walls—w1
2: turbine assembly—w0
3: Inlet cells—i0

sc 1 53 1 1 1 17 s
sc 1 53 26 26 1 17 w 1
sc 1 1 1 26 1 17 w 1
sc 53 53 2 26 1 17 w 1
sc 14 53 2 3 1 17 w 0

sc 14 21 4 4 1.17 w 0
sc 14 17 5 10 9 9 w 0
sc 1 53 1 26 1 1 cyclic
sc 1 53 1 26 17 17 cyclic
sc 2 52 25 25 1 17 i 0

Enable rotating reference frame, define rotating speed

ex op
no
yes
x
x
x
x
x
yes
done
body-force
x
x
x
10.472 (for 100 rpm)
done
quit

Before near wall velocities are defined, reset the length unit to meters by first setting units to the British system, then back to SI.

ex
su
yes
x
su
no
x
quit
pc
de, n, 1000
vi, 0.001
quit
quit
pa
2
52

25
25
1
17
w
-1.51844
quit

Set sweep, underrelaxation and variables.

ex sweep
25
5
5
10
5
5
1
3
yes
done
u1
0.1
0.1
0.1
1.0
0.1
0.1
0.1
done
sv
yes
yes
yes
yes
yes
yes
done
quit

Solution step 1: Use the k-ε model and get iteration started.

sc ufbtr.cas
ex install
optimizer-solver (no for all)

done
basic (no for vector hardware)
done
quit
quit
c1 500
sd ufbtr.dat

Solution step 2: Turn on ASM in the expert menu. Solve for the ASM model.

ex sp
x
x
x
x
x
x
x
yes
x
x
x
c
done
quit
sc ufbtra.cas
ex install
optimizer-solver (no for all)
done
basic (no for vector hardware)
done
quit
quit
c1 500
sd ufbtra.dat

APPENDIX C

SIMULATION PROGRAM SETUP FOR BAFFLED CONFIGURATION

This appendix contains the procedures for setting up the computer program of baffled configuration.

C.1 Single Impeller

Customize the length unit. Define domain size, number of cells, and activate turbulent flow.

```
sl no
ex su
no
yes 3
centimeters
0.01
no
quit
dd num
56
21
21
done
ds yes
36.0
0
14.5
1.570796
done
dv
yes
c
done
quit
```

Generating a non-uniform grid

```
gg
yes 4
0.87 8.639 12
1 25.759 32
1.15
yes 4
1 4.86 9
1.19 8.80 5
1
yes 4
0.8696 0.759218 9
1 0.8115781 1
1.15
```

Set cells.
Wall zone 1: tank walls—w1
2: turbine assembly—w0
3: top wall—w2
4: Inlet cells—i0

```
sc 1 18   1 1   1 21   s
sc 1 56   21 21   1 21   w 1
sc 1 1   1 21   1 21   w 1
sc 56 56   3 20   1 21   w 2
sc 19 56   1 2   1 21   w 0
sc 3 56   19 20   11 11   w 0
sc 18 18   4 11   1 21   i 0
sc 22 22   4 11   1 21   i 0
```

Set links for slip wall—w2.
Define system density, viscosity, and boundary coditions.
Before properties are defined, reset the length unit to meters
by first setting units to the British system, then back to SI.

```
ex
su
yes
x
su
no
x
quit
ex op
yes
no
yes
c
done
quit
bc w2
set-links
yes
yes
yes
quit
pc
de, n, 1000
vi, 0.001
```

quit
quit
n
ex
sp
x
yes
yes
0.001
n
c
done
pa
...key in the location of each *i0* cell and then the corresponding velocities, k, and ε.
quit

Set sweep, underrelaxation, and variables.

ex sw
20
5
5
10
5
5
1
3
yes
done
u1
0.1
0.1
0.1
1.0
0.1
0.1
0.1
done
sv
yes
yes
yes
yes
yes
yes

done
quit

Solution step 1: Use the k-ε model and get iteration started.

sc bfbt.cas
sd bfbt.dat
ex install
optimizer-solver (no for all)
done
basic (no for vector hardware)
done
quit
quit
c1 500
sd bfbt1.dat

Solution step 2: Turn on ASM in the expert menu. Solve for the ASM model.

ex sp
x
x
x
x
x
x
x
yes
x
x
x
c
done
quit
sc bfbta.cas
ex install
optimizer-solver (no for all)
done
basic (no for vector hardware)
done
quit
quit
c1 500
sd bfbta.dat

C.2 Double Impellers

Customize the length unit. Define domain size, number of cells, and activate turbulent flow.

```
s1 no
ex su
no
yes 3
centimeters
0.01
no
quit
dd num
56
21
21
done
ds yes
36.0
0
14.5
1.570796
done
dv
yes
c
done
quit
```

Generating a non-uniform grid

```
gg
yes 4
0.87 8.639 12
1 25.759 32
1.15
yes 4
1 4.86 9
1.19 8.80 5
1
yes 4
0.8696 0.759218 9
1 0.8115781 1
1.15
```

Set cells.
Wall zone 1: tank walls—w1
2: turbine assembly—w0
3: top wall—w2
4: Inlet cells—i0

```
sc 1 18   1 1   1 21   s
sc 1 56   21 21   1 21   w 1
sc 1 1   1 21   1 21   w 1
sc 56 56   3 20   1 21   w 2
sc 19 56   1 2   1 21   w 0
sc 3 56   19 20   11 11   w 0
sc 18 18   4 11   1 21   i 0
sc 22 22   4 11   1 21   i 0
sc 41 41   4 11   1 21   i 0
sc 45 45   4 11   1 21   i 0
```

Set links for slip wall—w2.
Define system density, viscosity, and boundary coditions.
Before properties are defined, reset the length unit to meters
by first setting units to the British system, then back to SI.

```
ex
su
yes
x
su
no
x
quit
ex op
yes
no
yes
c
done
quit
bc w2
set-links
yes
yes
yes
quit
pc
```

de, n, 1000
vi, 0.001
quit
quit
n
ex
sp
x
yes
yes
0.001
n
c
done
pa
...key in the location of each *i0* cell and then the corresponding velocities, k, and ε.
quit

Set sweep, underrelaxation, and variables.

ex sw
20
5
5
10
5
5
1
3
yes
done
u1
0.1
0.1
0.1
1.0
0.1
0.1
0.1
done
sv
yes
yes
yes
yes

yes
yes
done
quit

Solution step 1: Use the k-ε model and get iteration started.

sc b2fbt.cas
sd b2fbt.dat
ex install
optimizer-solver (no for all)
done
basic (no for vector hardware)
done
quit quit
c1 500
sd b2fbt1.dat

Solution step 2: Turn on ASM in the expert menu. Solve for the ASM model.

ex sp
x
x
x
x
x
x
x
yes
x
x
x
c
done
quit
sc b2fbta.cas
ex install
optimizer-solver (no for all)
done
basic (no for vector hardware)
done
quit quit
c1 500
sd b2fbta.dat

APPENDIX D

ALIGNMENT AND OPERATION PROCEDURES FOR LDV

This appendix contains the procedures for aligning the laser beams and routine operation of the LDV system.

D.1 Alignment Procedures for LDV

1. Install Model 9102-12 on to the base (Model 9127) of the LDV apparatus, and align the blue and green lights by letting lights pass through the 50 mm holes on the alignment block (using the fine adjust screws on Model 9107) which is sit at a distance about 3 feet away from Model 9107.
2. Install Model 9115-1 and Model 9174 sequentially on to the base and again let the lights pass through the holes on the alignment block by adjusting the screws on Model 9107.
3. Install Model 9102-11 and Model 9115-1 sequentially and repeat the aligning procedures as stated in step 2.
4. Install Model 9182-12 (for green light) and align the light with the alignment block. Tune the compensating wedge ring and tilt adjust on Model 9182-12 which would make the green light shown as a series of vertical spot lights on the alignment block. Then tune the tilt adjust to make the upper most light spot as bright as possible, and make sure that this spot light is disappeared with the frequency shifter off. Now the direction of fringe movement is directed upwards, that is the flow in the upward direction is defined as having a positive sign for green light.
5. Place Model 9182-11 (for blue light) and align the light with the alignment block. Tune the compensating wedge ring and tilt adjust on Model 9182-11 which would make the blue light shown as a series of horizontal spot lights on the alignment block. Then tune the tilt adjust to make the third light spot from left to be the brightest, and make sure that this spot light is disappeared with the frequency shifter off. Now the direction of fringe movement is directed to the right, that is the flow in the rightward direction is defined as having a positive sign for blue light.
6. Place Model 9140 and then Model 9176 on to the base, and also align with the alignment block.
7. Place Model 9145 and align with the alignment block.

8. Install Model 9143 and then Model 9181-4 on to the base. Adjust Model 9181-4 making the emitted light to be the brightest and therefore block off the stray light.
9. Place Model 9176 and then Model 9175, and also align with the alignment block.
10. Place Model 9113-13 and 9189 onto the base.
11. To focus the light converging, Model 10092 (Moving Objective) is employed in combination with the fine adjustment of Model 9175 and 9107.
12. Adjust Model 9140 and 9143 (receiving assembly) and let the Doppler signal to be detected by the oscilloscope.
13. In the mean time, if the aligning procedures are correct, blocking any of the emitted light from the optics would result in no Doppler signal being detected by the oscilloscope.

D.2 Operation Procedures for LDV

1. Slowly open the water supply valve, and allow water to flow through the laser to displace all air in the cooling system.
2. Plug in the electrical power cord.
3. Turn the LINE circuit breaker on. The three LINE indicators and the three fuse indicators will light.
4. The completion of the interlock chain can be inspected by observing the indicators of COVERS, WATER TEMP, WATER FLOW, and REG TEMP. If an indicator is lighten, the interlock chain is complete through that interlock.
5. Slide the BEAM ATTENUATOR to the "CLOSED" position.
6. Set the CONTROL SELECTOR to the "CURRENT" position. Turn the CURRENT CONTROL knob fully clockwise. Turn the METER selector switch to the "CURRENT 50A" position.
7. Press the POWER ON pushbottom.

8. After a 20-30 seconds delay, the ready indicator will light. Then press the LASER START pushbottom to ionize the plasma tube.
9. Once the laser has been started, the LASER meter will indicate a plasma-tube current of 27-33 amperes.
10. Slide the BEAM ATTENUATOR to the "OPEN" position.
11. Slight adjustments to the VERTICAL and HORIZONTAL tuning knobs may now be made to peak the power output.
12. The laser operating level may be set by adjusting the CURRENT CONTROL knob or by the LIGHT CONTROL knob (if operated by light control).
13. To stop the LDV lasing simply sliding the BEAM ATTENUATOR to the "CLOSED" position, and decrease the current level before pressing POWER OFF.
14. Turn off LINE circuit breaker and unplug the power cord, and then close the water supply valve.

REFERENCES

Armenante P. M. and C. C. Chou, 1994. "Experimental LDV Measurement and Numerical CFD Determination of the Fluid Velocity Distribution in an Unbaffled Mixing Vessel," *AIChE Symp. Ser.*, **90**(299): 33-40.

Armenante P. M., C. C. Chou, and R. R. Hemrajani, 1994. "Comparison of Experimental and Numerical Fluid Velocity Distribution Profiles in an Unbaffled Mixing Vessel Provided with a Pitched-Blade Turbine," *Proc. 8th Europ. Conf. Mixing*, No. 136, 349-356.

Armenante, P. M., Y.-T. Huang, and T. Li, 1992. "Determination of the Minimum Agitation Speed to Attain the Just Dispersed State in Solid-Liquid and Liquid-Liquid Reactors Provided with Multiple Impellers," *Chem. Eng. Sci.*, **47**: 2865-2870.

Armenante, P. M. and T. Li, 1993. "Minimum Agitation Speed for Off-Bottom Suspension of Solids in Agitated Vessels Provided with Multiple Flat-Blade Impellers," *AIChE Symp. Ser.*, No. 293, **89**: 105-111.

Bakker A., 1992. "Hydrodynamics of Stirred Gas-Liquid Dispersions," *Ph.D. Dissertation*, Delft University of Technology, The Netherlands.

Bates, R. L., P. L. Fondy, and R. R. Corpstein, 1963. "An Examination of Some Geometric Parameters of Impeller Power," *Ind. Eng. Chem. Proc. Des. Develop.*, **2**: 310-314.

Bates, R. L., P. L. Fondy, and J. C. Fenic, 1986. "Impeller Characteristics and Power," *In* Uhl, V. W. and J. B. Gray (eds.) *Mixing: Theory and Practice*, Vol. III, Academic Press, New York.

Bird, R. B., W. E. Stewart, and E. N. Lightfoot, 1960. *Transport Phenomena*, John Wiley & Sons, New York.

Boussinesq, T. V. 1877. *Mem. Pres. Acad. Sci.*, 3rd ed., Paris.

Bouwmans, I. 1992. "The Blending of Liquids in Stirred Vessels," *Ph.D. Dissertation*, Delft University of Technology, The Netherlands.

Chen, K. Y., J. C. Hajduk, and J. W. Johnson, 1988. "Laser-Doppler Anemometry in a Baffled Mixing Tank," Chem. Eng. Comm. Vol. 72, pp. 141-157.

Chou, P. Y., 1945. "On Velocity Correlations and the Solution of the Equations of Turbulent Fluctuation," Quart. J. Appl. Math., **3**(1): 38-54.

Costes, J., C. Alran, J. P. Couderc, 1991. "Characteristics of the Discharge Flow from a Rushton Turbine. Measurements by Thermal and Laser-Doppler Anemometry," *Int. Chem. Eng.*, **31**: 55-65.

Costes, J. and J. P. Couderc, 1988a. "Study by Laser Doppler Anemometry of the Turbulent Flow Induced by a Rushton Turbine in a Stirred Tank: Influence of the Size of the Units—I. Mean Flow and Turbulence," *Chem. Eng. Sci.*, **43**(10): 2751-2764.

Costes, J. and J. P. Couderc, 1988b. "Study by Laser Doppler Anemometry of the Turbulent Flow Induced by a Rushton Turbine in a Stirred Tank: Influence of the Size of the Units—II. Spectral Analysis and Scales of Tuebulence," *Chem. Eng. Sci.*, **43**(10): 2765-2772.

Creare.x, Inc., 1991. *FLUENT — Computational Fluid Dynamics Software*, Hanover, New Hampshire.

de Groot P. J., 1991. "LDA Used to Check Nagata's Model for Vortex Geometry in Stirred Vessels," *4th Laser Anemom. Int. Conf. (ASME)*, Vol. 1, pp. 247-252.

Deissler, R. G. 1955. *NACA Report* 1210.

Dyster, K., Z. Jaworski, E. Koutsakos, and A. W. Nienow, 1993. "An LDA Study of the Radial Discharge Velocities Generated by a Rushton Turbine: Newtonian Fluids, $Re \geq 5$," *Trans. Inst. Chem. Eng. (Chem. Eng. Res. Des.)*, **71**: 11-23.

Fort, I., 1986. "Flow and Turbulence in Vessels with Axial Impellers", *In* Uhl, V. W. and J. B. Gray (eds.) *Mixing: Theory and Practice*, Vol. III, Academic Press, New York.

Hirata Y., A. W. Nienow, I. P. Moore, 1991. "LDA Studies of Velocity Distributions and Cavern Sizes in a Yield Stress Fluid Agitated by a Rushton Turbine," *Proc. 7th Europ. Conf. on Mixing, Brugge (Belgium), 18-20 Sept. 1991*, Vol. 1, pp. 167-172.

Jaworski Z., A. W. Nienow, E. Koutsakos, K. Dyster, and W. Bujalski, 1991. "An LDA Study of Turbulent Flow in a Baffled Vessel Agitated by a Pitched Blade Turbine," *Trans IChemE, Part A, Chem. Eng. Res. Des.*, **69**: 313-320.

Kresta, S. M. and P. E. Wood, 1991. "Prediction of the Three-Dimensional Turbulent Flow in Stirred Tanks," *AIChE J.*, **37**(3): 448-460.

Kresta, S. M. and P. E. Wood, 1993a. "The Flow Field Produced by a Pitched Blade Turbine: Characterization of the Turbulence and Estimation of the Dissipation Rate," *Chem. Eng. Sci.*, **48**: 1761-1774.

Kresta, S. M. and P. E. Wood, 1993b. "The Mean Flow Field Produced by a 45° Pitched Blade Turbine: Changes in the Circulation Pattern Due to Off Bottom Clearance," *Can. J. Chem. Eng.*, **71**: 42-53.

Launder, B. E. and D. B. Spalding, 1972. *Mathematical Models of Turbulence*, Academic Press, London.

Mahouast, M., G. Cognet, and R. David, 1989. "Two-Component LDV Measurement in a Stirred Tank," *AIChE J.*, **35**: 1770-1778.

Nagata S., 1975, *Mixing*, John Wiley & Sons, New York.

Oldshue, J. Y., 1983. *Fluid Mixing Technology*, McGraw-Hill, New York.

Prandtl, L., 1925. "Bericht ueber Untersuchungen zur ausgebildeten Turbulenz," *App. Math. Mech.* **5**, 136.

Ranadé V. V. and J. B. Joshi, 1989. "Flow Generated by Pitched Blade Turbines I: Measurements Using Laser Doppler Anemometer," *Chem. Eng. Comm.*, **81:** 197-224.

Ranade V. V. and J. B. Joshi, 1990a. "Flow Generated by A Disc Turbine: Part I Experimental," *Trans IChemE*, Vol. 68, Part A, 19-33.

Ranade V. V. and J. B. Joshi, 1990b. "Flow Generated by A Disc Turbine: Part II Mathematical Modelling and Comparison with Experimental Data," *Trans IChemE*, Vol. 68, Part A, 34-50.

Ranade V. V., J. B. Joshi, and A. G. Marathe, 1989. "Flow Generated by Pitched Blade Turbines II: Simulation Using k-ε Model," *Chem. Eng. Comm.*, **81:** 225-248.

Ranade V. V., V. P. Mishra, V. S. Saraph, G. B. Deshpande, and J. B. Joshi, 1992. "Comparison of Axial Flow Impellers Using a Laser Doppler Anemometer," *Ind. Eng. Chem. Res.*, **31**: 2370-2379.

Rewatkar, V. B., K. S. M. S. Raghava Rao, and J. B. Joshi, 1990. "Power Consumption in Mechanically Agitated Contactors Using Pitched Bladed Turbine Impellers, *Chem. Eng. Comm.*, **88**: 69-90.

Rodi W., 1984. *Turbulent Models and Their Application in Hydraulics — A State of Art Review*, Second Edition, International Association for Hydraulic Research, Delft, The Netherlands.

Tatterson G. B., 1991. *Fluid Mixing and Gas Dispersion in Agitated Tanks*, McGraw-Hill Inc., New York, NY.

Taylor G. I., 1932. *Proc. Roy. Soc.*, **A135**, 685-701 (London).

von Karman, T., 1930. *Nachr. Ges. Wiss. Gottingen, Math-physik. kl.*; also *NACA, TM* 611.

Weetman R. J., 1991. "Development of Transitional Flow Mixing Impeller", *Proc. 7th Europ. Conf. on Mixing, Brugge (Belgium), 18-20 Sept. 1991*, Vol. 1, pp. 25-32 .

Wu, H. and G. K. Patterson, 1989. "Laser-Doppler Measurements of Turbulent-Flow Parameters in a Stirred Mixer," *Chem. Eng. Sci.*, **44**: 2207-2221.